Elucidation of the Dominant Factor in Electrochemical Materials Using Pair Distribution Function Analysis

Masakuni Takahashi

Contents

Chapter 1. General Introduction 6

1.1. Background 6

1.2. Fuel cells 7

1.2.1. Over Views of Fuel Cells 7

1.2.2. Issues with Cathode Catalysts for the Commercialization of PEFCs 8

1.2.3. Factors Controlling Activity during Oxygen Reduction Reaction 10

1.3. Li-Ion Secondary Batteries 14

1.3.1. All-Solid-State Batteries 15

1.3.2. Inorganic Solid Electrolytes 16

1.3.3. Applications of Sulfide Solid Electrolytes 21

1.3.4. Issues of Sulfide Solid Electrolytes for Commercialization 22

1.4. Applications of Disordered Materials for Electrochemical Devices 25

1.4.1. Properties of Disordered Materials 25

1.4.2. Structural Analysis of Disordered Materials 28

1.5. Objectives 30

1.6. Outline of the Present Thesis 31

Chapter 2. Observation of Subsurface Structure of Pt/C Catalyst Using Pair Distribution Function and Simple Modeling Techniques 63

2.1. Introduction 63

2.2. Experimental Section 65

2.2.1. Preparation of Annealed Samples. 65

2.2.2. TEM, XAFS and XRD Measurements. 65

2.2.3. High-Energy X-ray Total Scattering Measurement and Pair Distribution Function (PDF) Analysis. 66

2.2.4. Electrochemical Characterization. 67

2.3. Results and Discussion 68

2.4. Conclusion 72

Chapter 3. Synthesis of Sulfide Solid Electrolytes through the Liquid Phase: Optimization of the Preparation Conditions by Using Pair Distribution Function Analysis 88

3.1. Introduction 88

3.2. Experimental Section 90

3.2.1. Synthesis Methods of Li_3PS_4 90

3.2.2. Raman Spectroscopy, Thermogravimetry, XRD Measurements, and Scanning Electron Microscopy Observation 91

3.2.3. High-Energy XRD Measurement Coupled to PDF Analysis 92

3.2.4. Ionic Conductivity 92

3.3. Results and Discussion 93

3.4. Conclusion 101

Chapter 4. Improvement of lithium ionic conductivity of Li_3PS_4 through suppression of crystallization using low-boiling-point solvent in liquid-phase synthesis 127

4.1. Introduction 127

4.2. Experimental Section 129

4.2.1. Preparation of Li_3PS_4 through liquid-phase synthesis 129

4.2.2. Thermogravimetric analysis (TGA) and XRD measurement 129

4.2.3. High-energy XRD coupled with PDF analysis 130

4.2.4. Ionic conductivity measurement 130

4.3. Results and Discussion 130

4.4. Conclusion 136

Chapter 5. Elucidation of Relationship between Local Structure and Lithium Ion Conductivity of LiI-doped Li_3PS_4 for Li Dendrite Suppression by Using Pair Distribution

Function Analysis 152

5.1. Introduction 152

5.2. Experimental Section 154

5.2.1. Synthesis and annealing of the (100-x) Li_3PS_4 – x LiI solid electrolyte .. 154

5.2.2. Ionic conductivity measurement 154

5.2.3. Critical current density measurement for short-circuiting caused by lithium dendrite formation. 155

5.2.4. Characterization 155

5.3. Results and Discussion 156

5.4. Conclusion 163

Chapter 6. General conclusions 185

Acknowledgements 187

Chapter 1. General Introduction

1.1. Background

In recent years, numerous environmental issues have emerged. In particular, global warming caused by carbon dioxide emission has become a serious concern. To overcome this issue, it is necessary to mitigate carbon dioxide emissions. Large amounts of carbon dioxide are emitted from thermal power plants and vehicles, both of which are a global necessity. Moreover, the global demand for electricity is increasing; hence, it is difficult to significantly decrease carbon dioxide emissions. Furthermore, smart grids have been attracting attention in recent years. Smart grids are not only power grids but also a system that efficiently supplies electricity to residences, industries, and other areas where electricity is consumed, using the latest power and information technologies[1-8]. Moreover, smart grids can not only provide weather-dependent renewable energy but also store the excess energy as chemical energy. Therefore, the optimization of the generation and distribution of electricity, as well as the introduction of renewable energy, can decrease significant CO_2 emissions.

Power sources for vehicles and distributed energy-storage devices are important components of a smart grid. These devices require high power density and/or high energy density. They consist of supercapacitors, lead-acid batteries, fuel cells, and lithium-ion batteries (LIBs). Supercapacitors use an electric double layer to store electricity, and they can be charged and discharged faster than batteries that use chemical reactions[9-10]. Lead-acid batteries can be charged and discharged by passing sulfate ions between the

electrodes and the electrolyte, and they involve the lowest cost per unit of electricity. However, because of their low energy density, they are unsuitable as power sources for vehicles and as distributed energy-storage devices. In contrast, fuel cells generate electricity by the reaction of oxygen with hydrogen or other fuels, and they exhibit high energy density[6-8]. LIBs, which charge and discharge electricity by moving Li ions between the cathode and anode, are rechargeable batteries with high power density[1-5]. Therefore, fuel cells and LIBs are suitable for powering vehicles and as distributed energy-storage devices. However, the performance of these electrochemical devices is not sufficient. Therefore, it is necessary to improve their performance for use in smart grids.

1.2. Fuel cells

1.2.1. Over Views of Fuel Cells

Fuel cells were first developed by Lord Grove in 1839 to generate electric current from hydrogen and oxygen gas[11]. In recent years, they have received attention as an alternative power generation method, owing to their low environmental load and high energy efficiency[6-8]. For this reason, the research and development of fuel cells for practical use has been actively performed. Recently, a residential fuel-cell cogeneration system, Panasonic ENE-FARM, and fuel-cell-energized vehicles have been developed. Figure 1 shows a scheme of a typical proton-conduction fuel cell.

In a fuel cell, hydrogen oxidation and oxygen reduction proceed at the anode and cathode, respectively, with electrons flowing through the external circuit to extract chemical energy as electrical energy. For the case where the electrolyte is the proton conductor and hydrogen is the fuel, the reaction is expressed as follows:

Anode： $H_2 \rightarrow 2H^+ + 2e^-$ eq. 1

Cathode： $2H^+ + 1/2\ O_2 + 2\ e^- \rightarrow H_2O$ eq. 2

Total ： $H_2 + 1/2O_2 \rightarrow H_2O$ eq. 3

A polymer electrolyte fuel cell (PEFC) is a fuel cell that uses a solid polymer membrane as the electrolyte. The conductivity of a proton-conducting polymer, which is mainly used as the electrolyte, is significantly affected by the amount of water in the membrane, and a decrease in the water content leads to a decrease in conductivity[12]. Therefore, it is necessary to operate at a sufficiently low temperature to avoid the volatilization of water. Operating at a low temperature provides several advantages, including short start-up time, inexpensive materials, and a wide range of material choices. Therefore, PEFCs are suitable as power sources for automotive applications and portable devices[7-8]. Currently, owing to these advantages, ENE-FARM has been commercialized as a stationary generator and Toyota's MIRAI and Honda's FCX CLARITY as fuel-cell vehicles in Japan. However, problems related to cathode catalysts remain.

1.2.2. Issues with Cathode Catalysts for the Commercialization of PEFCs

Research and development are underway to further expand the use of fuel cells; however, the high cost of the cells has prevented their widespread applications. One of the challenges is the high cost of the Pt/C catalyst used in both the electrodes. It is necessary to use a Pt/C catalyst because the low operating temperature of the PEFC makes it difficult for the reaction to proceed. However, the cost of the catalyst is high because Pt is a precious metal and expensive. Improving the catalytic lifetime of the Pt/C catalyst

can reduce the cell cost. The degradation mechanism has been investigated to improve the catalyst lifetime. The following is a summary of the degradation mechanism.

It has been reported that the dissolution of Pt proceeds at a pH below 2 and a potential higher than 0.85 V vs. the reversible hydrogen electrode (RHE)[13]. The mechanism of dissolution involves not only the direct dissolution of Pt nanoparticles to produce Pt^{2+} ions without intermediates but also a process whereby platinum oxide is initially formed and then dissolved by protons supplied by the anode to produce Pt^{2+} ions[14-15].

$$Pt \rightarrow Pt^{2+} + 2e^- \qquad E_0 = 1.188\ V \qquad \text{eq. 4}$$

$$Pt + H_2O \rightarrow PtO + 2H^+ + 2e^- \qquad E_0 = 0.980\ V \qquad \text{eq. 5}$$

$$PtO + 2H+ \rightarrow Pt^{2+} + H_2O + 2e^- \qquad \text{eq. 6}$$

The Pt^{2+} ions produced by the dissolution of the Pt nanoparticles diffuse into the electrolyte membrane and is reduced by H_2 diffused from the anode side. It has been reported that the Pt nanoparticles form aggregates called Pt bands. These nanoparticles are aligned in bands in the electrolyte membrane. The Pt bands appear in both the left and right anodes as well as in the cathode catalyst layers[16-17]. Hydrogen peroxide and radical species formed in these Pt bands also react with the electrolyte membrane, leading to membrane degradation[16-17]. It has been reported that, as a result, the performance of the fuel cell reduces. In addition, Pt^{2+} formed by the dissolution of Pt nanoparticles is not only present in the electrolyte membrane but also precipitated onto the Pt nanoparticles. This mechanism of particle enlargement by the dissolution and precipitation of Pt nanoparticles is called Ostwald ripening[18-19]. Ferreira et al. performed cyclic degradation tests and employed transmission electron microscopy to observe the shapes of the Pt nanoparticles before and after the tests[13]. As a result, the enlarged particles caused by

Ostwald ripening can be classified into two types: spherical particles that remain supported on the carbon, and particles that have dropped off the carbon and are not spherical[13]. In addition, it was observed that Ostwald ripening significantly contributes to a decrease in the platinum surface area[13]. The mechanism of Pt nanoparticle enlargement other than Ostwald ripening has also been reported. Yasuda et al. and Han et al. performed cyclic degradation tests and observed the morphology of the catalyst before and after the degradation tests[20]. Yasuda et al. reported that aggregates were visible in the electrolyte membrane near the cathode support[20]. Han et al. reported that the aggregated Pt particles showed a boundary in the lattice images of the distorted Pt nanoparticles observed after the cyclic degradation tests[21]. They concluded that these Pt nanoparticles were produced by the aggregation of two Pt nanoparticles[21]. The sintering mechanism, in which Pt nanoparticles form aggregates with each other so that the particles are enlarged, also reduces the Pt surface area and reduces the fuel cell performance. A scheme of the degradation mechanism is shown in Figure 2.

The current discussion of the degradation mechanism is completely based on the morphology. However, to improve the long-term stability of the polymer electrolyte fuel cells, it is necessary to clarify the degradation mechanism at the atomic level, including the surface structure of the catalyst, which directly affects catalytic activity. In the next section, the relationship at the atomic level between the local structure and the oxygen-reduction activity is discussed.

1.2.3. Factors Controlling Activity during Oxygen Reduction Reaction

When an atom or molecule is adsorbed on a metal surface, hybridization occurs

between the *sp* orbitals of the adsorbed material and the *d*-band of the metal surface. J. K. Nørskov et al. reported that the binding energy changes, depending on the energy levels of the bonding and antibonding hybrid orbitals formed with the *d*-band of the metal surface[22-23]. In the following sections, we will explain the effect of the energy levels of these bonding and antibonding orbitals on the adsorption of oxygen atoms on Ru, Cu, Au, Ni, Pd, and Pt (Figure 3)[23]. When oxygen atoms are adsorbed on Ru, the bonding orbital energy level of the hybrid orbitals is lower than that of the oxygen atoms. As a result, the binding energy of oxygen on the metal surface is higher and the adsorption state of oxygen is stabilized. The energy levels of the hybrid orbitals when oxygen atoms are adsorbed on Cu, Ag, and Au are different from those when oxygen atoms are adsorbed on Ru. The energy levels of the anti-bonding hybrid orbitals are lower than the Fermi level. Therefore, the electrons occupy not only the associative orbitals but also the anti-coupling orbitals. The anti-bonding orbitals are occupied by electrons, which lowers the binding energy and destabilizes the adsorption state. With regard to the hybrid orbitals for the adsorption of oxygen atoms on Pt, the energy levels of the bonding hybrid orbitals are lower than those of the bonding orbitals of oxygen, and the energy levels of the anti-bonding orbitals are higher than those of the Fermi level. These results indicate that the binding energy between Pt and oxygen atoms is high. As mentioned above, the binding energy varies with the energy levels of the hybrid orbitals before and after adsorption.

The binding energy with the oxygen atom increases as the energy of the *d*-band center increases (Figure 4(a))[24]. The width of the *d* band decreases as the energy of its center increases, and the number of electrons remains constant. As a result, the number of anti-bonding orbitals below the Fermi level that are occupied by electrons after the formation of the hybrid orbitals decreases, and the binding energy becomes higher (Figure

4(b))[20]. As described above, the position of the *d*-band center can be used to evaluate the binding energy.

Adzic et al. reported that the *d*-band center exhibits a linear trend with the oxygen binding energy, whereas the area-specific activity of oxygen reduction exhibits a "volcano" type trend with the area-specific activity of the oxygen reduction reaction, as shown in Figure 5(a)[25]. The oxygen reduction reaction proceeds by the dissociation of oxygen molecules and the hydrogenation of oxygen adsorbed on the catalyst surface. In addition, the higher binding energy with oxygen increases the stability of the oxygen molecules at the catalyst surface. As a result, the activation energy of dissociation of the oxygen molecules is reduced, and the reaction proceeds in a simpler manner. However, owing to the stability of the oxygen atoms adsorbed on the catalyst surface, the activation energy for the hydrogenation of oxygen is higher, and hydrogenation is less likely to proceed. Therefore, as shown in Figure 5(b), when the binding energy with oxygen is high, the activation energy for the dissociation of oxygen decreases while the activation energy for the hydrogenation of the adsorbed oxygen increases[25]. The dissociation and hydrogenation of molecular oxygen are indispensable for the oxygen reduction reaction to proceed. When the binding energy with oxygen is high, hydrogenation becomes the rate-limiting factor for the reaction, and when it is low, the dissociation of oxygen becomes the rate-limiting factor[25]. Therefore, the area-specific activity is reported to exhibit a volcano-type trend, with reaching a maximum when activation energy of oxygen dissociation and hydrogenation are optimal[25].

J. K. Nørskov et al. performed the density functional theory (DFT) calculations of the adsorption energies of CO and O on the Ru (0001) surface and the energy of CO dissociation on the metal surface under compressive and tensile stresses[26]. The results

indicate that as the lattice constant increases, the overlap between the *d* electrons of adjacent metal atoms decreases and the *d*-band width decreases[26]. They reported that the *d*-band center increases to maintain the occupancy of the *d*-band electrons and that the binding energy changes[26]. In addition, they also reported that the most active catalysts can be created by adjusting the lattice constant.

Wang et al. synthesized PtMLPd/C for Pd/C with different particle systems and surface roughness by the underpotential deposition of copper, followed by the substitution of Pt atoms for copper atoms on the Pd surface[27]. The interatomic distances were determined by the extended X-ray absorption fine structure (EXAFS) of X-ray absorption fine structure (XAFS) measurements, and the correlation between the interatomic distances and the oxygen reduction activity of the $Pt_{shell}Pd_{core}$ catalyst was investigated. The specific activity was observed to be correlated with the interatomic distance, and the area-specific activity increased with decreasing interatomic distance[27]. These results indicate that the Pt-Pt interatomic distance is a useful indicator of oxygen reduction activity.

X-ray diffraction (XRD) and XAFS measurements have been used for structure evaluation in previous studies. XRD measurements are useful for evaluating the particle size and lattice parameters of Pt catalysts[28-31]. For structural analysis using Bragg reflection, as in XRD measurements, it is assumed that the periodic structure consists of an Avogadro number of atoms approximately. However, in the case of nanoparticles, such a long-period structure cannot be developed, and the structural information obtained may be different from that obtained for the macroscopic structure. XAFS measurements are very useful not only for determining the oxidation state of a Pt catalyst but also for evaluating the coordination number and interatomic distances[32-34]. However, XAFS

measurements can provide only average structural information. Therefore, it is not possible to directly obtain structural information on the catalyst surface in cases where the reaction field and the structure significantly influence the activity.

The correlation between the surface structure and the activity of a catalyst is very important to establish a principle for improving the activity and lifetime of the catalyst. As mentioned above, conventional XRD and XAFS measurements provide only the average structure; hence, it is difficult to investigate the surface structure of the catalysts.

1.3. Li-Ion Secondary Batteries

Lithium-ion batteries (LIBs) play an important role in modern society. This section describes the mechanism and composition of a conventional LIB using an organic solvent as the electrolyte. Figure 6 shows a schematic diagram of a typical commercial LIB. Generally, a Li-containing transition metal oxide $LiMO_2$, graphite, and an organic solvent with Li salt dissolved in it function as the cathode, the anode, and the electrolyte, respectively. The charge–discharge reaction of this battery can be represented by following equation:

$$\text{Cathode}: Li_{1-x}MO_2 + xLi^+ + xe^- \Leftrightarrow LiMO_2 \qquad \text{eq. 7}$$

$$\text{Anode}: Li_xC_6 \Leftrightarrow xLi^+ + xe^- + C_6 \qquad \text{eq. 8}$$

$$\text{Total}: Li_{1-x}MO_2 + Li_xC_6 \Leftrightarrow LiMO_2 + C_6 \qquad \text{eq. 9}$$

Li ions in the crystalline structure of the cathode material are extracted and transported into the electrolyte during charging, and the Li ions in the electrolyte are inserted into the structure of the anode material. At the same time, electrons are transferred from the cathode to the anode through the external circuit. During discharge, the opposite process

occurs. The battery can store and extract power from the Li-ion movement and electrons from the anode to the cathode using the inside of the battery and the external circuit, respectively. Current LIBs that use organic solvents as the electrolyte are unsafe because of the risk of ignition of the organic solvent[35-38]. In addition, the ranges of temperature and potential are low. In recent years, all-solid-state batteries using solid electrolytes have been receiving significant attention. The following section describes these all-solid-state batteries.

1.3.1. All-Solid-State Batteries

In recent years, all-solid-state batteries that use solid electrolytes instead of organic liquid electrolytes have received immense attention [39-47]. In the case of organic electrolytes, there are restrictions related to the shape of the battery to prevent leakage as well as to limit the operating temperature[43, 45] and voltage[42] because of the risk of ignition and explosion. In contrast, all-solid-state batteries provides higher safety than the conventional LIBs because the solid electrolyte does not involve the risks of burning, leaking, or corroding. As a result, the thickness of the all-solid-state batteries can be decreased. These batteries can be layered to create multiple structures, and they can also be bent. Furthermore, it is possible to increase the energy density using multiple layers[46-47]. In addition, they can be used in a variety of environments because they retain their performance over a wide range of temperatures, owing to the high thermal stability of the solid electrolyte. The solid electrolyte is the important component in the all-solid-state batteries because its characteristics limit the voltage range, temperature, and anode material. The properties of the solid electrolytes are required to include high ionic conductivity and desirable thermal and electrochemical stabilities for high-voltage

cathodes, as well as chemical stability in the presence of Li metal anodes. Several types of solid electrolytes have been developed. In the following section, the structure and ionic conduction mechanism, as well as the advantages and disadvantages of each type of solid electrolyte will be described.

1.3.2. Inorganic Solid Electrolytes

1.3.2.1. Oxide Solid Electrolytes

Oxide solid electrolytes can be divided into the LISICON (Li super ionic conductor)-like, NASICON (Na super ionic conductor)-like, garnet, and perovskite types. The structure, ionic conduction mechanism, advantages, and disadvantages of each type are described below.

The LISICON-like solid electrolyte is a structure with an orthorhombic unit cell and space group *Pnma*[48-50]. In this crystal structure, all the cations are in tetrahedral coordination (Figure 7). The structure can be described as hexagonal close-packed with oxygen atoms aligned along the *c*-axis. The Li and other cations are arranged alternately in a tetrahedral arrangement, and the Li ions in the LiO_4 tetrahedron diffuse through the interstitial sites in the tetrahedron of another cation[48]. The first known LISICON-like solid electrolyte is $Li_{14}Zn(GeO_4)_4$ reported by Hong et al., with an ionic conductivity of 0.13 S cm^{-1} at 573 K[49]. However, there are disadvantages involved in the LISICON-like solid electrolyte, such as low ionic conductivity at room temperature as well as instability to Li metal and air.

Generally, the NASICON-type solid electrolyte consists of a rhombohedral unit cell. This solid electrolyte is a phosphate, described as $L_{1+6x}M^{4+}{}_{2-x}M'^{3+}{}_{x}(PO_4)_3$, where L is Li or Na, M is Ti, Ge, Sn, Hf, or Zr, and M′ is Cr, Al, Ga, Sc, Y, In, or La[51-56]. The

framework is constructed from PO_4 tetrahedra and MO_6 octahedra sharing a corner. The Li ions occupy two types of sites: one is the center of the six-coordinated structure with oxygen between the MO_6 octahedra and the other is the central site of the eight-coordinated structure with oxygen between the columns developed by the MO_6 octahedron (this structure is shown in Figure 8)[55,57]. The Li ions diffuse through these two sites[55]. $Li_{1+x}Al_xGe_{2-x}(PO_4)_3$ (LAGP) and $Li_{1+x}Al_xTi_{2-x}(PO_4)_3$ (LATP) exhibited the highest ionic conductivities (10^{-3} and 10^{-2} S cm^{-1}) at room temperature [57-60]. However, Ti^{4+} is easily reduced at Li metal anodes, which restricts the applications of LATP. Therefore, LAGP, which does not contain Ti, is more suitable for a wide range of applications.

Garnet-type solid electrolytes possess a cubic unit cell represented using the general formula $A_3B_2(XO_4)_3$. Here, the A site, B site, and X site possess an eight-coordinated structure, a six-coordinated structure, and a four-coordinated structure, respectively[61-64]. Li is present in the four-coordinate sites in a typical Li-conducting garnet-type solid electrolyte (Figure 9). However, the mobility of Li in the four-coordinate site is low. $Li_3Ln_3Te_2O_{12}$, in which the Li ion is only present in the four-coordinate sites, is known to possess low ionic conductivity [62]. To further improve the ionic conductivity, studies have been conducted to add more Li ions into the structure by adjusting the valence of the A and B site cations. The introduction of pentavalent ions causes the Li ions to occupy some of the distorted octahedral sites in addition to the tetrahedral sites. The Li ions in the octahedral sites exhibit high mobility, an effect due to static repulsion caused by the short Li-Li distance. Consequently, garnet-type solid electrolytes such as $Li_7La_3Zr_2O_{12}$ (LLZO) with Li ions in the octahedral sites exhibit high ionic conductivity (of the order 10^{-3} S cm^{-1}) at room temperature [61]. However, these garnet-type solid

electrolytes are reported to be unstable toward the cathode and exhibit high contact resistance with Li metal [63].

Perovskite-type solid electrolytes are represented by the general formula ABO_3. The A atoms, B atom, and oxygen atoms are present at the corners, the body center, and the face centers of the cubic unit cell (Figure 10)[65-67]. In this perovskite-type solid electrolyte, Li ions diffuse over the ab-plane through the square plane bottleneck consisting of oxygen. The ionic conductivity of perovskite solid electrolytes has been reported to be significantly affected by the concentrations of Li ions and vacancies as well as the size of the bottleneck[65]. It has been reported that the bottleneck can be controlled by replacing La and Ti ions with other elements such as Al and Mg to produce certain materials that exhibit high ionic conductivity, up to 10^{-3} S cm^{-1}, at room temperature,[68]. However, although this perovskite solid electrolyte is stable at high potentials, it is known to be reduced at approximately 1.5 V vs. Li/Li^+; hence, it is unsuitable for use with Li and graphite anodes.

1.3.2.2. Sulfide-Based Solid Electrolytes

Sulfide-based solid electrolytes possess higher Li ion conductivity than oxide-based solid electrolytes, owing to a larger ionic radius of S^{2-}, higher polarization, and lower electronegativity compared to O^{2-}; hence, the binding of Li ions to the skeletal structure becomes weak, resulting in wider ion-transport passages and easier ion transport. In addition, sulfide solid electrolytes have a desirable contact between the electrode and the electrolyte by one-axis pressurization because the sulfide materials exhibit a relatively low elastic modulus[69-70]. Hence, sulfur solid electrolytes possess potential practical applications in all-solid-state batteries. They are available in different types of crystalline

and glass–ceramic materials. The structure, advantages, and disadvantages of each type of sulfide solid electrolyte are described below.

The crystalline sulfur solid electrolytes can be divided into LISICON-like and argyrodite types. The structures and properties of these crystalline materials are described below.

Since Taches et al. discovered the sulfide solid electrolyte Li_3PS_4 in 1984, LISICON-like materials have been studied in various sulfide solid electrolytes [71]. Among these LISICON-like sulfur solid electrolytes, $Li_{10}GeP_2S_{12}$ (LGPS) and $Li_{11}Si_2PS_{12}$ exhibit high Li ion conductivity of approximately 10^{-2} S cm^{-1} at room temperature[43, 72]. The crystal structure of LGPS possesses a tetragonal unit cell formed from a PS_4 tetrahedron, a $(M/P)S_4$ tetrahedron, and a LiS_6 octahedron. In this structure, the 2*b* sites are completely occupied by phosphorus, the 4*d* sites are partially shared by germanium and phosphorus in a ratio of 1:1, and Li is distributed over four crystal structure sites (4*c*, 4*d*, 8*f*, and 16*h*). The 4*d* site Li octahedra and the $(P/Ge)S_4$ tetrahedra form a one-dimensional chain along the c-axis with shared edges (Figure 11)[43]. The 4*d* site Li octahedron also develops an a- and b-axis connected structure with the 2*b* site PS_4 tetrahedron in the form of shared corners. In LGPS, the Li ions conduct through a one-dimensional chain along the c-axis formed by sharing the edges of the 4*d* site Li octahedron and the $(P/Ge)S_4$ tetrahedron[43]. The transfer energy of Li ion transport through this one-dimensional channel is reported to be very low; therefore, the Li ion conductivity is high.

Deiseroth et al. reported argyrodite-type sulfur solid electrolytes, which are newly discovered crystalline sulfur solid electrolytes with a cubic unit cell[73]. In this structure, the phosphorus atoms form a network of isolated PS_4 tetrahedra, with halogen atoms at the 4*a* sites, sulfur atoms at the 4*c* sites, and Li ions randomly located at the 24*g*

and 48*h* sites[74]. In this structure, hexagonal cages formed by the sulfur atoms at sites 4*c* and the Li ions around them are connected by interstitial sites around the sulfur and halogen ions, and Li is conducted through this chain of hexagonal cages(Figure 12)[74]. It has been reported that LGPS and the argyrodite sulfur solid electrolytes exhibit high ionic conductivity, but their low stability toward Li metal anodes at low voltages restricts their applications in all-solid-state batteries[75]. These crystalline materials are synthesized by solid-phase synthesis that is difficult to operate on a large scale, followed by the prolonged heat treatment. Hence, it is difficult to synthesize them industrially, and these materials are unsuitable for practical use.

Amorphous materials are materials that do not have a medium- to long-range ordered structure. Sulfide amorphous solid electrolytes have been the subject of various studies. An example is Li_2S-P_2S_5 glass materials that are reported to develop a short-range ordered structure composed of the P_xS_y species such as PS_3^{4-}, $P_2S_7^{4-}$, $P_2S_6^{4-}$ and $P_2S_6^{2-}$ [76]. It is reported that in the Li_2S-P_2S_5 glass materials, the PS_3^{4-} tetrahedron transitions from the $P_2S_7^{4-}$ icosahedron and the Li ionic conductivity are increased by increasing the ratio of Li_2S to P_2S_5 (Figure 13)[77]. Ohara et al. reported that increasing the molar ratio of Li_2S to P_2S_5 from 67% to 75% changes the dominant Li species from PS_4 and P_2S_7 to mostly PS_4 and certain P_2S_6, and the simulation of this material structure indicates that polyhedral edge-sharing in the P_2S_7 unit causes the ionic conductivity to decrease as a result of increased interaction with Li ions[78]. Among these sulfide amorphous materials, Li_2S-P_2S_5 glasses doped with Li halide exhibit higher ionic conductivity than the original Li_2S-P_2S_5 glass materials[79-80]. In addition, it has been reported that the incorporation of LiI into the solid electrolyte interphase layers suppresses the dendrite growth, owing to the introduction of highly ionic but electronically insulating LiI (Figure 14).[81-82].

It is clear that amorphous materials have advantages such as high ionic conductivity due to their large free volume and structural diversity, which allows the addition of different materials, thereby changing their properties, including electrochemical stability. However, problems related to synthesis and dendrite formation for practical use remain. These problems are discussed in the following section.

1.3.3. Applications of Sulfide Solid Electrolytes

As mentioned above, the LISICON-like and argyrodite-type sulfide solid electrolytes, which are crystalline materials, exhibit high Li ionic conductivity. A new Li superionic conductor, $Li_{9.54}Si_{1.74}P_{1.44}S_{11.7}Cl_{0.3}$, reported by Kato et al. in 2016 exhibited the highest conductivity of all the reported Li superionic conductors[83]. All-solid-state battery cells using this material as the electrolyte, $LiCoO_2$ coated with $LiNbO_3$ as the cathode, and $Li_4Ti_5O_{12}$ as the anode, exhibit excellent rate performance, with the discharge current densities of 150 C at 25 °C and 1500 C at 100 °C in the voltage range of 1.0–2.6 V[83]. In addition, it was reported that this all-solid-state cell exhibited approximately 75% capacity retention and 100% Coulombic efficiency after more than 500 cycles[83].

In addition, crystalline materials and amorphous sulfide solid electrolyte materials are investigated for practical applications. Ohtomo et al. have prepared cells using amorphous and glass-ceramic sulfide solid electrolytes and compared their battery performances. They reported that an all-solid-state battery with a glass solid electrolyte exhibited higher rate performance than that with a glass-ceramic solid electrolyte[84]. In addition, changing the composition of the Li_2S-P_2S_5 amorphous solid electrolyte from 70 Li_2S : 30 P_2S_5 to 75 Li_2S : 25 P_2S_5 was reported to decrease the rate performance but

increase the electrochemical stability (Figure 15) [84]. The addition of 5 mol% Li_3PO_4 to the 70 Li_2S : 30 P_2S_5 solid electrolyte was also reported to increase the stability of the electrolyte at high temperatures (100 °C) [85].

1.3.4. Issues of Sulfide Solid Electrolytes for Commercialization

1.3.4.1. Synthesis

Sulfide solid electrolytes are generally synthesized by a solid-phase method, there are two method. one is heated in a vacuum-sealed quartz ampoule, other is mechanical milling method. In mechanical milling, the solid electrolyte is synthesized by the planetary ball milling of the raw materials. This method has been widely used to synthesize Li_2S-P_2S_5 sulfide glasses, glass ceramics,[86-87] and Li argyrodite Li_6PS_5X (X = Cl, Br, or I) [88-89]. Using this method, it is possible to form a metastable amorphous phase immediately after ball milling.

Another method is annealing a quartz ampoule containing the premixed raw powder sealed in vacuum; Li superionic conductors such as $Li_{10}GeP_2S_{12}$ have been prepared using this method[43, 71, 90]. The advantage of this method is that it is possible to anneal at high temperatures for a long time while preventing the release of sulfur species. For this reason, numerous crystalline sulfide solid electrolytes have been prepared using this method. However, using this method, it is difficult to produce large amounts and it involves long reaction durations, which are the disadvantages in terms of economic requirements[43, 71, 86-90]. Therefore, it is desirable to develop novel production methods for large-scale synthesis.

In recent years, liquid-phase synthesis has been receiving attention as an alternative to solid-phase synthesis[91-99]. Liquid-phase synthesis is a method for

synthesizing sulfide solid electrolytes by stirring the raw materials in an organic solvent and then annealing. This method is suitable for industrialization because a large amount of solid electrolyte can be produced in a short reaction time. Another advantage of this method is that a thin coating of the solid electrolyte can be applied to the active material. Composite cathodes are commonly prepared by grinding and mixing the solid electrolyte and active material, and the content of solid electrolyte content needs to be 30–60 wt% to maintain the Li ion conduction pathway to the electrodes[100]. However, decreasing the amount of active material in the electrodes tends to decrease the energy density. The results of using a model active material coated with a thin film of the solid electrolyte by pulsed laser deposition have confirmed that it is possible to increase the energy density by decreasing the amount of the solid electrolyte required to maintain the Li ion conduction pathway[45, 101-102]. In liquid-phase synthesis, the solid electrolyte can be uniformly coated onto the active material by simply mixing the active materials with the solid electrolyte dissolved or dispersed in a solvent and then annealing it. This process does not require the use of special equipment and is also easy to scale up. Liquid-phase synthesis provides significant industrial advantages. Therefore, numerous studies on its practical applications have been carried out. In particular, the liquid-phase synthesis of Li_3PS_4, which exhibits high electrochemical stability among the sulfur solid electrolytes, has been extensively studied.

However, the ionic conductivities exhibited by the sulfide solid electrolytes during liquid-phase synthesis were lower than those exhibited during solid-phase synthesis[91-99]. The relatively low ionic conductivity of Li_3PS_4 prepared in the liquid phase is due to two factors: the presence of residual unreacted Li_2S and its relatively high crystallinity[96, 103-104]. Shin et al. reported that the low ionic conductivity is due to

unreacted starting material, Li_2S[40]. However, the presence of unreacted Li_2S has not been confirmed by XRD or Raman spectroscopy in other studies[91-95, 97-99]. Crystallinity is another factor affecting Li ionic conductivity; in the case of Li_3PS_4, it has been reported that the ionic conductivity is high when the main structure is amorphous, and it decreases as crystallization progresses because of the absence of fast ion pathways in the crystal structure[49-50]. It has been reported that in liquid-phase synthesis, Li_3PS_4 becomes highly crystallized during annealing where the solvent is removed, resulting in a decrease in ionic conductivity[91-95, 97-99, 105]. However, the contribution of these factors to ionic conductivity has not been completely elucidated, owing to the difficulty of quantitatively evaluating the amount of raw materials such as Li_2S and the degree of crystallinity using conventional analytical methods such as Raman spectroscopy and XRD measurements.

1.3.4.2. Material Properties

All-solid-state batteries that replace conventional liquid electrolytes with solid sulfide electrolytes can provide improved safety and power density than conventional batteries. In addition, all-solid-state batteries using sulfide electrolytes can operate over a wide temperature range because of their high thermal stability. In addition, as mentioned, LGPS and argyrodite-type sulfide solid electrolytes exhibit excellent Li ion conductivity[43, 71, 90]. Moreover, because of their low elastic moduli, the grain boundary resistance of sulfide solid electrolytes can be decreased by simple pressing. However, the current all-solid-state batteries based on sulfur solid electrolytes present challenges for practical applications. They require properties such as high stability and high conductivity at the electrode interface, as well as high ionic conductivity and the ability to synthesize the solid electrolytes under conditions feasible for commercialization. However, in the case

of crystalline materials, structural and compositional limitations hinders further enhancement of properties.

Moreover, in the case of amorphous materials, the diversity of structures allows various compositions and the addition of different materials. Hence, it is possible to change properties such as the ionic conductivity, electrochemical stability, and the battery performance[76-77, 79-80]. Amorphous sulfide solid electrolyte materials as well as crystalline materials are also investigated for practical applications. If the most suitable amorphous material is developed and its electrochemical stability is improved, it can be used as a high voltage cathode and Li metal anode, which will further improve the capacities of all-solid-state batteries.

However, the structural evaluation of these materials is very difficult because they do not exhibit long-range periodic structure. Because only fragment structural information can be obtained using the conventional methods, the mechanism of structural influence on their properties and the factors governing them remain unclear. To improve the properties of the amorphous materials, it is necessary to elucidate these mechanisms and establish principles for the design of amorphous solid electrolytes with superior properties.

1.4. Applications of Disordered Materials for Electrochemical Devices

1.4.1. Properties of Disordered Materials

Disordered materials, such as amorphous materials and nanoparticle catalysts, have been receiving immense attention in recent years because they have been reported

to exhibit higher activity compared to crystalline materials[106-114]. It is important to understand the influence of structure of disordered materials to the property. In the following section, we will use nanoparticle catalysts and amorphous materials as examples to explain the influence of the difference of structure on the reaction.

Various chemical reactions occur at the catalyst interface. The surface structure plays an important role in several physical and chemical processes[114-115]. In bulk solids, because the ratio of surface atoms to all the atoms is low, the influence of the surface free energy is small; hence, the surface structure forms a structure close to the stable phase. However, as the proportion of surface atoms increases by decreasing the material grain size, the surface free energy cannot be neglected. This surface energy is a factor in the formation of a metastable phase, which is a local minimized state. The formation of the metastable phase can improve the catalytic properties and perform new functions because the activation energy of the reaction changes with the change in the Gibbs free energy. It has been reported that reducing the size of the material to the nanoscale can improve its properties and perform new functions[109-110, 112]. Gold nanoparticle catalysts are an example; bulk gold is practically inert. However, by decreasing the size of the gold particles to nanometers, the catalytic activity for the oxidation of CO, low-temperature water-gas shift reactions, and the reduction of nitrogen oxides can be improved[109-110, 112]. In the case of the oxygen reduction reaction, the size of the catalyst nanoparticles affects the activity[106-107, 116-117]. This indicates that the surface of the nanoparticles possesses a disordered structure, and this structure exhibits a significant effect on their behavior in catalyzing the chemical reaction.

Next, the effect of the disordered structure on ionic conduction is discussed. The ionic conductivity of a solid electrolyte is well related to its structure. In the case of

crystalline materials, ions are transferred between one site and another empty site. The ions migrate between empty sites via a different structure than the stable structure where the bonds of the ions are broken, and they form bonds again at another site. Therefore, the activation energy for migration to an empty site and the number of empty sites are the main factors that determine ionic conductivity. In the case of amorphous materials, the overall structure is arranged in a disordered manner, and it possesses a larger free volume than that of crystalline materials. Considering Li ion conduction in this amorphous material as an example, Li ion conduction occurs as a result of the Li movement around the anions in the matrix. Therefore, ionic conduction occurs due to a mechanism different from that involved in a crystalline structure. Therefore, the activation energy of the reaction changes as the potentials of both the initial and the end states change by metastable phase formation, which is expected to affect the ionic conductivity. Amorphous materials are often synthesized by supplying high energy that is higher than the activation energy between the stable and metastable phases, from external sources such as heat, pressure and mechanical energy. The amorphous materials synthesized using this method exhibit properties different from those of the crystalline materials, for example, Li_3PS_4, a sulfide solid electrolyte. The ionic conductivity of crystalline Li_3PS_4 is reported to be low owing to the low accessibility of adjacent sites; however, it has been reported that the ionic conductivity of this material can be improved upon changes to an amorphous structure[49-50]. Hence, it is reported that fast ionic conduction can be achieved by converting the material from a stable to a metastable phase.

As described above, these disordered materials can be formed by applying high external energy to the material by heat, pressure, and mechanical methods or by increasing the surface energy by nanoparticulation. These disordered materials possess a

structure different from those of the ordered materials, and this affects properties such as catalyst activation and ion conduction mechanisms. Thus far, numerous studies on crystal materials to improve the property of the materials have been conducted. For further development of electrochemical materials, it is very important to develop a wide range of materials, including those with disordered materials. To develop disordered materials, it is necessary to determine the influence of disordered structures on the properties of materials. The disordered materials is not a completely random structure, but it exhibits a short-range order because it is a local minimized state. This short-range order contributes significantly to its properties. Therefore, it is very important to evaluate the short-range order structure and relate it to the properties. However, it is difficult to evaluate the short-range order structure, and in many cases, the relationship between the structure and properties is unclear.

1.4.2. Structural Analysis of Disordered Materials

As mentioned above, the disordered structures in nanoparticles and amorphous materials exhibit a significant effect on their properties. Therefore, structural characterization is important to elucidate the relationship between the disordered structure and properties for improving the properties of these materials.

These materials are characterized by XRD and XAFS measurements. Conventional XRD measurements provide information on the atomic structure of the sample by analyzing only the Bragg peaks. In this process, diffuse scattering caused by the disordered structure is removed[28-31]. Therefore, it is difficult to evaluate nanostructures and amorphous structures. EXAFS can be used to characterize the local atomic structure of any material regardless of the degree of the atomic order[32-34]. However,

the structural information obtained from EXAFS is limited to the first few coordination shells around the atoms; hence, it difficult to fully characterize the structure of the disordered material.

Therefore, high-energy XRD coupled with pair distribution function (PDF) analysis was focused. The PDF, $G(r)$, is obtained as the Fourier transform of the structure factor $S(Q)$, as shown in the following equations. $S(Q)$ is the scattering intensity normalized (by coherent scattering intensity, with corrections for background, absorption, multiple scattering, and inelastic scattering) to the number of atoms to obtain the scattering intensity per atom. The structure factor $S(Q)$ includes not only information about the Bragg peaks but also information about the weak diffuse-scattering component. The Bragg peaks contain information about the average periodic structure of the material. Diffuse scattering occurs as a broad peak and contains information about the disordered structure. In the conventional structure analysis, this diffuse scattering is subtracted from the data and not considered. In contrast, the PDF analysis is analyzed using $S(Q)$, which includes not only information about the Bragg peaks but also information about the weak diffuse scattering. Therefore, the PDF, $G(r)$, can provide structural information about the material that cannot be obtained from long-period structures. The resolution of the PDF is determined by the Q region, and a large Q region is required for accurate structural analysis. Therefore, the PDF analysis is often coupled with high-energy XRD measurements.

$$S(Q) = \frac{I_{coh}(Q) - \langle f(Q)^2 \rangle}{\langle f(Q) \rangle^2} + 1 \quad \left(Q = \frac{4\pi \sin(\theta)}{\lambda}\right) \qquad \text{eq. 10}$$

$$G(r) = \left(\frac{2}{\pi}\right) \int_{Q_{min}}^{Q_{max}} Q(S(Q) - 1) \sin(Qr) dQ \qquad \text{eq. 11}$$

The pair distribution function (PDF), G(*r*), expresses the existence probability of atoms present at distance *r*. The position and intensity of a peak in the PDF indicate the interatomic distance and coordination number, respectively, and the most simple local structure analysis in PDF analysis provides the bond lengths and coordination number directly from the peak positions and intensities by peak fitting.

Disordered materials, such as amorphous and nanoparticle materials, possess a short-range ordered structure, although they do not have long-range order because they are in a locally stable state. The short-range order in the structure exhibits a significant influence on the material properties. The diffuse scattering component of diffraction provides information on the short-range order structure; however, this information has been removed from previous analyses. In previous studies, the disordered materials has been discussed in terms of structural changes that do not include the short-range order structure. In contrast, high-energy XRD measurements coupled with PDF analysis use all the scattered components and do not exclude the information on the short-range ordered structure. In addition, the existence of atoms over a wide real-space distance can be established; hence, in the case of nanoparticles, structural information about the entire particle can be obtained. Thus, the combination of high-energy XRD measurements with the PDF analysis is an effective method for the structural evaluation of disordered materials such as nanoparticles and amorphous materials.

1.5. Objectives

As mentioned above, disordered materials, such as nanoparticles and amorphous materials, are important for improving the performance of electrochemical devices, and

the exploration of these materials is underway. To further improve their properties, it is necessary to understand the influence of disordered structures in disordered materials. The high-energy XRD measurements coupled with PDF analysis has received significant attention as a structural method for materials with disordered structures. This method applies not only to Bragg scattering but also to diffuse scattering, both of which provide periodic and aperiodic structural information. Therefore, even materials with disordered structures can be analyzed in detail, and it is a suitable method to investigate the effect of structure on the properties of these materials.

In this study, we report that electrochemical materials with a disordered structure, such as Pt nanoparticle catalysts and amorphous solid electrolytes, can be subjected to a gradual structural transition by the application of externally controlled thermal energy. In addition, these structural changes can be revealed using high-energy XRD measurements and PDF analysis. From the correlation between the structural change and the material properties, the effect of the short-range order structure of the disordered materials on the material properties can be revealed. Moreover, the main factors of disordered materials, understanding of which is important for developing principles for new functional materials, can be determined by the correlation between the structure and the properties of these materials.

1.6. Outline of the Present Thesis

The present thesis consists of seven chapters, presenting the development of a method to analyze the surface structure of nanoparticle catalysts, the optimization of synthesis conditions for liquid-phase synthesis of sulfur solid electrolytes, and the

elucidation of the factors controlling the properties of Li halide-doped Li_3PS_4 using high-energy XRD measurements coupled with the PDF analysis.

Chapter 2 describes that Pt nanoparticle catalysts with different particle sizes were prepared by annealing, and their structures were characterized by high-energy XRD measurements coupled with the PDF analysis. In addition, a simple structural model was developed to extract information about the surface structure of the catalysts. The correlation between the structural information and the properties of the material is discussed.

Chapter 3 describes how the liquid-phase synthesis of Li_3PS_4, a sulfur solid electrolyte, was performed, and the residual amount of raw materials and the degree of crystallinity of Li_3PS_4 were quantitatively evaluated by high-energy XRD measurement coupled with the PDF analysis. The correlation between these factors and ionic conductivity is discussed.

In chapter 4, based on the optimization results of the synthesis conditions for the liquid-phase synthesis, we have attempted to improve the properties of the sulfur solid electrolyte synthesized using the liquid-phase method. The controlling factors of performance were determined by high-energy XRD measurement coupled with the PDF analysis, and the correlation with the ionic conductivity is discussed.

Chapter 5 presents the synthesis and annealing of LiI-doped Li_3PS_4. The structures of LiI-doped Li_3PS_4 were characterized by high-energy XRD measurements coupled with the PDF analysis. In addition, the controlling factors for the properties of these materials are discussed in terms of correlation between the structures and properties. The effect of these properties on the dendrite suppression capability is also discussed.

In chapter 7, conclusions obtained from the present study and application

prospects in future electrochemical devices are presented.

Reference

1. Dunn, B.; Kamath, H.; Tarascon, J. M., Electrical Energy Storage for the Grid: A Battery of Choices. *Science* **2011,** *334* (6058), 928-935.
2. Zubi, G.; Dufo-López, R.; Carvalho, M.; Pasaoglu, G., The lithium-ion battery: State of the art and future perspectives. *Renew. Sust. Energ. Rev.* **2018,** *89*, 292-308.
3. Wu, H.; Cui, Y., Designing nanostructured Si anodes for high energy lithium ion batteries. *Nano Today* **2012,** *7* (5), 414-429.
4. Islam, M. S.; Fisher, C. A. J., Lithium and sodium battery cathode materials: computational insights into voltage, diffusion and nanostructural properties. *Chem. Soc. Rev.* **2014,** *43* (1), 185-204.
5. Seh, Z. W.; Sun, Y.; Zhang, Q.; Cui, Y., Designing high-energy lithium–sulfur batteries. *Chem. Soc. Rev.* **2016,** *45* (20), 5605-5634.
6. Wang, C.; Nehrir, M. H., Power management of a stand-alone wind/photovoltaic/fuel cell energy system. *IEEE Trans. Energy Convers.* **2008,** *23* (3), 957-967.
7. Bai, W.; Abedi, M. R.; Lee, K. Y., Distributed generation system control strategies with PV and fuel cell in microgrid operation. *Control. Eng. Pract.* **2016,** *53*, 184-193.
8. Bigdeli, N., Optimal management of hybrid PV/fuel cell/battery power system: A comparison of optimal hybrid approaches. *Renew. Sust. Energ. Rev.* **2015**, *42*, 377-393.
9. Frackowiak, E., Carbon materials for supercapacitor application. *Phys. Chem. Chem. Phys.* **2007,** *9* (15), 1774-1785.
10. Conway, B. E., Transition from Supercapacitor to Battery Behavior in Electrochemical Energy-Storage. *J. Electrochem. Soc.* **1991,** *138* (6), 1539-1548.
11. Grove, W. R., On a Gaseous Voltaic Battery. *Philosophical Magazine* **2012,** *92* (31),

3753-3756.

12. Hickner, M. A.; Ghassemi, H.; Kim, Y. S.; Einsla, B. R.; McGrath, J. E., Alternative polymer systems for proton exchange membranes (PEMs). *Chem. Rev.* **2004,** *104* (10), 4587-611.
13. Noel, J. M.; Yu, Y.; Mirkin, M. V., Dissolution of Pt at Moderately Negative Potentials during Oxygen Reduction in Water and Organic Media. *Langmuir* **2013,** *29* (5), 1346-1350.
14. Merte, L. R.; Behafarid, F.; Miller, D. J.; Friebel, D.; Cho, S.; Mbuga, F.; Sokaras, D.; Alonso-Mori, R.; Weng, T. C.; Nordlund, D.; Nilsson, A.; Cuenya, B. R., Electrochemical Oxidation of Size-Selected Pt Nanoparticles Studied Using in Situ High-Energy-Resolution X-ray Absorption Spectroscopy. *ACS Catal.* **2012,** *2* (11), 2371-2376.
15. Ishimoto, T.; Ogura, T.; Umeda, M.; Koyama, M., Theoretical study on dissolution and reprecipitation mechanism of Pt complex in Pt electrocatalyst. *J. Phys. Chem. C* **2011,** *115* (7), 3136-3142.
16. Ferreira, P. J.; la O, G. J.; Shao-Horn, Y.; Morgan, D.; Makharia, R.; Kocha, S.; Gasteiger, H. A., Instability of Pt/C electrocatalysts in proton exchange membrane fuel cells - A mechanistic investigation. *J. Electrochem. Soc.* **2005,** *152* (11), A2256-A2271.
17. Bi, W.; Fuller, T. F., Temperature Effects on PEM Fuel Cells Pt/C Catalyst Degradation. *J. Electrochem. Soc.* **2008,** *155* (2), B215-B221.
18. Li, L.; Hu, L.; Li, J.; Wei, Z., Enhanced stability of Pt nanoparticle electrocatalysts for fuel cells. *Nano Research* **2015**, *8*, 418-440.
19. De Bruijn, F. A.; Dam, V. A. T.; Janssen, G. J. M., Review: Durability and degradation

issues of PEM fuel cell components. *Fuel Cells* **2008,** *8* (1), 3-22.

20. Yasuda, K.; Taniguchi, A.; Akita, T.; Ioroi, T.; Siroma, Z., Platinum dissolution and deposition in the polymer electrolyte membrane of a PEM fuel cell as studied by potential cycling. *Phys. Chem. Chem. Phys.* **2006,** *8* (6), 746-752.
21. Han, K. S.; Moon, Y. S.; Han, O. H.; Hwang, K. J.; Kim, I.; Kim, H., Heat treatment and potential cycling effects on surface morphology, particle size, and catalytic activity of Pt/C catalysts studied by 13C NMR, TEM, XRD and CV. *Electrochem. Commun.* **2007,** *9* (2), 317-324.
22. Hammer, B.; Nørskov, J. K., Electronic factors determining the reactivity of metal surfaces. *Surf. Sci.* **1995,** *343* (3), 211-220.
23. Hammer, B.; Norskov, J. K., Theoretical surface science and catalysis - Calculations and concepts. In *Advances in Catalysis, Vol 45: Impact of Surface Science on Catalysis*, Gates, B. C.; Knozinger, H., Eds. Elsevier Academic Press Inc: San Diego, 2000; Vol. 45, pp 71-129.
24. Xu, Y.; Ruban, A. V.; Mavrikakis, M., Adsorption and Dissociation of O_2 on Pt-Co and Pt-Fe Alloys. *J. Am. Chem. Soc.* **2004**, *126*(14), 4717-4725.
25. Zhang, J.; Vukmirovic, M. B.; Xu, Y.; Mavrikakis, M.; Adzic, R. R., Controlling the Catalytic Activity of Platinum-Monolayer Electrocatalysts for Oxygen Reduction with Different Substrates. *Angew. Chem., Int. Ed.* **2005,** *44* (14), 2132-2135.
26. Mavrikakis, M.; Hammer, B.; Norskov, J. K., Effect of strain on the reactivity of metal surfaces. *Phys. Rev. Lett.* **1998,** *81* (13), 2819-2822.
27. Wang, X.; Orikasa, Y.; Takesue, Y.; Inoue, H.; Nakamura, M.; Minato, T.; Hoshi, N.; Uchimoto, Y., Quantitating the lattice strain dependence of monolayer Pt shell activity toward oxygen reduction. *J. Am. Chem. Soc.* **2013,** *135* (16), 5938-5941.

28. Borup, R. L.; Davey, J. R.; Garzon, F. H.; Wood, D. L.; Inbody, M. A., PEM fuel cell electrocatalyst durability measurements. *J. Power Sources* **2006,** *163* (1), 76-81.
29. Strasser, P.; Koh, S.; Anniyev, T.; Greeley, J.; More, K.; Yu, C.; Liu, Z.; Kaya, S.; Nordlund, D.; Ogasawara, H.; Toney, M. F.; Nilsson, A., Lattice-strain control of the activity in dealloyed core-shell fuel cell catalysts. *Nat. Chem.* **2010,** *2* (6), 454-460.
30. Temmel, S. E.; Fabbri, E.; Pergolesi, D.; Lippert, T.; Schmidt, T. J., Investigating the Role of Strain toward the Oxygen Reduction Activity on Model Thin Film Pt Catalysts. *ACS Catal.* **2016,** *6* (11), 7566-7576.
31. Escudero-Escribano, M.; Malacrida, P.; Hansen, M. H.; Vej-Hansen, U. G.; Velazquez-Palenzuela, A.; Tripkovic, V.; Schiotz, J.; Rossmeisl, J.; Stephens, I. E. L.; Chorkendorff, I., Tuning the activity of Pt alloy electrocatalysts by means of the lanthanide contraction. *Science* **2016,** *352* (6281), 73-76.
32. Yoshida, H.; Kinumoto, T.; Iriyama, Y.; Uchimoto, Y.; Ogumi, Z., XAS Study for Degradation Mechanism of Pt/C Catalyst During Potential Cycling Test. *ECS Trans.* **2007,** *11* (1), 1321-1329.
33. Imai, H.; Matsumoto, M.; Miyazaki, T.; Kato, K.; Tanida, H.; Uruga, T., Growth limits in platinum oxides formed on Pt-skin layers on Pt–Co bimetallic nanoparticles. *Chem. Commun.* **2011,** *47* (12), 3538-3538.
34. Imai, H.; Izumi, K.; Matsumoto, M.; Kubo, Y.; Kato, K.; Imai, Y., In Situ and Real-Time Monitoring of Oxide Growth in a Few Monolayers at Surfaces of Platinum Nanoparticles in Aqueous Media. *J. Am. Chem. Soc.* **2009,** *131* (17), 6293-6300.
35. Goodenough, J. B.; Kim, Y., Challenges for Rechargeable Li Batteries. *Chem. Mater.* **2010,** *22* (3), 587-603.
36. Goodenough, J. B.; Park, K. S., The Li-ion rechargeable battery: A perspective. *J.*

Am. Chem. Soc. **2013,** *135* (4), 1167-1176.

37. Whittingham, M. S., Lithium Batteries and Cathode Materials. *Chem. Rev.* **2004,** *104* (10), 4271-4302.
38. Simon, P.; Gogotsi, Y., Materials for electrochemical capacitors. *Nat. Mater.* **2008,** *7* (11), 845-854.
39. Tatsumisago, M.; Nagao, M.; Hayashi, A., Recent development of sulfide solid electrolytes and interfacial modification for all-solid-state rechargeable lithium batteries. *J. Asian Ceram. Soc.* **2013,** *1* (1), 17-25.
40. Hayashi, A.; Sakuda, A.; Tatsumisago, M., Development of Sulfide Solid Electrolytes and Interface Formation Processes for Bulk-Type All-Solid-State Li and Na Batteries. *Front. Energy Res.* **2016,** *4*, 25-25.
41. Inaguma, Y.; Liquan, C.; Itoh, M.; Nakamura, T.; Uchida, T.; Ikuta, H.; Wakihara, M., High ionic conductivity in lithium lanthanum titanate. *Solid State Commun.* **1993,** *86* (10), 689-693.
42. Murugan, R.; Thangadurai, V.; Weppner, W., Fast Lithium Ion Conduction in Garnet-Type $Li_7La_3Zr_2O_{12}$. *Angew. Chem., Int. Ed.* **2007,** *46* (41), 7778-7781.
43. Kamaya, N.; Homma, K.; Yamakawa, Y.; Hirayama, M.; Kanno, R.; Yonemura, M.; Kamiyama, T.; Kato, Y.; Hama, S.; Kawamoto, K.; Mitsui, A., A lithium superionic conductor. *Nat. Mater.* **2011,** *10* (9), 682-686.
44. Rangasamy, E.; Liu, Z.; Gobet, M.; Pilar, K.; Sahu, G.; Zhou, W.; Wu, H.; Greenbaum, S.; Liang, C., An Iodide-Based $Li_7P_2S_8I$ Superionic Conductor. *J. Am. Chem. Soc.* **2015,** *137* (4), 1384-1387.
45. Nagao, M.; Kitaura, H.; Hayashi, A.; Tatsumisago, M., High Rate Performance, Wide Temperature Operation and Long Cyclability of All-Solid-State Rechargeable

Lithium Batteries Using Mo-S Chevrel-Phase Compound. *J. Electrochem. Soc.* **2013,** *160* (6), A819-A823.

46. Miura, A.; Rosero-Navarro, N. C.; Sakuda, A.; Tadanaga, K.; Phuc, N. H. H.; Matsuda, A.; Machida, N.; Hayashi, A.; Tatsumisago, M., Liquid-phase syntheses of sulfide electrolytes for all-solid-state lithium battery. *Nat. Rev. Chem.* **2019,** *3* (3), 189-198.
47. Kato, Y.; Hori, S.; Saito, T.; Suzuki, K.; Hirayama, M.; Mitsui, A.; Yonemura, M.; Iba, H.; Kanno, R., High-power all-solid-state batteries using sulfide superionic conductors. *Nat. Energy* **2016,** *1* (4), 16030-16030.
48. Du, Y. A.; Holzwarth, N. A. W., Mechanisms of Li^+ diffusion in crystalline γ- and β-Li_3PO_4 electrolytes from first principles. *Phys. Rev. B* **2007,** *76*, 1-14.
49. Hong, H. Y. P., Crystal structure and ionic conductivity of $Li_{14}Zn(GeO_4)_4$ and other new Li^+ superionic conductors. *Mater. Res. Bull.* **1978,** *13*, 117-124.
50. Shannon, R. D.; Taylor, B. E.; English, A. D.; Berzins, T., New Li solid electrolytes. *Electrochimi. Acta* **1977,** *22*, 783-796.
51. Gromov, O. G.; Kunshina, G. B.; Kuz'min, A. P.; Kalinnikov, V. T., Ionic conductivity of solid electrolytes based on $Li_{1.3}Al_{0.3}Ti_{1.7}(PO_4)_3$. *Russ. J. Appl. Chem.* **1996,** *69*, 385-388.
52. Kubanska, A.; Castro, L.; Tortet, L.; Schäf, O.; Dollé, M.; Bouchet, R., Elaboration of controlled size $Li_{1.5}Al_{0.5}Ge_{1.5}(PO_4)_3$ crystallites from glass-ceramics. *Solid State Ionics* **2014,** *266*, 44-50.
53. Norhaniza, R.; Subban, R. H. Y.; Mohamed, N. S., Cr and V substituted $LiSn_2P_3O_{12}$ solid electrolyte materials. *J. Power Sources* **2013,** *244*, 300-305.
54. Ortiz, G. F.; López, M. C.; Lavela, P.; Vidal-Abarca, C.; Tirado, J. L., Improved

lithium-ion transport in NASICON-type lithium titanium phosphate by calcium and iron doping. *Solid State Ionics* **2014,** *262*, 573-577.

55. Subramanian, M. A.; Subramanian, R.; Clearfield, A., Lithium ion conductors in the system $AB(IV)_2(PO_4)_3$ (B = Ti, Zr and Hf). *Solid State Ionics* **1986,** *18-19*, 562-569.
56. Thangadurai, V.; Shukla, A. K.; Gopalakrishnan, J., New lithium-ion conductors based on the NASICON structure. *J. Mater. Chem.* **1999,** *9*, 739-741.
57. Breuer, S.; Prutsch, D.; Ma, Q.; Epp, V.; Preishuber-Pflügl, F.; Tietz, F.; Wilkening, M., Separating bulk from grain boundary Li ion conductivity in the sol-gel prepared solid electrolyte $Li_{1.5}Al_{0.5}Ti_{1.5}(PO_4)_3$. *J. Mater. Chem. A* **2015,** *3*, 21343-21350.
58. Fu, J., Superionic conductivity of glass-ceramics in the system Li_2O-Al_2O_3-TiO_2-P_2O_5. *Solid State Ionics* **1997,** *96*, 195-200.
59. Pershina, S. V.; Antonov, B. D.; Farlenkov, A. S.; Vovkotrub, E. G., Glass-ceramics in $Li_{1+x}Al_xGe_{2-x}(PO_4)_3$ system: The effect of Al_2O_3 addition on microstructure, structure and electrical properties. *J. Alloys Compound.* **2020,** *835*, 155281.
60. Xu, X.; Wen, Z.; Yang, X.; Zhang, J.; Gu, Z., High lithium ion conductivity glass-ceramics in Li_2O-Al_2O_3-TiO_2-P_2O_5 from nanoscaled glassy powders by mechanical milling. *Solid State Ionics* **2006,** *177*, 2611-2615.
61. Awaka, J.; Kijima, N.; Hayakawa, H.; Akimoto, J., Synthesis and structure analysis of tetragonal $Li_7La_3Zr_2O_{12}$ with the garnet-related type structure. *J Solid State Chem* **2009,** *182*, 2046-2052.
62. O'Callaghan, M. P.; Lynham, D. R.; Cussen, E. J.; Chen, G. Z., Structure and ionic-transport properties of lithium-containing garnets $Li_3Ln_3Te_2O_{12}$ (Ln = Y, Pr, Nd, Sm-Lu). *Chem. Mater.* **2006,** *18*, 4681-4689.
63. Thangadurai, V.; Narayanan, S.; Pinzaru, D., Garnet-type solid-state fast Li ion

conductors for Li batteries: Critical review. *Chem. Soc. Rev.* **2014,** *43*, 4714-4727.

64. Thangadurai, V.; Weppner, W., $Li_6ALa_2Ta_2O_{12}$ (A=Sr, Ba): Novel garnet-like oxides for fast lithium ion conduction. *Adv. Funct. Mater.* **2005,** *15*, 107-112.
65. Bohnke, O.; Bohnke, C.; Fourquet, J. L., Mechanism of ionic conduction and electrochemical intercalation of lithium into the perovskite lanthanum lithium titanate. *Solid State Ionics* **1996,** *91*, 21-31.
66. Harada, Y.; Ishigaki, T.; Kawai, H.; Kuwano, J., Lithium ion conductivity of polycrystalline perovskite $La_{0.67-x}Li_{3x}TiO_3$ with ordered and disordered arrangements of the A-site ions. *Solid State Ionics* **1998,** *108*, 407-413.
67. Stramare, S.; Thangadurai, V.; Weppner, W., Lithium Lanthanum Titanates: A Review. *Chem. Mater.* **2003,** *15*, 3974-3990.
68. Inaguma, Y.; Liquan, C.; Itoh, M.; Nakamura, T.; Uchida, T.; Ikuta, H.; Wakihara, M., High ionic conductivity in lithium lanthanum titanate. *Solid State Commun.* **1993,** *86*, 689-693.
69. Sakuda, A.; Hayashi, A.; Tatsumisago, M., Sulfide Solid Electrolyte with Favorable Mechanical Property for All-Solid-State Lithium Battery. *Sci. Rep.* **2013,** *3* (1), 2261-2261.
70. Nam, Y. J.; Cho, S.-J.; Oh, D. Y.; Lim, J.-M.; Kim, S. Y.; Song, J. H.; Lee, Y.-G.; Lee, S.-Y.; Jung, Y. S., Bendable and Thin Sulfide Solid Electrolyte Film: A New Electrolyte Opportunity for Free-Standing and Stackable High-Energy All-Solid-State Lithium-Ion Batteries. *Nano Letters* **2015,** *15* (5), 3317-3323.
71. Tachez, M.; Malugani, J.; Mercier, R.; Robert, G., Ionic conductivity of and phase transition in lithium thiophosphate Li_3PS_4. *Solid State Ionics* **1984,** *14* (3), 181-185.
72. Kuhn, A.; Gerbig, O.; Zhu, C.; Falkenberg, F.; Maier, J.; Lotsch, B. V., A new ultrafast

superionic Li-conductor: Ion dynamics in $Li_{11}Si_2PS_{12}$ and comparison with other tetragonal LGPS-type electrolytes. *Phys. Chem. Chem. Phys.* **2014,** *16*, 14669-14674.

73. Deiseroth, H.-J.; Kong, S.-T.; Eckert, H.; Vannahme, J.; Reiner, C.; Zaiß, T.; Schlosser, M., Li_6PS_5X: A Class of Crystalline Li-Rich Solids With an Unusually High Li^+ Mobility. *Angew. Chem., Int. Ed.* **2008,** *120* (4), 767-770.
74. Kraft, M. A.; Culver, S. P.; Calderon, M.; Bocher, F.; Krauskopf, T.; Senyshyn, A.; Dietrich, C.; Zevalkink, A.; Janek, J.; Zeier, W. G., Influence of Lattice Polarizability on the Ionic Conductivity in the Lithium Superionic Argyrodites Li_6PS_5X (X = Cl, Br, I). *J. Am. Chem. Soc.* **2017,** *139* (31), 10909-10918.
75. Mo, Y.; Ping Ong, S.; Ceder, G., First Principles Study of the $Li_{10}GeP_2S_{12}$ Lithium Super Ionic Conductor Material. *Chem. Mater.* **2011,** *24*, 15-17.
76. Dietrich, C.; Koerver, R.; Gaultois, M. W.; Kieslich, G.; Cibin, G.; Janek, J.; Zeier, W. G., Spectroscopic characterization of lithium thiophosphates by XPS and XAS-a model to help monitor interfacial reactions in all-solid-state batteries. *Phys. Chem. Chem. Phys.* **2018,** *20*, 20088-20095.
77. Dietrich, C.; A. Weber, D.; Culver, S.; Senyshyn, A.; J. Sedlmaier, S.; Indris, S.; Janek, J.; G. Zeier, W., Synthesis, Structural Characterization, and Lithium Ion Conductivity of the Lithium Thiophosphate $Li_2P_2S_6$. *Inorg. Chem.* **2017,** *56*, 6681-6687.
78. Ohara, K.; Mitsui, A.; Mori, M.; Onodera, Y.; Shiotani, S.; Koyama, Y.; Orikasa, Y.; Murakami, M.; Shimoda, K.; Mori, K.; Fukunaga, T.; Arai, H.; Uchimoto, Y.; Ogumi, Z., Structural and electronic features of binary Li_2S-P_2S_5 glasses. *Sci. Rep.* **2016,** *6* (1), 1-9.
79. Ujiie, S.; Hayashi, A.; Tatsumisago, M., Preparation and ionic conductivity of (100-x)($0.8Li_2S{\cdot}0.2P_2S_5$)·xLiI glass-ceramic electrolytes. *J. Solid. State. Electrochem.*

2013, *17* (3), 675-680.

80. Ujiie, S.; Hayashi, A.; Tatsumisago, M., Structure, ionic conductivity and electrochemical stability of Li_2S-P_2S_5-LiI glass and glass-ceramic electrolytes. *Solid State Ionics* **2012,** *211*, 42-45.
81. Han, F.; Yue, J.; Zhu, X.; Wang, C., Suppressing Li Dendrite Formation in Li_2S-P_2S_5 Solid Electrolyte by LiI Incorporation. *Adv. Energy Mater.* **2018,** *8* (18), 2-7.
82. Suyama, M.; Kato, A.; Sakuda, A.; Hayashi, A.; Tatsumisago, M., Lithium dissolution/deposition behavior with Li_3PS_4-LiI electrolyte for all-solid-state batteries operating at high temperatures. *Electrochim. Acta* **2018,** *286*, 158-162.
83. Kato, T.; Yoshida, R.; Yamamoto, K.; Hirayama, T.; Motoyama, M.; West, W. C.; Iriyama, Y., Effects of sintering temperature on interfacial structure and interfacial resistance for all-solid-state rechargeable lithium batteries. *J. Power Sources* **2016,** *325*, 584-590.
84. Ohtomo, T.; Hayashi, A.; Tatsumisago, M.; Tsuchida, Y.; Hama, S.; Kawamoto, K., All-solid-state lithium secondary batteries using the $75Li_2S{\cdot}25P_2S_5$ glass and the $70Li_2S{\cdot}30P_2S_5$ glass-ceramic as solid electrolytes. *J. Power Sources* **2013,** *233*, 231-235.
85. Ohtomo, T.; Hayashi, A.; Tatsumisago, M.; Kawamoto, K., Glass electrolytes with high ion conductivity and high chemical stability in the system LiI-Li_2O-Li_2S-P_2S_5. *Electrochemistry* **2013,** *81*, 428-431.
86. Hayashi, A.; Hama, S.; Morimoto, H.; Tatsumisago, M.; Minami, T., Preparation of Li_2S-P_2S_5 Amorphous Solid Electrolytes by Mechanical Milling. *J. Am. Ceram. Soc.* **2004,** *84* (2), 477-479.
87. Muramatsu, H.; Hayashi, A.; Ohtomo, T.; Hama, S.; Tatsumisago, M., Structural

change of Li_2S-P_2S_5 sulfide solid electrolytes in the atmosphere. *Solid State Ionics* **2011,** *182* (1), 116-119.

88. Boulineau, S.; Courty, M.; Tarascon, J.-M.; Viallet, V., Mechanochemical synthesis of Li-argyrodite Li_6PS_5X (X=Cl, Br, I) as sulfur-based solid electrolytes for all solid state batteries application. *Solid State Ionics* **2012,** *221*, 1-5.
89. Auvergniot, J.; Cassel, A.; Ledeuil, J.-B.; Viallet, V.; Seznec, V.; Dedryvère, R., Interface Stability of Argyrodite Li_6PS_5Cl toward $LiCoO_2$, $LiNi_{1/3}Co_{1/3}Mn_{1/3}O_2$, and $LiMn_2O_4$ in Bulk All-Solid-State Batteries. *Chem. Mater.* **2017,** *29* (9), 3883-3890.
90. Murayama, M.; Kanno, R., Synthesis of New Lithium Ionic Conductor Thio-LISICON—Lithium Silicon Sulfides System. *J. Solid State Chem.* **2002,** *168* (1), 140-148.
91. Liu, Z.; Fu, W.; Payzant, E. A.; Yu, X.; Wu, Z.; Dudney, N. J.; Kiggans, J.; Hong, K.; Rondinone, A. J.; Liang, C., Anomalous High Ionic Conductivity of Nanoporous β-Li_3PS_4. *J. Am. Chem. Soc.* **2013,** *135* (3), 975-978.
92. Teragawa, S.; Aso, K.; Tadanaga, K.; Hayashi, A.; Tatsumisago, M., Liquid-phase synthesis of a Li_3PS_4 solid electrolyte using N-methylformamide for all-solid-state lithium batteries. *J. Mater. Chem. A* **2014,** *2* (14), 5095-5099.
93. Matsuda, A.; Muto, H.; H.H. Phuc, N., Preparation of Li_3PS_4 Solid Electrolyte by Liquid-Phase Shaking Using Organic Solvents with Carbonyl Group as Complex Forming Medium. *J. Jpn. Soc. Powder and Powder Metallurgy* **2016,** *63* (11), 976-980.
94. Phuc, N. H. H.; Morikawa, K.; Totani, M.; Muto, H.; Matsuda, A., Chemical synthesis of Li_3PS_4 precursor suspension by liquid-phase shaking. *Solid State Ionics* **2016,** *285*, 2-5.

95. Lim, H.-D.; Yue, X.; Xing, X.; Petrova, V.; Gonzalez, M.; Liu, H.; Liu, P., Designing solution chemistries for the low-temperature synthesis of sulfide-based solid electrolytes. *J. Mate. Chem. A* **2018,** *6* (17), 7370-7374.

96. Choi, S.; Lee, S.; Park, J.; Nichols, W. T.; Shin, D., Facile synthesis of Li_2S-P_2S_5 glass-ceramics electrolyte with micron range particles for all-solid-state batteries via a low-temperature solution technique (LTST). *Appl. Surf. Sci.* **2018,** *444*, 10-14.

97. Wang, H.; Hood, Z. D.; Xia, Y.; Liang, C., Fabrication of ultrathin solid electrolyte membranes of β-Li_3PS_4 nanoflakes by evaporation-induced self-assembly for all-solid-state batteries. *J. Mater. Chem. A* **2016,** *4* (21), 8091-8096.

98. Wang, Y.; Lu, D.; Bowden, M.; El Khoury, P. Z.; Han, K. S.; Deng, Z. D.; Xiao, J.; Zhang, J.-G.; Liu, J., Mechanism of Formation of $Li_7P_3S_{11}$ Solid Electrolytes through Liquid Phase Synthesis. *Chem. Mater.* **2018,** *30* (3), 990-997.

99. Suto, K.; Bonnick, P.; Nagai, E.; Niitani, K.; Arthur, T. S.; Muldoon, J., Microwave-aided synthesis of lithium thiophosphate solid electrolyte. *J. Mater. Chem. A* **2018,** *6* (43), 21261-21265.

100. Sakuda, A.; Kitaura, H.; Hayashi, A.; Tadanaga, K.; Tatsumisago, M., Improvement of high-rate performance of all-solid-state lithium secondary batteries using $LiCoO_2$ coated with Li_2O - SiO_2 glasses. *ECS Electrochem. Lett.* **2008,** *11* (1), A1-A3.

101. Sakuda, A.; Hayashi, A.; Hama, S.; Tatsumisago, M., Preparation of Highly Lithium-Ion Conductive $80Li_2S{\cdot}20P_2S_5$ Thin-Film Electrolytes Using Pulsed Laser Deposition. *J. Am. Ceram. Soc.* **2010,** *93* (3), 765-768.

102. Sakuda, A.; Hayashi, A.; Ohtomo, T.; Hama, S.; Tatsumisago, M., All-solid-state lithium secondary batteries using $LiCoO_2$ particles with pulsed laser deposition coatings of Li_2S-P_2S_5 solid electrolytes. *J. Power Sources* **2011,** *196* (16), 6735-6741.

103. Shiotani, S.; Ohara, K.; Tsukasaki, H.; Mori, S.; Kanno, R., Pair distribution function analysis of sulfide glassy electrolytes for all-solid-state batteries: Understanding the improvement of ionic conductivity under annealing condition. *Sci. Rep.* **2017,** *7* (1), 6972-6972.

104. Tsukasaki, H.; Mori, S.; Shiotani, S.; Yamamura, H., Ionic conductivity and crystallization process in the Li_2S–P_2S_5 glass electrolyte. *Solid State Ionics* **2018,** *317*, 122-126.

105. Phuc, N. H. H.; Morikawa, K.; Mitsuhiro, T.; Muto, H.; Matsuda, A., Synthesis of plate-like Li_3PS_4 solid electrolyte via liquid-phase shaking for all-solid-state lithium batteries. *Ionics* **2017,** *23* (8), 2061-2067.

106. Roldan Cuenya, B.; Behafarid, F., Nanocatalysis: Size- and shape-dependent chemisorption and catalytic reactivity. *Surface Science Reports* **2015**, *70*, 135-187.

107. Yano, H.; Inukai, J.; Uchida, H.; Watanabe, M.; Babu, P. K.; Kobayashi, T.; Chung, J. H.; Oldfield, E.; Wieckowski, A., Particle-size effect of nanoscale platinum catalysts in oxygen reduction reaction: An electrochemical and 195Pt EC-NMR study. *Phys. Chem. Chem. Phys.* **2006,** *8* (42), 4932-4939.

108. Wang, L.; Tsang, C. S.; Liu, W.; Zhang, X.; Zhang, K.; Ha, E.; Kwok, W. M.; Park, J. H.; Suk Lee, L. Y.; Wong, K. Y., Disordered layers on WO_3 nanoparticles enable photochemical generation of hydrogen from water. *J. Mater. Chem. A* **2019,** *7* (1), 221-227.

109. Haruta, M., Novel catalysis of gold deposited on metal oxides. *Catal. Surv. from Japan* **1997,** *1* (1), 61-73.

110. Deng, W.; Frenkel, A. I.; Si, R.; Flytzani-Stephanop, M., Reaction-relevant gold structures in the low temperature water-gas shift reaction on Au-CeO_2. *J. Phys. Chem.*

C **2008,** *112* (33), 12834-12840.

111. Chen, X.; Liu, L.; Yu, P. Y.; Mao, S. S., Increasing solar absorption for photocatalysis with black hydrogenated titanium dioxide nanocrystals. *Science* **2011,** *331* (6018), 746-750.

112. Aguilar-Guerrero, V.; Gates, B. C., Kinetics of CO oxidation catalyzed by supported gold: A tabular summary of the literature. *Catal. Lett.* **2009,** *130*, 108-120.

113. Wang, C.; Bai, S.; Xiong, Y., Recent advances in surface and interface engineering for electrocatalysis. *Chin. J. Catal.* **2015**, *36*, 1476-1493.

114. Stamenkovic, V. R.; Mun, B. S.; Arenz, M.; Mayrhofer, K. J. J.; Lucas, C. A.; Wang, G. F.; Ross, P. N.; Markovic, N. M., Trends in electrocatalysis on extended and nanoscale Pt-bimetallic alloy surfaces. *Nat. Mater.* **2007,** *6* (3), 241-247.

115. Stamenkovic, V. R.; Fowler, B.; Mun, B. S.; Wang, G.; Ross, P. N.; Lucas, C. A.; Markovic, N. M., Improved oxygen reduction activity on $Pt_3Ni(111)$ via increased surface site availability. *Science* **2007,** *315* (5811), 493-497.

116. Komanicky, V.; Iddir, H.; Chang, K.-C.; Menzel, A.; Karapetrov, G.; Hennessy, D.; Zapol, P.; You, H., Shape-Dependent Activity of Platinum Array Catalyst. *J. Am. Chem. Soc.* **2009,** *131* (16), 5732-5733.

117. Yano, H.; Higuchi, E.; Uchida, H.; Watanabe, M., Temperature Dependence of Oxygen Reduction Activity at Nafion-Coated Bulk Pt and Pt/Carbon Black Catalysts. *J. Phys. Chem. B* **2006,** *110* (33), 16544-16549.

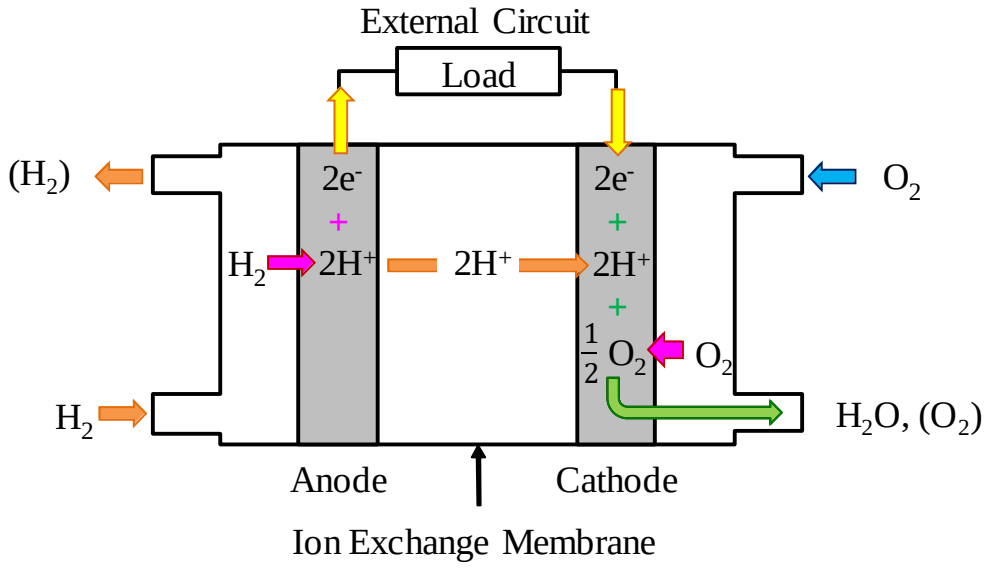

Figure 1. Schematic representation of a polymer electrolyte fuel cell.

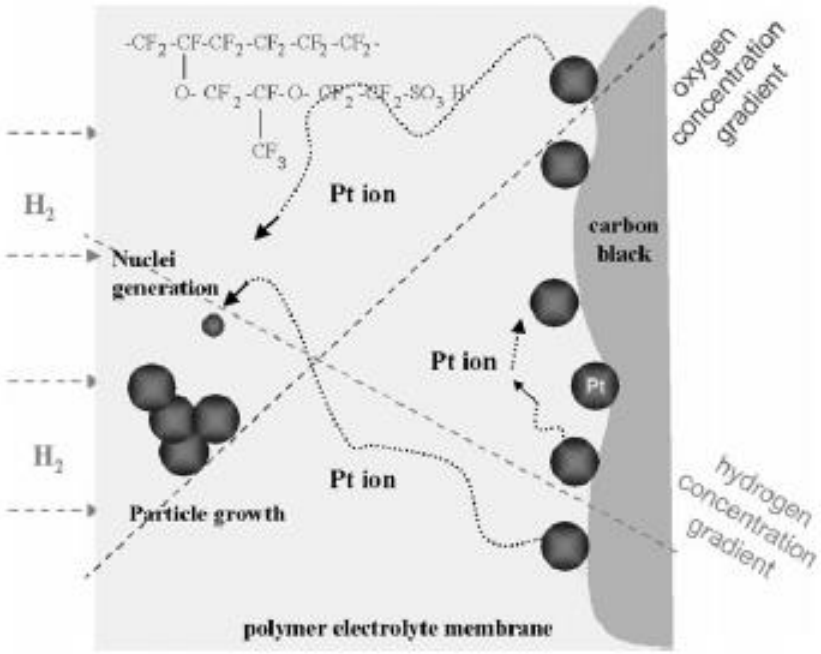

Figure 2. Degradation mechanism of Pt/C catalyst in a polymer electrolyte fuel cell[20].

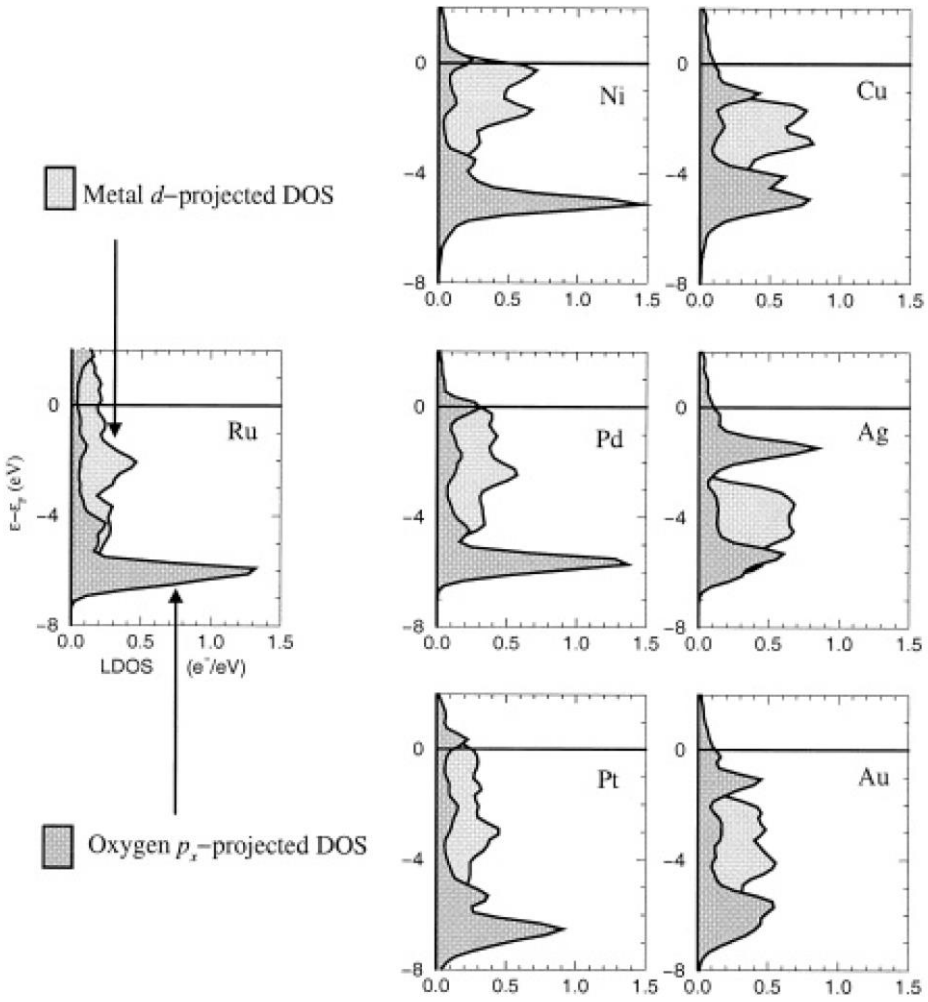

Figure 3. Schematic illustration of the change in local electronic structure at an oxygen atom upon adsorption on simple and transition/noble metal surfaces[23].

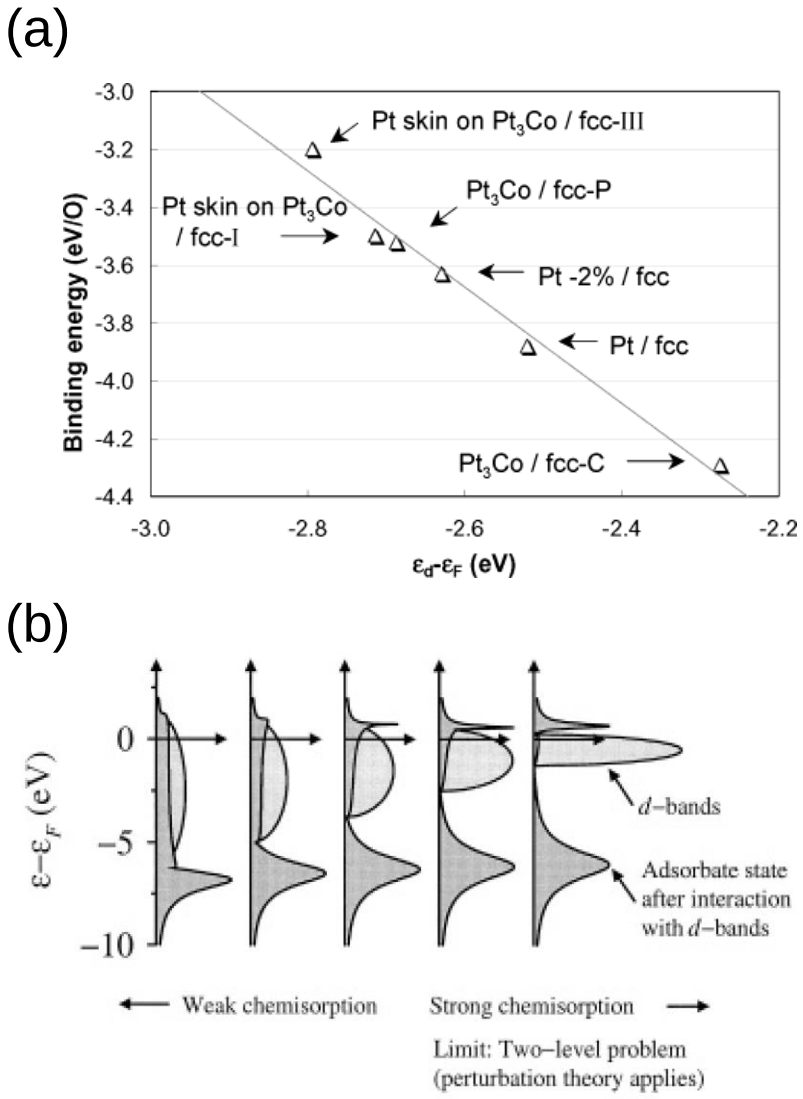

Figure 4. (a) Binding energies of atomic O vs d-band centers (ε_d) of the four clean surfaces. (b) The local den sity of states proj ected onto an adsorbate state intera cting with the d bands at a surface [20].

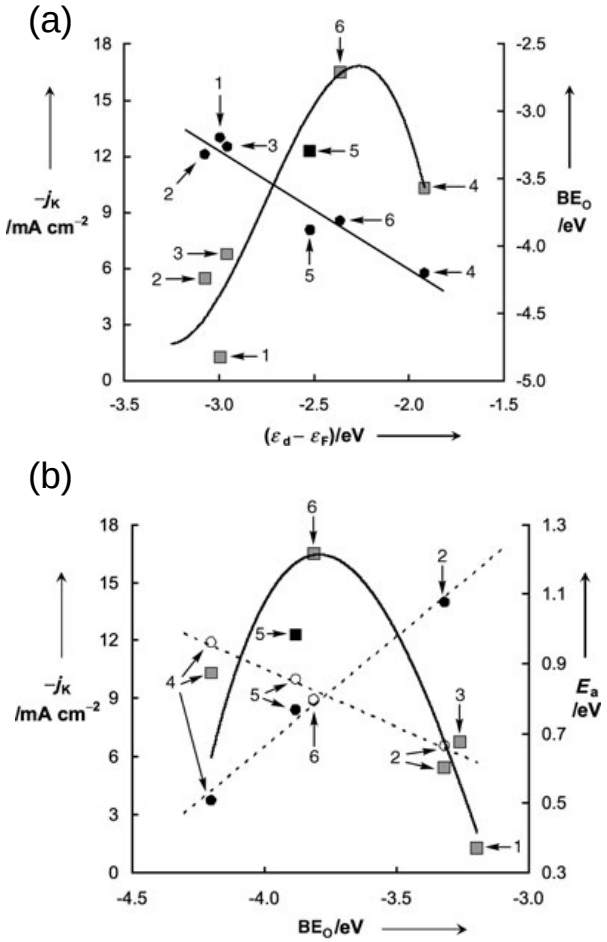

Figure 5. (a) Kinetic currents (j_K; square symbols) at 0.8 V for O_2 reduction on the platinum monolayers supported on different single-crystal surfaces in a 0.1m $HClO_4$ solution and calculated binding energies of atomic oxygen (BE_O; filled circles) as functions of calculated d-band center ($\varepsilon_d - \varepsilon_F$; relative to the Fermi level) of the respective clean platinum monolayers. Labels: 1. PtML/Ru(0001), 2. PtML/Ir(111), 3. PtML/Rh(111), 4. PtML/Au(111), 5. Pt(111), 6. PtML/Pd(111). (b) Kinetic currents (j_K; square symbols) at 0.8 V for O_2 reduction on the platinum monolayers in a 0.1m $HClO_4$ solution and the activation energies for O_2 dissociation (filled circles) and for OH formation (open circles) on PtML/Au(111), Pt(111), PtML/Pd(111), and PtML/Ir(111), as functions of the calculated binding energy of atomic oxygen (BE_O) [25].

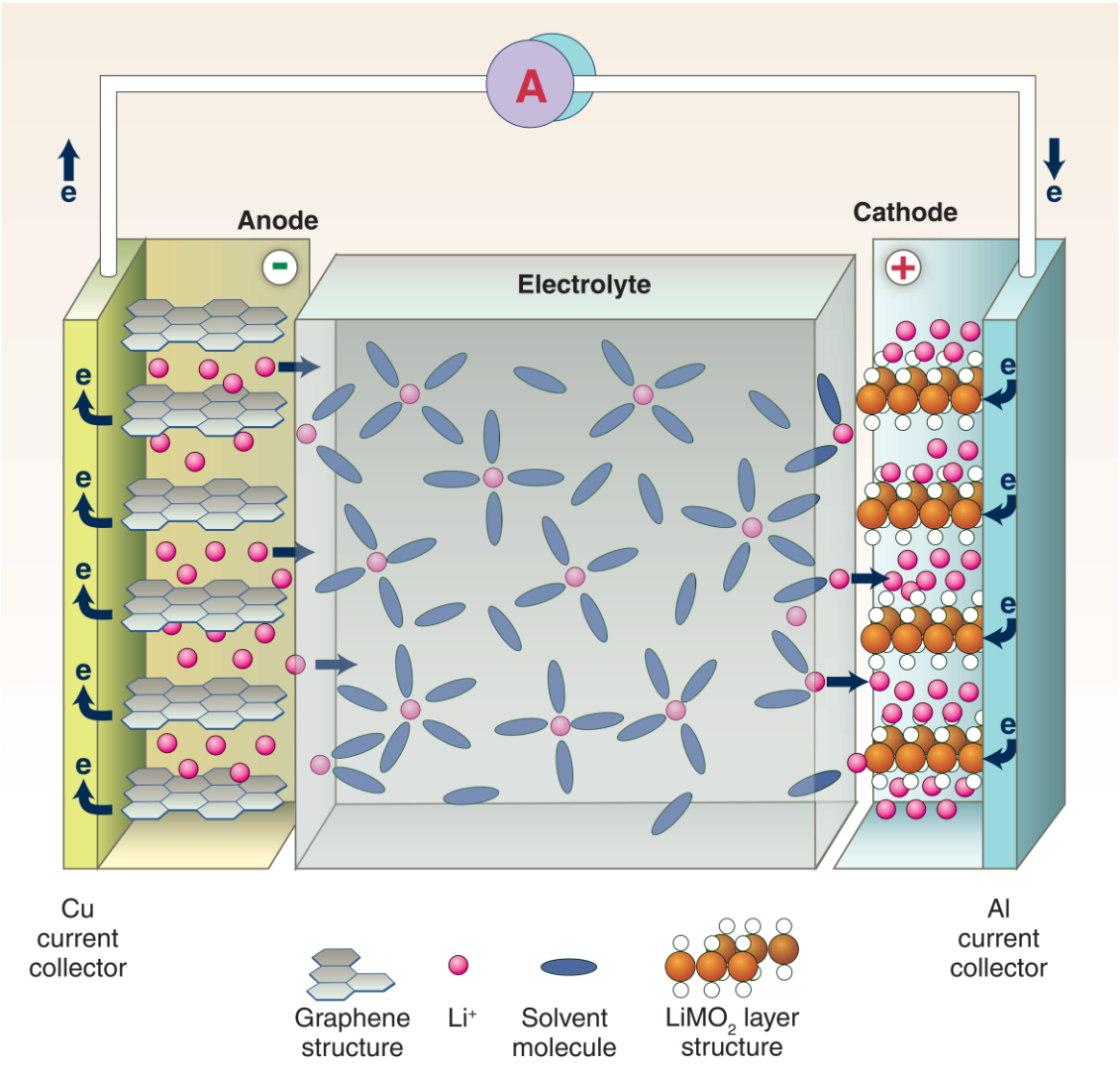

Figure 6. Schematic figure of lithium ion rechargeable battery[1].

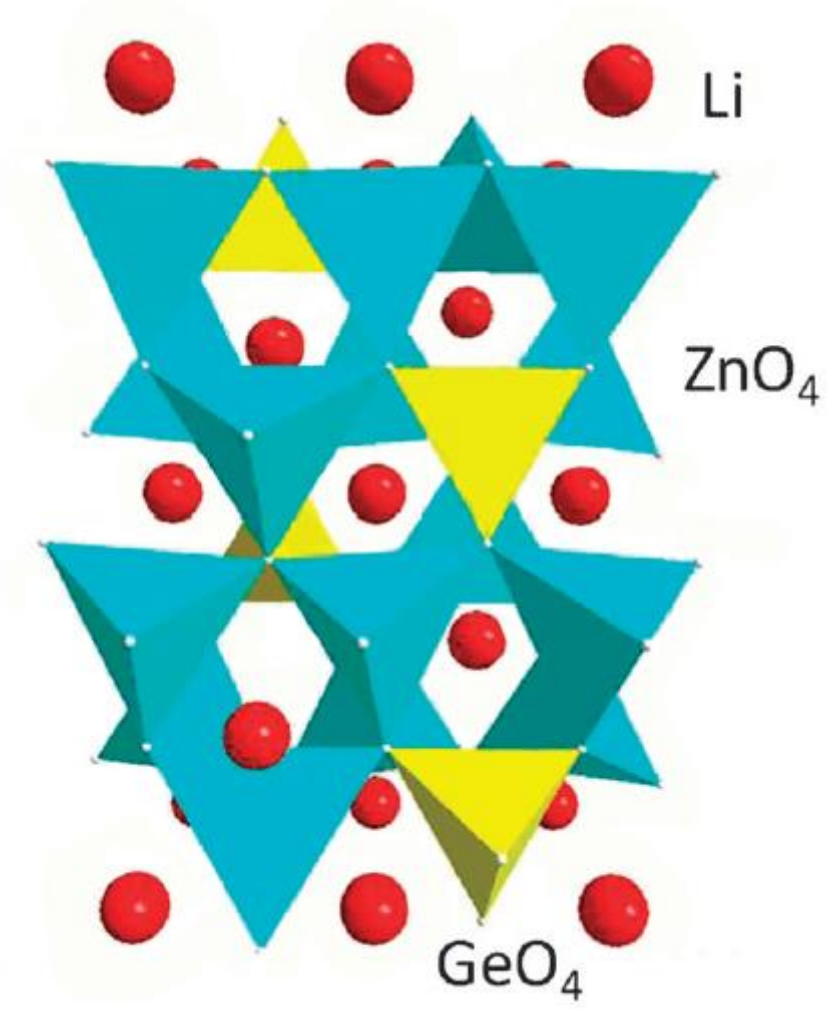

Figure 7. The crystal structure of The LISICON-like solid electrolyte using $Li_{14}Zn(GeO_4)_4$ as an example[49].

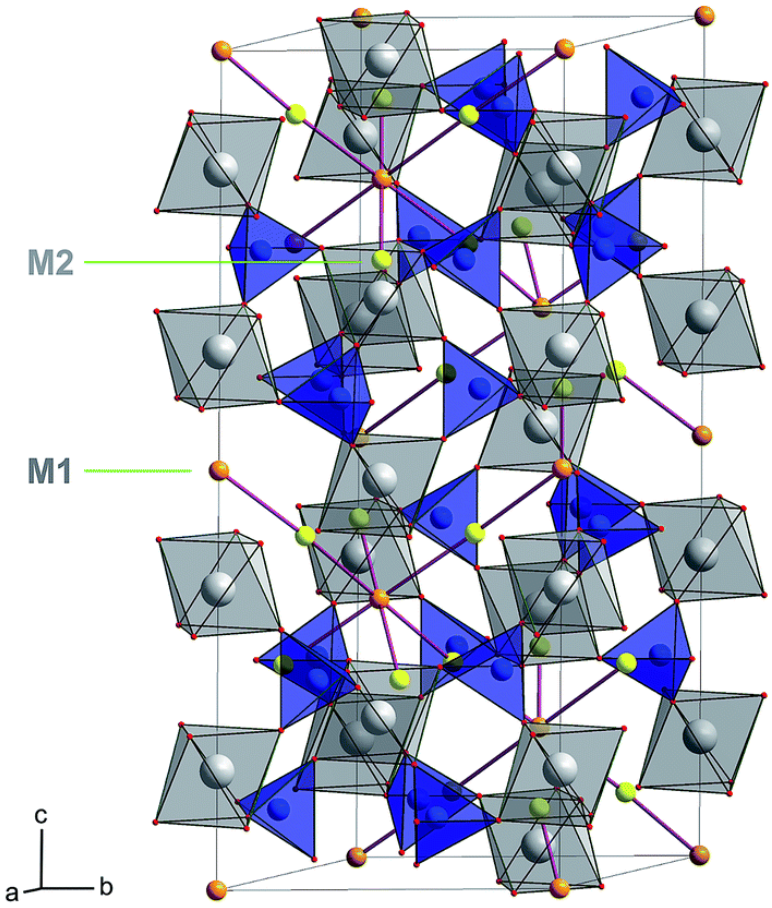

Figure 8. The crystal structure of The NASICON-type solid electrolyte using LATP as an example[57].

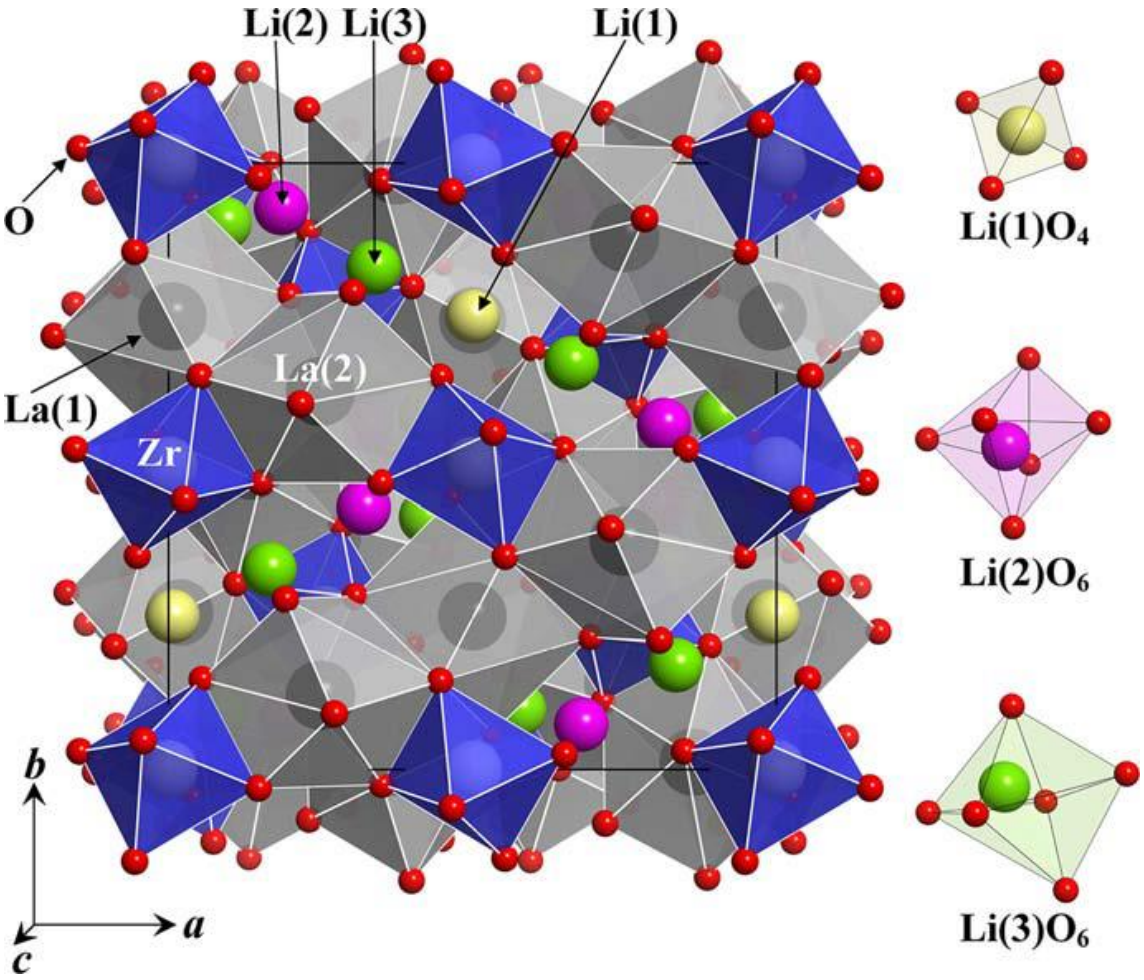

Figure 9. Crystal structure of Garnett-type solid electrolytes using $Li_7La_3Zr_2O_{12}$ as an example [61].

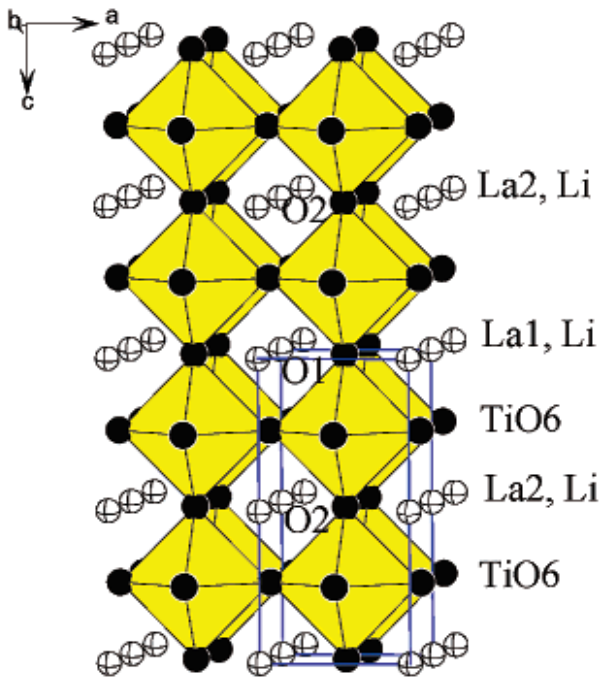

Figure 10. Crystal structure of perovskite-type solid electrolyte using $Li_{3x}La_{(2/3)-x}0_{(1/3)-2x}TiO_3$ (x = 0.11) as an example [67].

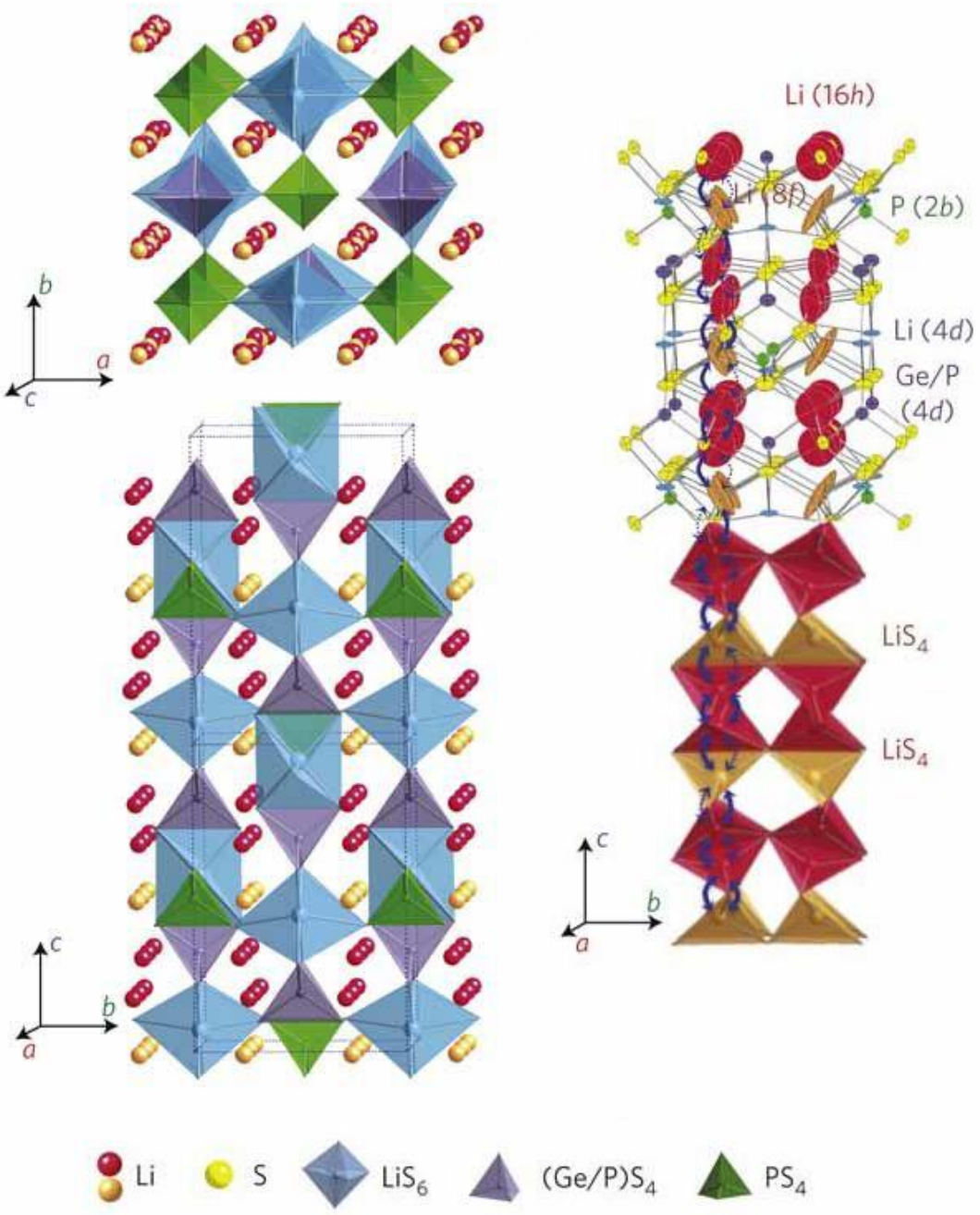

Figure 11. (a) The framework structure of $Li_{10}GeP_2S_{12}$ and lithium ions that participate in ionic conduction. (b) Conduction pathways of lithium ions.[43]

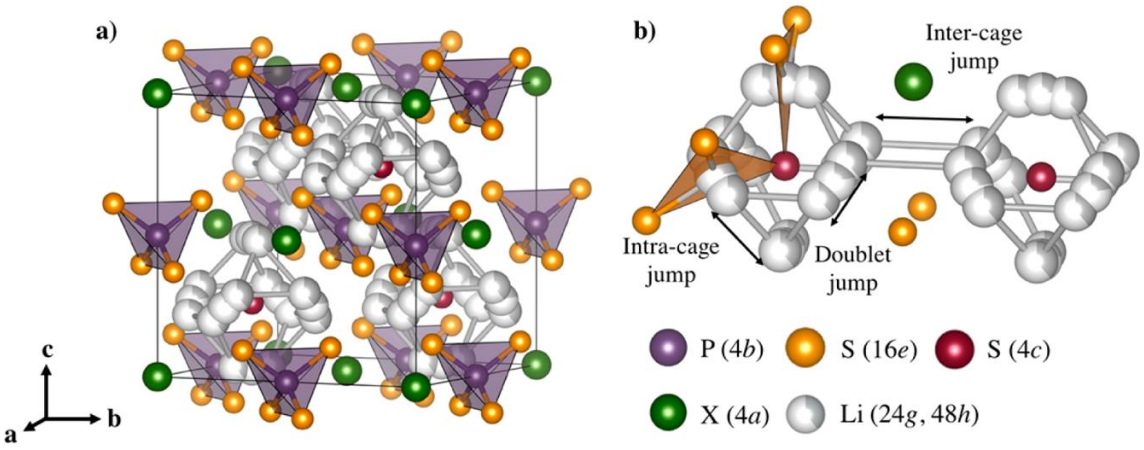

Figure 12. (a) Crystal structures of Li_6PS_5X with X = Cl, Br, I. In the ordered structure and (b) scheme of the inter-cage jumps[74].

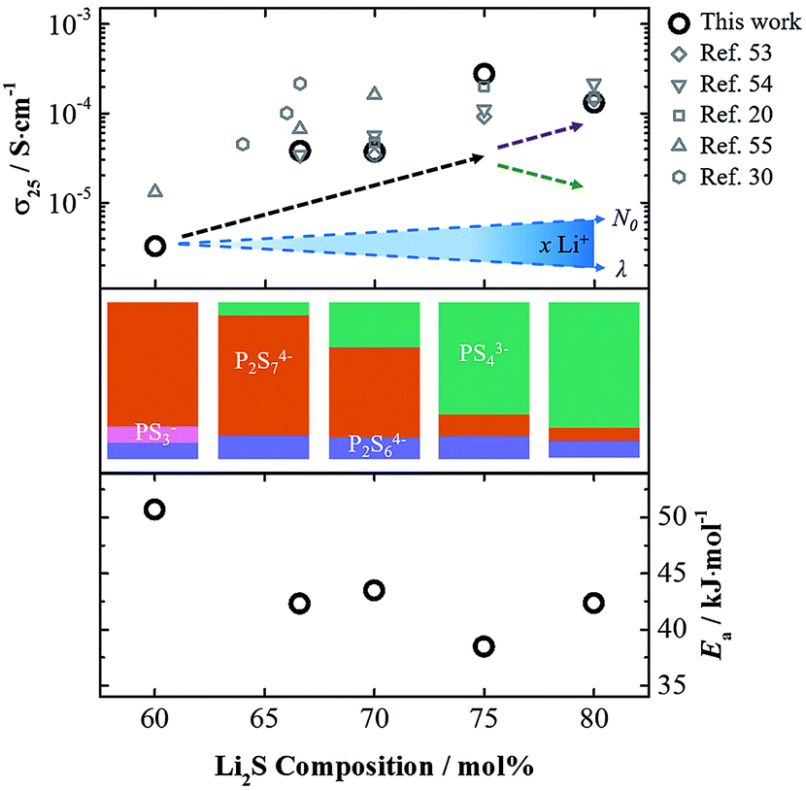

Figure 13. (Top) Variation of LPS glass and literature data on isothermal conductivity at room temperature with x. The arrows show the general trend of composition: at x > 75, two different trends are reported (green and purple arrows). (Middle) Colored bar graphs visualizing the percentages of various thiophosphate anions that affect transport properties. (Bottom) Activation energy of the ionic conductivity of LPS glass[77].

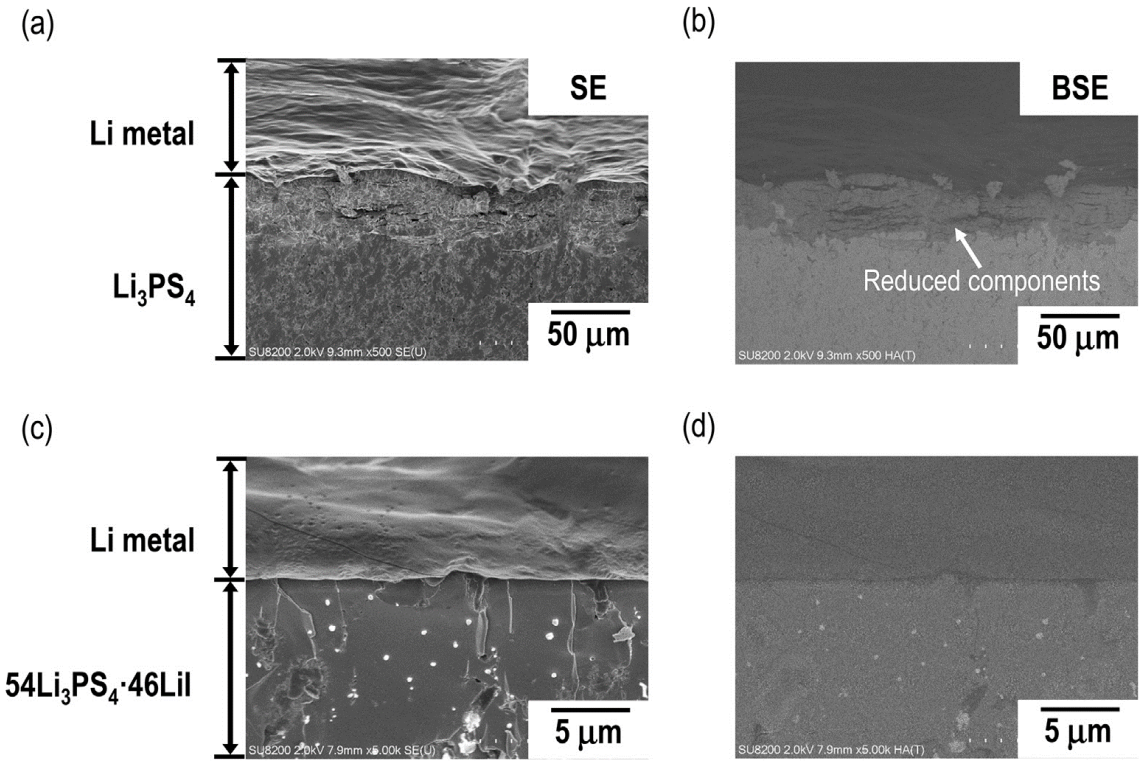

Figure 14. Cross-section SEM images of the Li/solid electrolyte interface after the Li dendrite evaluation test[82].

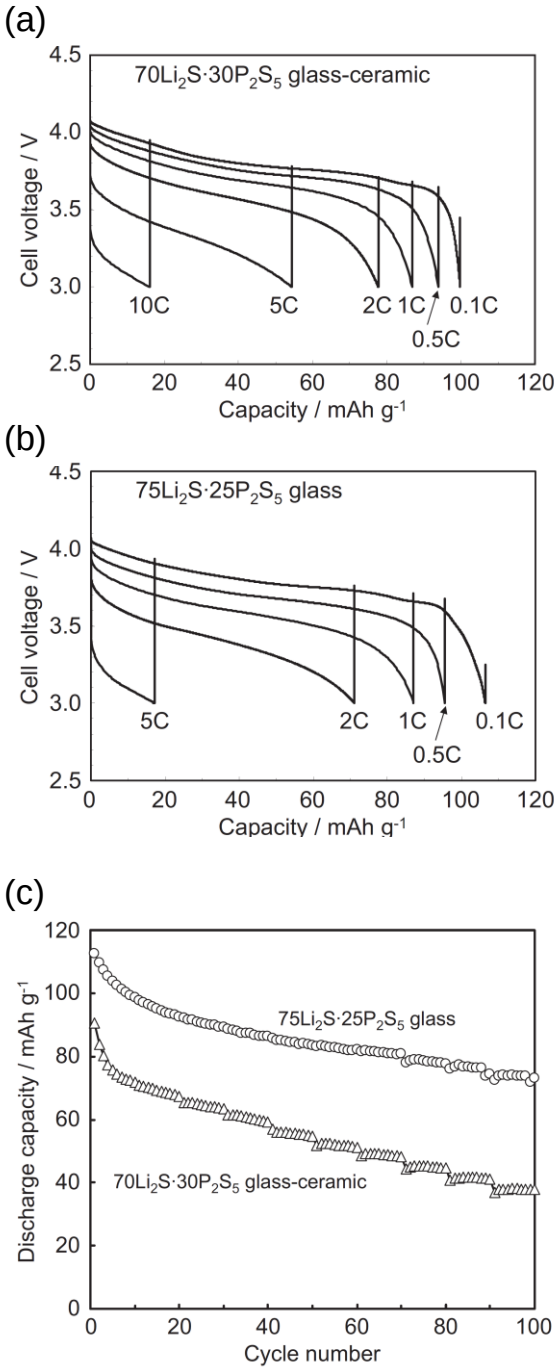

Figure 15. Discharge curves of the all-solid-state C/$LiCoO_2$ cells using the (a)70 Li_2S-30 P_2S_5 glass-ceramic and (b) the 75Li_2S-25P_2S_5 glass at room temperature. (c) Cycle performance of these cells [84].

Chapter 2. Observation of Subsurface Structure of Pt/C Catalyst Using Pair Distribution Function and Simple Modeling Techniques

2.1. Introduction

Polymer electrolyte membrane fuel cells (PEMFC), which are highly efficient and environmentally friendly, are used as a mobile power source in fuel cell vehicles (FCVs). Current FCVs need a precious Pt catalyst for the oxygen reduction reaction (ORR) of the rate-determining process in the PEMFC because of its high activity. The necessity of the Pt catalyst is no longer questionable, but this is not suitable owing to its high cost. Increasing the activity and the durability of the Pt catalyst to decrease the Pt amount would decrease its cost. Therefore, it is important to accurately evaluate a factor for determining the activity and durability of the Pt catalyst and to control them.

Hammer and Nørskov suggested in theoretical studies that the Pt-Pt interatomic distance in the subsurface is correlated with specific activity[1]. This suggestion is consistent with experimental results based on XAFS measurement using model structures such as core–shell and/or Pt skin structures, which indicates a correlation between the specific activity and the Pt-Pt interatomic distance[2,3]. However, it is difficult to separate the Pt–Pt interatomic distance at the subsurface and interior regions of the Pt nanoparticle

catalyst because XAFS measurements provide the average structural information of both regions within the closest interatomic distance, although nanoparticles have different Pt–Pt interatomic distances in the regions. In addition, the Pt–Pt interatomic distance depends on the nanoparticle size, which has been characterized by XAFS and powder X-ray diffraction[4,5]. Although XAFS and XRD measurements are powerful techniques to evaluate the average interatomic distance of bulk materials, they are not suitable to evaluate the Pt-Pt interatomic distance in the subsurface of the Pt catalyst because the ORR reaction occurs at the surface. Therefore, a structure analysis method that can be used to evaluate the Pt–Pt interatomic distance in the subsurface of catalysts, which have different lengths of Pt–Pt bonds by changing the particle size, is necessary.

In this study, total X-ray scattering measurement coupled with pair distribution function (PDF) analysis was carried out to evaluate the Pt–Pt interatomic distance in the subsurface of Pt catalysts with different particle size. The intensity of the PDF represents an atom abundance fraction from a certain atom to a distance r. Furthermore, the peak positions of the PDF present interatomic distances and they can obtain a much longer interatomic distance than XAFS measurement. A medium to long-range interatomic distance over the closest distance, which means the Pt-Pt correlation over the closest distance, can more accurately evaluate a change in interatomic distance than using the short-range interatomic distance. We tried to compare the results of XAFS measurement and PDF analysis for the Pt catalysts with different particle size, which means a comparison of structure information between the closest and medium to long-range interatomic distances at different particle sizes. The subsurface structure of the catalyst was previously discussed on the basis of simulations with three dimensional (3D) complex models[6–10]. We consider the usability of PDF and simple modeling techniques

using the medium to long-range interatomic distance.

2.2. Experimental Section

2.2.1. Preparation of Annealed Samples.

Annealed samples were prepared by heating a commercially available 30 wt% Pt/C catalyst (Tanaka Kikinzoku Kogyo, TEC10V30E) at 200, 400, 600, and 800°C in N_2 atmosphere for 2 h. Untreated and annealed samples were characterized and evaluated in terms of electrochemical activity. Samples were reduced by flowing 5% H_2-N_2 gas for 5 hours at room temperature before synchrotron measurement to remove the effect of oxygen on the Pt nanoparticle surface.

2.2.2. TEM, XAFS and XRD Measurements.

Changes in the shape and distribution of Pt nanoparticle size by annealing were observed by transmission electron microscopy (TEM) measurement. Specimens for TEM observations were prepared by powder dispersion techniques. Bright-field images were acquired with a TecnaiG2 F20 electron microscope (FEI Company) with an acceleration voltage of 200 kV. Average particle size, standard deviation, and particle size distribution were estimated from over 500 particles of black spots in the TEM images, that correspond to Pt particles.

Pellets of samples for XAFS measurement were prepared by the compression molding of BN powders and samples were mixed for 30 min. XAFS experiments of the L_{III}-edge were performed at the SPring-8 beamline BL01B1. The storage ring energy of SPring-8 was 8 GeV and the ring current was 100 mA. Energy scans in the range of 11.3–

13.1 keV using a double-crystal monochromator were conducted to obtain the XAFS spectra. In addition, the intensities of incident and transmission X-rays at each energy were measured. Moreover, XAFS spectra were obtained from the difference between the intensities of incident and transmission X-rays.

XRD measurements of untreated and annealed Pt/C catalysts were conducted at the SPring-8 beamline BL02B2. XRD measurements were carried out with the energy of synchrotron radiation set to 17.7 keV (0.7 Å) using a double-crystal monochromator of Si (111). XRD patterns were obtained between 2° to 78° at 0.006° intervals. RIETAN–FP was employed for the Rietveld analysis of XRD patterns[11].

2.2.3. High-Energy X-ray Total Scattering Measurement and Pair Distribution Function (PDF) Analysis.

High-energy total scattering measurements of all samples were carried out at the SPring-8 beamline BL04B2. The X-ray energy was 61.2 keV (0.2 Å) and the measurement range was 0.3° to 48° at 0.1° intervals. Scattering data of each sample was corrected for background, absorption correction, multiple scattering and inelastic scattering. The structure factor $S(Q)$ was calculated from the standardization of the corrected scattering data by the number of atoms and the scattering intensity from one atom. Moreover, the reduced PDF $G(r)$ was obtained by the Fourier transform of $S(Q)$. To evaluate the interatomic distance of Pt–Pt correlations in the subsurface region, simulation sphere models that have different particle diameters such as 2.4, 3.2, 4.0, and 4.8 nm were created on the basis of the crystalline structure of the bulk Pt. The Pt atoms were classified on the basis of the distance from the subsurface region to the interior region. We compared the relationship between the Pt–Pt correlations in the subsurface

region and the interatomic distances. $G(r)$ corresponding to the subsurface region was calculated using PDFgui software[12]. The initial parameter values were used, which were obtained by Rietveld analysis. The instrumental function was set to a value that was calculated by the curve fitting of $G(r)$ of the standard sample Ni.

2.2.4. Electrochemical Characterization.

Catalyst suspensions were prepared by the ultrasonic dispersion of a solution, which is a mixture of 5.521 mg of catalyst, 2.4 mL of 2-propanol (Wako Pure Chemical Industries, Wako Super Special Grade), 7.6 mL of ultrapure water and 40 μL 5 wt% Nafion® perfluorinated resin solution (Sigma-Aldrich). Catalyst–modified working electrodes were prepared by rotating dry glass carbon (GC) electrodes, which were cast with 10 μL of a prepared catalyst suspension on GC for 1 h. Electrochemical measurements were carried out in a three-electrode cell at 25°C. The counter electrode was a Pt mesh and the reference electrode was a reversible hydrogen electrode (RHE). The electrolyte was 0.1 M $HClO_4$ aq., which was prepared by diluting 60 wt% $HClO_4$ (Kanto Chemical Corporation, Ultrapure) with ultrapure water. Prior to the cyclic voltammetry (CV) measurement, cycles of potential (50 times) were carried out between 0.05 and 1.0 V vs. RHE at 200 mV s^{-1} in a N_2-saturated 0.1 M $HClO_4$ solution to clean the subsurface of the catalyst. CV measurements were performed between 0.05 and 1.0 V vs. RHE at 50 mV s^{-1} in a N_2-saturated 0.1 M $HClO_4$ solution at 3 cycles. The subsurface of the catalyst, which showed above at 10 cycles, was cleaned before each linear sweep voltammetry (LSV) measurement. LSV measurements were performed between 0.05 and 1.0 V vs. RHE and rotating speed between 100 and 2500 rpm at 10 mV s^{-1} scan rate in a N_2-saturated and O_2-saturated 0.1 M $HClO_4$ solution. The oxygen

reduction reaction currents of each sample were calculated with different current densities obtained in a N_2-saturated and O_2-saturated 0.1 M $HClO_4$ solution. The kinetically-controlled current was obtained by Koutecky–Levich plot using the oxygen reduction current at each rotating speed. Furthermore, mass activities and specific activities were calculated by standardizing the kinetically controlled current at the weight of the Pt catalyst and the electrochemically active surface area obtained by CV measurement. The electrochemical measurements were performed three times, and the validities were checked.

2.3. Results and Discussion

The average particle size of each sample obtained from TEM images (Figure 1) is summarized in Table 1. As can be seen in Table 1, the average particle size increased with increasing annealing temperature. It is consisted with the change of the width at half-height of XRD during annealing (Figure 2). Figure 3 shows the distributions of Pt nanoparticle size for each annealing treatment. We found that the breadth of the distribution of the particle size was larger with increasing annealing temperature, and not only the particle size. It can be assumed that an aggregate is formed between particles during annealing and growth of the aggregate by rearrangement. The growth attracts distributions in which larger particles increase with the formation of aggregates of small particles and decrease the fraction of the small particles.

Results of CV measurement, LSV measurement, Koutecky–Levich plots, and all values of each measurement are shown in Figure. 4. (a) Electrochemical surface area (ECSA), (b) specific activity obtained from Koutecky–Levich plots, and mass activity for

these catalysts under each annealing condition are shown in Figure 5. The mass activity decreased with increasing annealing temperature, which indicates that aggregate was formed between Pt nanoparticles and the fraction for the interior region increased. On the other hand, the specific activity increased. These results mean that ORR activity is closely related to structural changes in the subsurface region on the annealing treatment.

It was reported by Hammer and Nørskov[1] and Zhang et al.[13] that the Pt–Pt interatomic distance in the subsurface shows a volcano plot with specific activity in the theoretical calculations. Furthermore, the correlation between the Pt–Pt interatomic distance and the specific activity was studied by XAFS[1,2,4,14], XRD[15,16], and PDF analysis[7,17]. In this study, we also evaluated the correlation between the Pt–Pt interatomic distance and the specific activity at each particle size by XAFS and PDF analysis.

In order to evaluate the Pt–Pt interatomic distance of the Pt/C catalyst before and after annealing, we performed XAFS measurements and PDF analysis for the samples. Figure 6 shows (a) Pt L_{III}-edge XANES spectra and (b) Fourier transform of k^3–weighted Pt L_{III}-edge EXAFS oscillations. The peak intensity in XANES spectra decreased with increasing particle size, which is consistent with the previous XAFS work[3] and the results of our TEM measurement. Furthermore, from the fitting of the Fourier transform of k^3–weighted Pt L_{III}-edge XAFS oscillations in Figure 6(b) (Figure 7 shows the detailed fitting process), the Pt-Pt interatomic distances and coordination numbers (CN) of Pt were obtained. These results are summarized in Table 2. As can be seen in these results, both Pt–Pt interatomic distance and CN increase with increasing the average particle size because the CN of a large nanoparticle is larger than that of a smaller one. This means that the fraction of the interior Pt atoms toward the subsurface atom increased with

increasing Pt nanoparticle size. The results of EXAFS analysis are consistent with the XANES results. Figure 8 shows correlations between the closest Pt–Pt interatomic distances based on EXAFS analysis and specific activity. The result showed a positive correlation. However, we reported in a previous study that the Pt–Pt interatomic distance of the catalyst, which is the Pd core–Pt shell structure and does not include the Pt–Pt bond in the interior structure, shows a negative correlation with specific activity.[3] Such difference is caused by two factors, one is having many Pt–Pt bonds in the interior structure, and the other is a change in the fraction of the interior structure in the whole structure. That is, specific activity is correlated with the subsurface structure, which is the reaction field of ORR. Therefore, in the case of the increasing fraction of interior atoms, it is difficult to obtain the subsurface information on the basis of EXAFS. This is a reason for the difference between the previous work and this work.

The Pt–Pt interatomic distance depends on the particle size. We calculated the fraction of the subsurface for each particle size as shown in Figure 9(a), which increased similarly to the quadratic function with increasing distance. The short-range peaks provide little information of the subsurface, therefore, it can be used to evaluate the interior structure like a bulk structure, which means that the first PDF peak does not entirely correlate to nearby atoms only inside the NPs. On the other hand, medium– and long–range peaks provide more information of the subsurface and can more specifically be used to evaluate the subsurface structure compared with the short-range peak. Thus, we could analyze the structure in detail from the interior structure like the bulk structure to the subsurface structure by the PDF. The fitting regions for the subsurface at each particle model were decided from Figure 9(a) and shown in Figure 9(b).

Figure 10 shows the results of the PDF for each particle size as indicated by dashed

lines. The tendency of increasing intensity of $G(r)$ and the confirmation of the peak in the long-range peak were observed in the results. The increasing of $G(r)$ was caused by the increasing crystal face and coordination number, while the change in the long-range peak was caused by the increasing particle size. For a more accurate discussion of the change of the Pt–Pt interatomic distances in each region (interior and subsurface), a change in the Pt–Pt interatomic distances was calculated by PDF pattern fitting using the program PDFgui[12]. PDFgui uses a model, which is the minimum unit that can reproduce a unit cell, but it is not a complex model like the 3D nanoparticle model structure. The subsurface information of the catalyst evaluated using the 3D complex model fitting of the PDF, like the reverse Monte Carlo method, is an arbitrary evaluation. Therefore, we tried to obtain the subsurface information using a simple model analysis.

Bonds of the interior region are defined by a distance from 1 to 3 Å of $G(r)$ in all particle sizes as shown in Figure 10 by open circles. Moreover, bonds including the subsurface region are defined by distances from 6.53 to 11.65 Å, 11.83 to 19.78 Å, 13.63 to 22.53 Å, 13.63 to 22.53 Å and 14.67 to 24.12 Å in particle sizes of 2.9, 4.2, 4.7, 4.7 and 4.9 nm, respectively, by open squares. The subsurface regions were defined by the correlation between the average particle size and the fraction of the subsurface structure information obtained from the simulation as shown in Figure 9. Although we may be able to reproduce a refinement model to obtain the subsurface bonds, the subsurface parameters obtained by this experimental analysis are sufficient for the discussion of the change in the Pt–Pt interatomic distances.

The correlations between the closest Pt–Pt interatomic distance and specific activities are shown in Figure 11(a). If pattern fitting was performed using a peak in the interior region, the closest Pt–Pt interatomic distances presented values similar to those

of the bulk Pt, which is consistent with the results of XAFS in Figure 8. In contrast, the closest Pt–Pt interatomic distances of the subsurface region were smaller than those of the bulk Pt, which show stronger negative correlation on specific activity than interior region because peaks in the subsurface region include more subsurface structure information than those in the interior region. The schematic of the analysis in this study is shown in Figure 11(b). The subsurface structure information of nanoparticles was markedly obtained by PDF using only a medium to long-range distance. In other words, the PDF analysis is useful for extracting subsurface structure information.

2.4. Conclusion

In this study, annealed Pt/C catalysts were characterized. From the TEM observations, the increase in the average particle size is observed in each annealing treatment, which is consistent with the previous works[18,19]. Moreover, XAFS and PDF using the interior region were conducted to evaluate the change in the Pt–Pt interatomic distance in the subsurface. These showed no correlations with the specific activity and were close to the bulk Pt value. To compare the catalyst with different particle sizes, the structure information emphasized in the subsurface regions was obtained by PDF. We found a negative correlation between the Pt–Pt interatomic distances in the subsurface regions, which were obtained from PDF over the closest Pt–Pt interatomic distance, and specific activity, which is consistent with previous works using a model structure catalyst such as a core-shell and a Pt-skin structure. The method in this study can be applied to the nanoparticle catalyst, which has Pt–Pt bonds in the interior, and the result is also reasonable. Therefore, it showed that the subsurface structure information can be easily

extracted from experimental data by the method in this study without a complex model.

The method in this study could lead to a further understanding of the factors controlling the specific activity of the oxygen reduction reaction and the degradation mechanism of a Pt/C catalyst.

Reference

1. Hammer, B.; Norskov, J. K. Theoretical Surface Science and Catalysis — Calculations and Concepts. *Adv. Catal*. **2000**, *45*, 71–129.
2. Kaito, T.; Tanaka, H.; Mitsumoto, H.; Sugawara, S.; Shinohara, K.; Ariga, H.; Uehara, H.; Takakusagi, S.; Asakura, K. In Situ X-Ray Absorption Fine Structure Analysis of PtCo, PtCu, and PtNi Alloy Electrocatalysts: The Correlation of Enhanced Oxygen Reduction Reaction Activity and Structure. *J. Phys. Chem. C* **2016**, *120*, 11519–11527.
3. Wang, X.; Orikasa, Y.; Takesue, Y.; Inoue, H.; Nakamura, M.; Minato, T.; Hoshi, N.; Uchimoto, Y. Quantitating the Lattice Strain Dependence of Monolayer Pt Shell Activity toward Oxygen Reduction. *J. Am. Chem. Soc*. **2013**, *135*, 5938–5941.
4. Leontyev, I. N.; Kuriganova, A. B.; Leontyev, N. G.; Hennet, L.; Rakhmatullin, A.; Smirnova, N. V.; Dmitriev, V. Size Dependence of the Lattice Parameters of Carbon Supported Platinum Nanoparticles: X-Ray Diffraction Analysis and Theoretical Considerations. *RSC Adv.* **2014**, *4*, 35959–35965.
5. Lei, Y.; Jelic, J.; Nitsche, L. C.; Meyer, R.; Miller, J. Effect of Particle Size and Adsorbates on the L3, L2 and L1 X-Ray Absorption Near Edge Structure of Supported Pt Nanoparticles. *Top. Catal.* **2011**, *54*, 334–348.
6. Loukrakpam, R.; Shan, S.; Petkov, V.; Yang, L.; Luo, J.; Zhong, C.-J. Atomic Ordering Enhanced Electrocatalytic Activity of Nanoalloys for Oxygen Reduction Reaction. *J. Phys. Chem. C* **2013**, *117*, 20715–20721.
7. Prasai, B.; Ren, Y.; Shan, S.; Zhao, Y.; Cronk, H.; Luo, J.; Zhong, C.-J.; Petkov, V. Synthesis-Atomic Structure-Properties Relationships in Metallic Nanoparticles by Total Scattering Experiments and 3D Computer Simulations: Case of Pt–Ru

Nanoalloy Catalysts. *Nanoscale* **2015**, *7*, 8122–8134.

8. Petkov, V.; Prasai, B.; Shastri, S.; Chen, T.-Y. 3D Atomic Arrangement at Functional Interfaces Inside Nanoparticles by Resonant High-Energy X-Ray Diffraction. *ACS Appl. Mater. Interfaces* **2015**, *7*, 23265–23277.
9. Kumara, L. S. R.; Sakata, O.; Kohara, S.; Yang, A.; Song, C.; Kusada, K.; Kobayashi, H.; Kitagawa, H. Origin of the Catalytic Activity of Face-Centered-Cubic Ruthenium Nanoparticles Determined from an Atomic-Scale Structure. *Phys. Chem. Chem. Phys*. **2016**, *18*, 30622–30629.
10. Wu, J.; Shan, S.; Luo, J.; Joseph, P.; Petkov, V.; Zhong, C. J. PdCu Nanoalloy Electrocatalysts in Oxygen Reduction Reaction: Role of Composition and Phase State in Catalytic Synergy. *ACS Appl. Mater. Interfaces* **2015**, *7*, 25906–25913.
11. Izumi, F.; Momma, K. Three-Dimensional Visualization in Powder Diffraction. *Solid State Phenom*. **2007**, *130*, 15–20.
12. Farrow, C. L.; Juhas, P.; Liu, J. W.; Bryndin, D.; Boin, E. S.; Bloch, J.; Proffen, T.; Billinge, S. J. L. PDFfit2 and PDFgui: Computer Programs for Studying Nanostructure in Crystals. *J. Phys. Condens. Matter* **2007**, *19,* 335219.
13. Zhang, J.; Vukmirovic, M. B.; Xu, Y.; Mavrikakis, M.; Adzic, R. R. Controlling the Catalytic Activity of Platinum-Monolayer Electrocatalysts for Oxygen Reduction with Different Substrates. *Angew. Chem., Int. Ed.* **2005**, *44*, 2132–2135.
14. Mukerjee, S.; Srinivasan, S.; Soriaga, M. P.; McBreen, J. Role of Structural and Electronic Properties of Pt and Pt Alloys on Electrocatalysis of Oxygen Reduction. *J. Electrochem. Soc.* **1995**, *142*, 1409-1422.
15. Antolini, E.; Salgado, J. R. C.; Giz, M. J.; Gonzalez, E. R. Effects of Geometric and Electronic Factors on ORR Activity of Carbon Supported Pt–Co Electrocatalysts in

PEM Fuel Cells. *Int. J. Hydrogen Energy* **2005**, *30*, 1213–1220.

16. Escudero-Escribano, M.; Malacrida, P.; Hansen, M. H.; Vej-Hansen, U. G.; Velazquez-Palenzuela, A.; Tripkovic, V.; Schiotz, J.; Rossmeisl, J.; Stephens, I. E. L.; Chorkendorff, I. Tuning the Activity of Pt Alloy Electrocatalysts by Means of the Lanthanide Contraction. *Science* **2016**, *352*, 73–76.
17. Zhao, Y.; Maswadeh, Y.; Shan, S.; Cronk, H.; Skeete, Z.; Prasai, B.; Luo, J.; Petkov, V.; Zhong, C.-J. Composition–Structure–Activity Correlation of Platinum–Ruthenium Nanoalloy Catalysts for Ethanol Oxidation Reaction. *J. Phys. Chem. C* **2017**, *121*, 17077–17087.
18. Wanjala, B. N.; Loukrakpam, R.; Luo, J.; Njoki, P. N.; Mott, D.; Zhong, C.-J.; Shao, M.; Protsailo, L.; Kawamura, T. Thermal Treatment of PtNiCo Electrocatalysts: Effects of Nanoscale Strain and Structure on the Activity and Stability for the Oxygen Reduction Reaction. *J. Phys. Chem. C* **2010**, *114*, 17580–17590.
19. Lin, R.; Zhao, T.; Shang, M.; Wang, J.; Tang, W.; Guterman, V. E.; Ma, J. Effect of Heat Treatment on the Activity and Stability of PtCo/C Catalyst and Application of in-Situ X-Ray Absorption near Edge Structure for Proton Exchange Membrane Fuel Cell. *J. Power Sources* **2015**, *293*, 274–282.

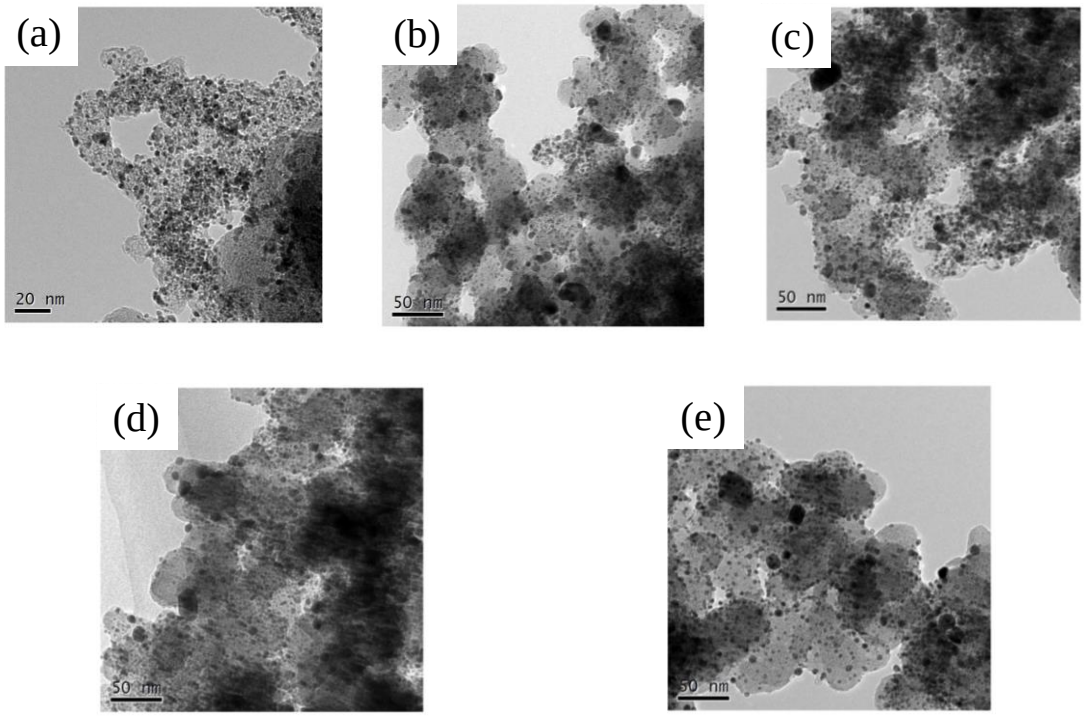

Figure 1. TEM images of Pt/C annealing samples. (a) is the Pt/C-untreated; (b) is the Pt/C-200°C; (c) is the Pt/C-400°C; (d) is the Pt/C-600°C; (e) is the Pt/C-800°C.

Table 1. Average particle sizes of untreated and annealed samples obtained from TEM measurements.

Annealing temperature	Average particle size / nm
untreated	2.9 ± 0.5
200ºC	4.2 ± 1.6
400ºC	4.7 ± 2.0
600ºC	4.7 ± 1.8
800ºC	4.9 ± 1.8

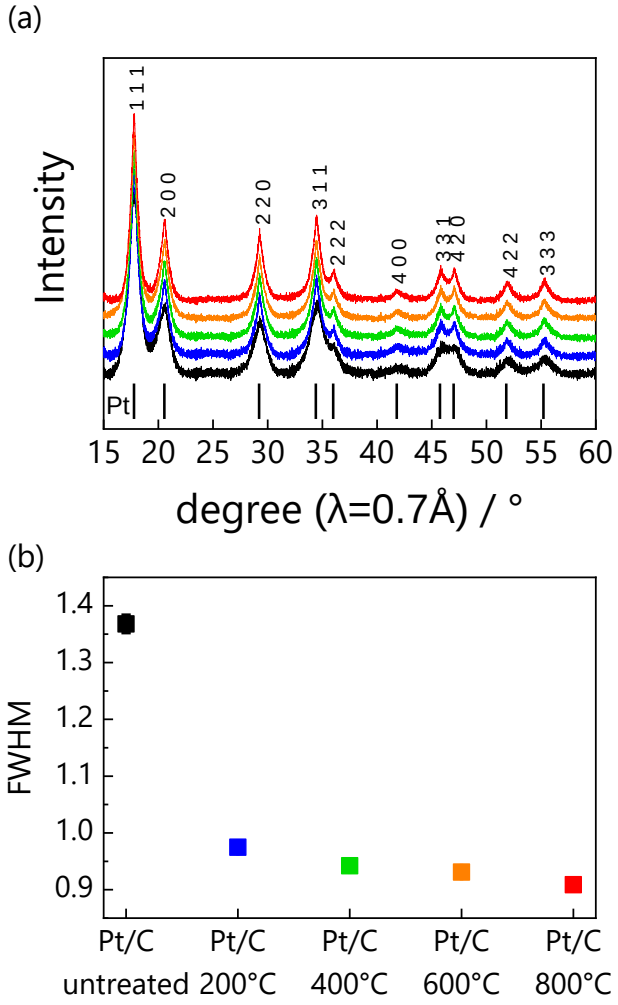

Figure 2. (a) XRD patterns of the untreated and annealed samples. Black, blue, green, orange, and red lines represent the untreated, 200, 400, 600, and 800ºC of the annealing temperature, respectively. (b) The peak width at half-height at 29.2º of untreated and annealed samples.

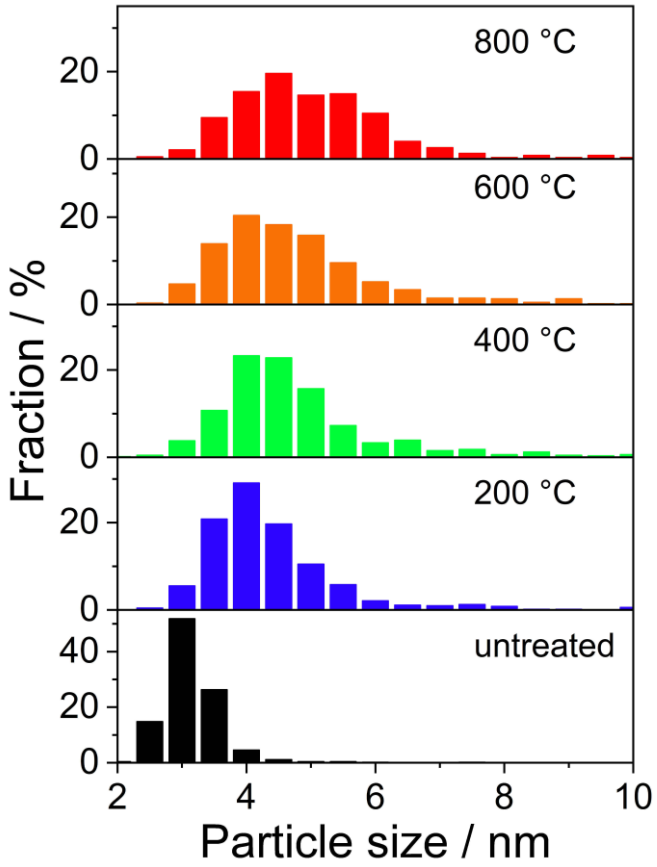

Figure 3. Particle size distributions of untreated and annealed samples. Black, blue, green, orange, and red sticks represent the untreated, 200, 400, 600, and 800ºC of the annealing temperature, respectively

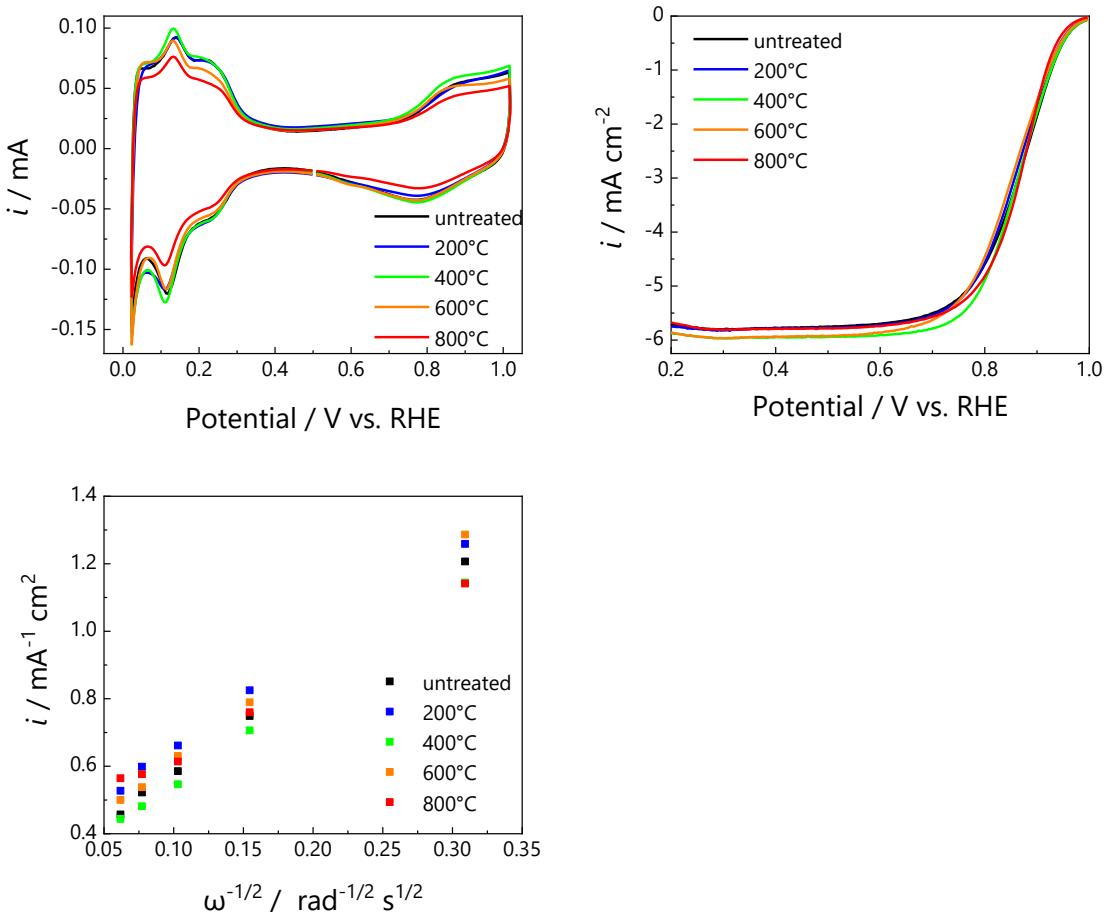

Figure 4. (a)Cyclic voltammograms of untreated and annealed Pt/C catalysts in 0.1 M $HClO_4$ at 25 ºC, (b)Polarization curves for oxygen reduction reaction and (c)Koutecky – Levich plots of untreated and annealed samples in O_2-saturated 0.1M $HClO_4$ at 25 ºC. The scan rate is 10 mV s^{-1}. Scan rate is 50 mVs^{-1}. The black line is the untreated sample; the red line is the Pt/C- 200ºC; the blue line is the Pt/C- 400ºC; the green line is the Pt/C- 600ºC; the pink line is the Pt/C- 800ºC.

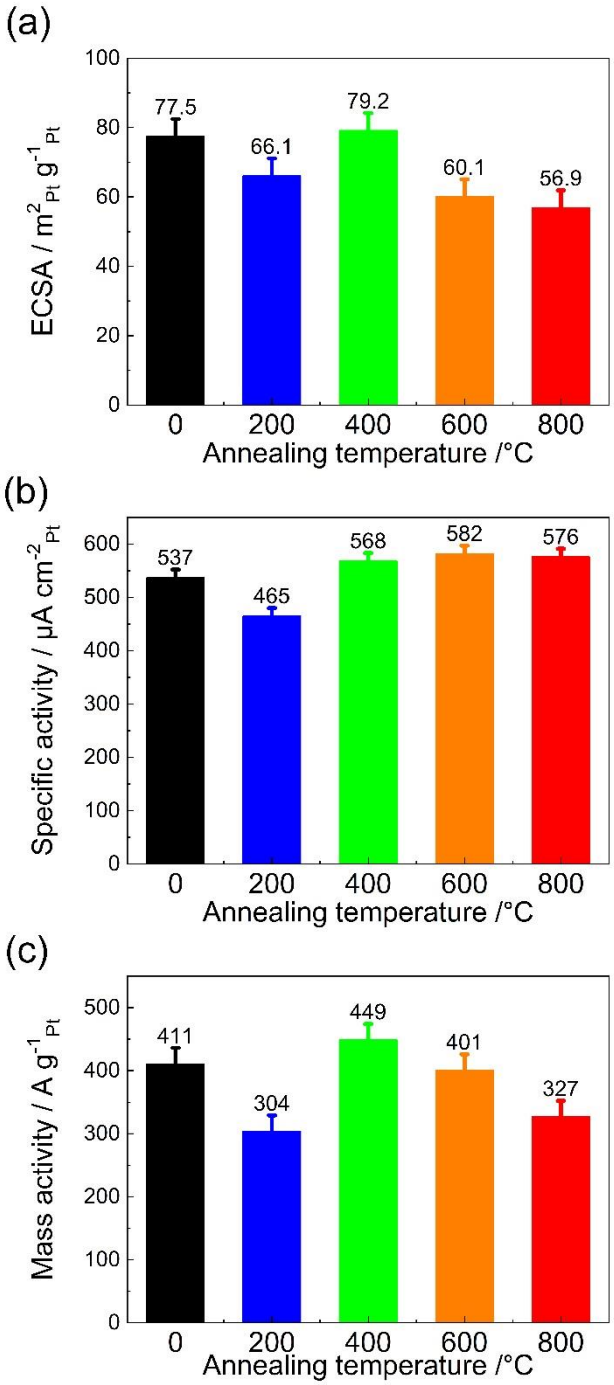

Figure 5. (a) ECSA, (b) specific activity and (c) Mass activity of untreated and annealed samples. Sticks show the average results for three times with the error bar.

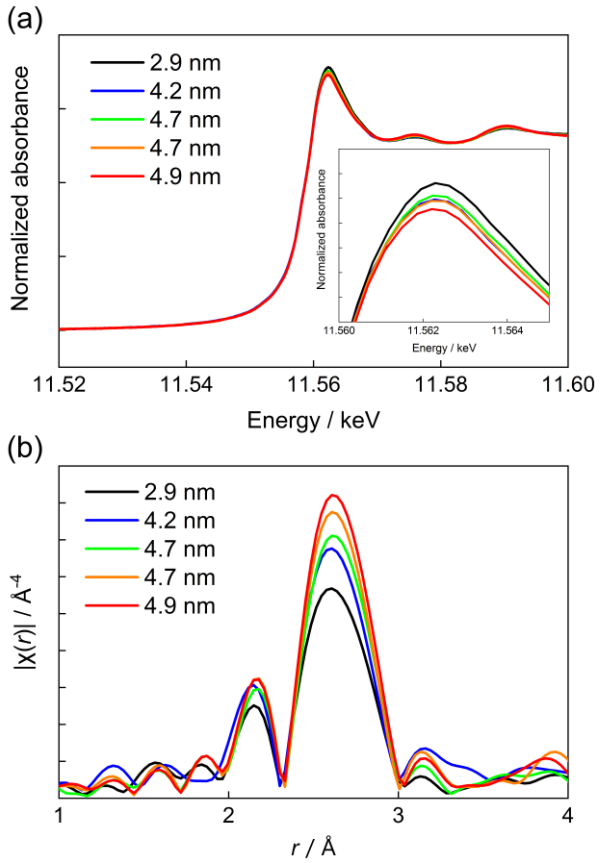

Figure 6. (a) Pt L_{III}-edge XANES spectra and (b) Fourier transform of k^3-weighted Pt L_{III} -edge EXAFS oscillations of untreated and annealed samples. Line colors correspond to stick ones in Figure 1.

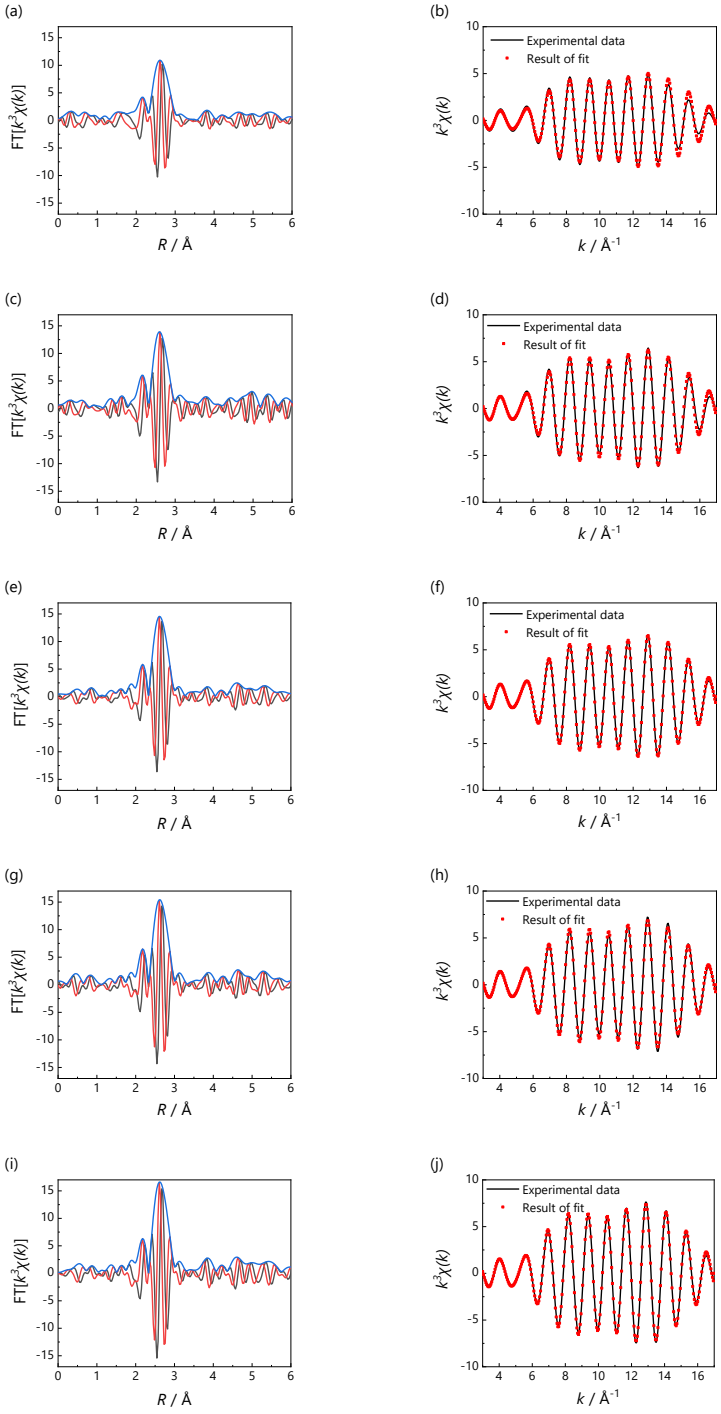

Figure 7. The result of curve fitting of Fourier transform of k^3-weighted Pt L_{III} -edge EXAFS oscillations of untreated and annealed samples.

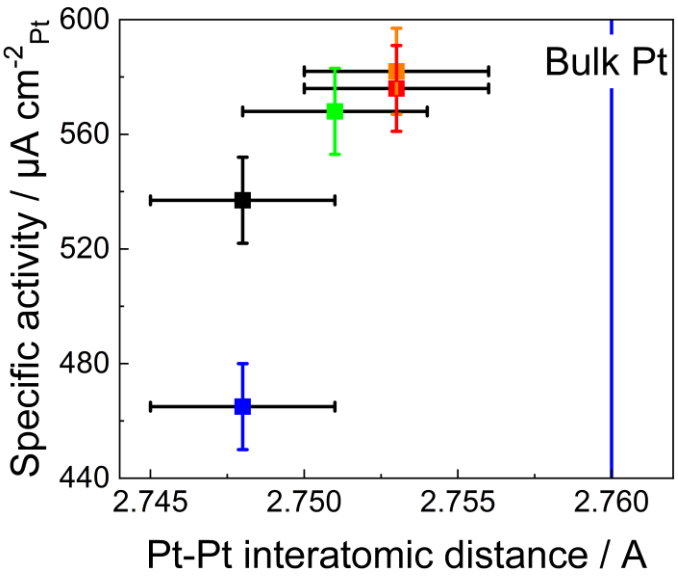

Figure 8. Correlation between Pt-Pt interatomic distances based on EXAFS analysis and specific activity. Plot colors correspond to stick ones in Figure 1.

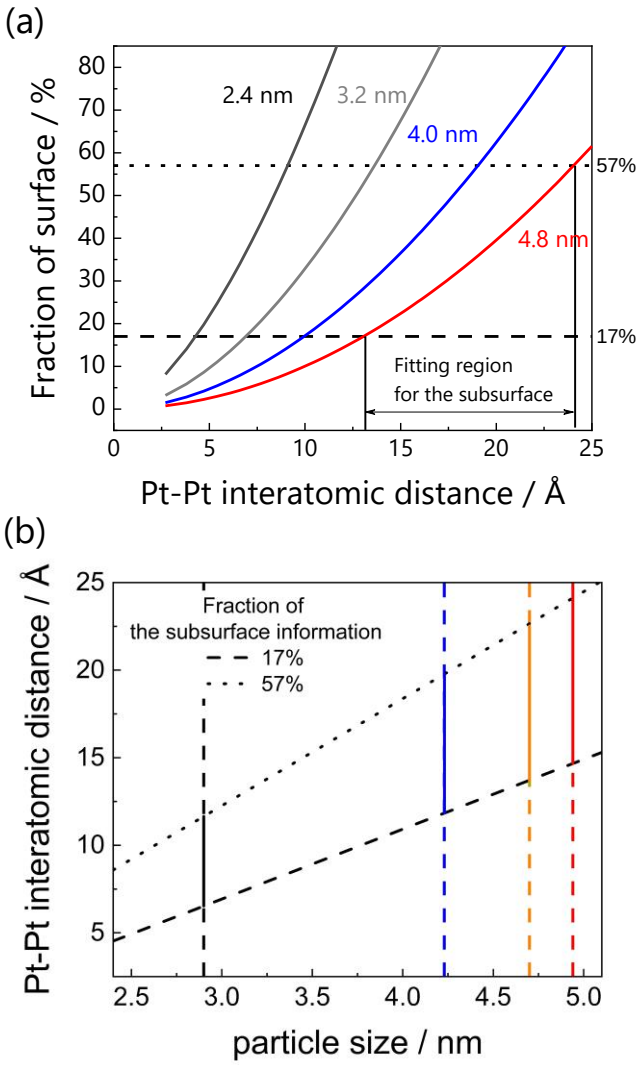

Figure 9. (a) Fraction of subsurface with interatomic distance for each particle size model and (b) fitting region for the subsurface at each particle model. Line colors correspond to stick ones in Figure 1.

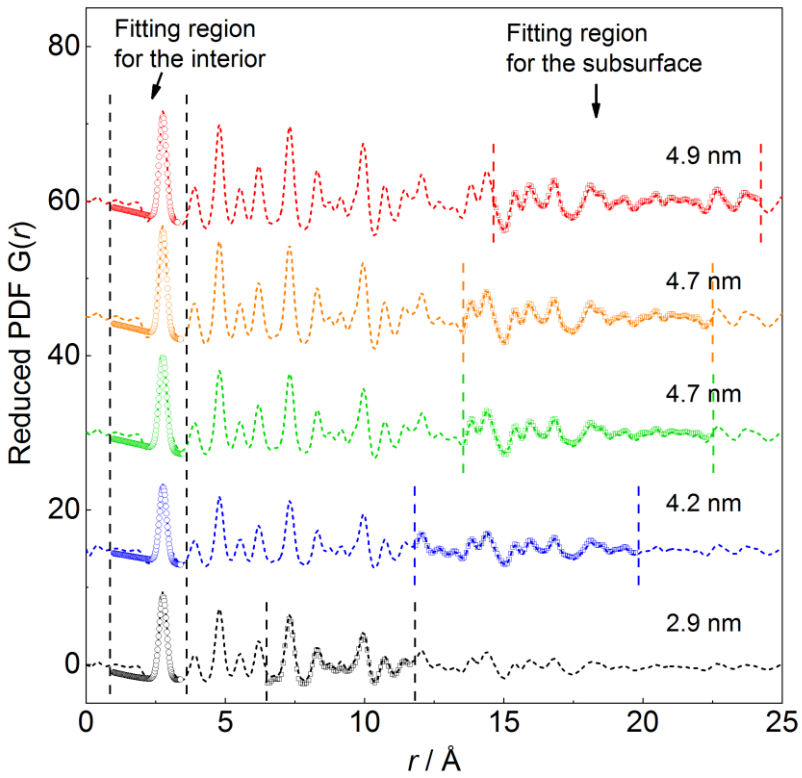

Figure 10. Summary of the reduced PDF $G(r)$ of untreated and annealed samples. Line colors correspond to stick ones in Figure 1.

Chapter 3. Synthesis of Sulfide Solid Electrolytes through the Liquid Phase: Optimization of the Preparation Conditions by Using Pair Distribution Function Analysis

3.1. Introduction

Lithium-ion rechargeable batteries (LIBs) have been expected for application to electric vehicles and to play the role of peak shaving and load shifting in a grid[1–5]. These power source and power storage demand to improve energy density, rate characteristics, safety, and lifetime[3–5]. However, current LIBs using organic liquid electrolytes have a safety issue, and the operating temperature is limited because of combustion hazards[6–11]. During past decades, all-solid-state batteries using inorganic solid electrolytes have been developed[12–21]. The inorganic solid electrolytes are nonleaking and nonvolatile[12,13] and have a wide potential window[14–18] and operating temperature[16,19], ensuring safety and durability. Moreover, the lithium-ion transfer number of inorganic solid electrolytes is 1, leading to high-power batteries[20,21].

Solid electrolytes are of several types such as oxide and sulfide solid electrolytes; especially, sulfide solid electrolytes show high ionic conductivities[16,22–25]. Furthermore, the sulfide solid electrolytes can easily contact the active material via mechanical pressing because of their lower elastic moduli[26,27] compared to oxide solid electrolytes[28,29].

Therefore, the commercial viability of the all-solid-state battery using sulfide solid electrolytes is expected as the first popularization stage[26,27].

Sulfide solid electrolytes are commonly synthesized by solid-phase methods, classified into the mechanical milling method and the method synthesizing via heating the evacuated quartz ampoule. The mechanical milling method is widely used in the synthesis of $Li_2S–P_2S_5$ sulfide glasses and glass ceramics[22,30] and lithium argyrodite Li_6PS_5X (X = Cl, Br, or I) [25,31]. Lithium superionic conductor-like crystalline compounds including $Li_{10}GeP_2S_{12}$ have been prepared via heating of the evacuated quartz ampoule[16,32,33]. These methods have disadvantages from the aspect of economical demand for large-scale synthesis and low energy because they cannot provide a large amount of the product and take a long time[16,22,25,30,31]. Therefore, developing a novel manufacturing method for large-scale synthesis is desired.

Since Liu et al. first reported liquid-phase synthesis of sulfide solid electrolytes[17], many researchers have attempted to synthesize them via liquid-phase synthesis to solve these current issues[17,34–42]. Several studies reported that the $Li_2S–P_2S_5$ solid electrolyte was synthesized via stirring Li_2S and P_2S_5 in polar organic solvents[17,34,38–41]. In all cases, the ionic conductivity of Li3PS4 prepared via liquid-phase synthesis was lower than that via solid-phase synthesis[17,34,38–41]. The relatively low ionic conductivity of Li_3PS_4 in the liquid phase is hypothesized to be due to two factors: the residual unreacted Li_2S and/or its relatively high crystallinity[39,43,44]. Shin et al. reported that the reason for the low ionic conductivity was the unreacted starting material, Li_2S[39]. However, the unreacted Li_2S was not confirmed using X-ray diffraction (XRD) and/or Raman spectroscopy in other studies[17,34–38,40–42]. Crystallinity is another factor for influencing the lithium ionic conductivity. Other researchers reported that the ionic conductivity decreased with

increasing crystallinity[43,44]. In the case of the liquid-phase synthesis, Li_3PS_4 is highly crystallized during the annealing process for removing the solvent, resulting in the decrease of the ionic conductivity[17,34,38–41].

These factors are influenced by synthesis and annealing conditions, which depend on the solvent properties such as solubility and boiling point. However, their contributions to the ionic conductivity have not been totally clarified because quantitative evaluation of the amount of the raw materials such as Li_2S and the degree of crystallinity is difficult by using conventional analytical methods such as Raman spectroscopy and XRD measurements. Pair distribution function (PDF) analysis is a method of structural analysis using total scattering data including not only Bragg but also diffuse scattering which can obtain both periodic and nonperiodic structural information. In addition, PDF analysis can quantitatively evaluate the crystallinity of the materials[43,44]. Therefore, PDF analysis is expected to be a powerful technique to clarify the reason of the relatively low ionic conductivity of Li_3PS_4 prepared by liquid-phase synthesis.

In this study, we prepared Li_3PS_4 electrolytes with various mixing times and annealing conditions via liquid-phase synthesis. High-energy XRD measurement coupled to PDF analysis is performed for the Li_3PS_4 electrolytes to evaluate quantitatively the amount of the raw material and crystallinity. This study is useful to optimize the liquid-phase synthesis process for sulfide solid electrolytes.

3.2. Experimental Section

3.2.1. Synthesis Methods of Li_3PS_4

Liquid-phase synthesis was used for the preparation of Li_3PS_4, which was reported

by Matsuda et al[37]. Li_2S (Mitsuwa Chemical Co., Ltd.) and P_2S_5 (Merck & Co., Inc.), at a molar ratio of 3:1, were shaken with a zirconia ball for up to 360 min at 1500 rpm in ethyl propionate (Sigma-Aldrich Co., LLC). The residual solvent was removed via centrifugation and reduced pressure drying at room temperature. Li_3PS_4 was synthesized by annealing of the precursor at 80, 100, 120, and 170°C. In this study, the shaking time varied from 5, 10, 30, 60, 120, 240, to 360 min. In addition, another Li_3PS_4 was prepared via the mechanical milling method for a reference material. Li_2S (Mitsuwa chemical Co., Ltd.), P_2S_5 (Merck & Co., Inc.), and zirconia balls were added to a zirconia pot and mixed via a planetary ball mill apparatus at 370 rpm for 20 h.

3.2.2. Raman Spectroscopy, Thermogravimetry, XRD Measurements, and Scanning Electron Microscopy Observation

Raman spectroscopy was conducted using a MultiRAM (Bruker Optics Co., Ltd.) equipped with a Nd-YAG laser (1064 nm) at room temperature. Raman spectra of the precursor were recorded between 3600 and 100 cm^{-1}. All samples were sealed in glass vessels in an argon-filled glovebox and measured without air exposure. Thermogravimetry (TG) measurement was performed for the precursor with a shaking time of 360 min. The precursor was loaded on an alumina pan in a glovebox. The alumina pan was transferred into the chamber of the TG instrument, and the chamber was purged with argon gas. The weight loss of the precursor was measured between 25 and 350°C. XRD measurement was conducted using an X-ray diffractometer (RINIT-Ultima III, Rigaku) with Cu Kα radiation. Samples were sealed in a holder in a glovebox to prevent air exposure. Scanning electron microscopy (SEM) observation was performed using a

field emission scanning electron microscope (SU8220, Hitachi High-Technologies) to observe the sample morphology.

3.2.3. High-Energy XRD Measurement Coupled to PDF Analysis

High-energy XRD measurements of all samples were carried out at the SPring-8 (Hyogo, Japan) beamline BL08W. The X-ray energy was 115 keV (0.108 Å), and the scattering X-ray was detected using a flat panel detector. The samples were sealed in a 2ϕ quartz capillary to prevent air exposure. Scattering data of each sample were corrected for background, absorption, multiple scattering, and inelastic scattering. The structure factor $S(Q)$ was obtained from the standardization of the corrected scattering data by the number of atoms and the scattering intensity from one atom. Moreover, the reduced PDF, $G(r)$, was calculated by the Fourier transform of $S(Q)$. $G(r)$ is defined by the equation $G(r) = 4\pi r\rho_0\{\rho(r)/\rho_0 - 1\}$, where r, ρ_0, and $\rho(r)$ are the real space distances, average atomic number density, and local atomic number density, respectively. Therefore, the information regarding the existing probability to the real distance is obtained using high-energy XRD measurement coupled to PDF analysis.

3.2.4. Ionic Conductivity

The ionic conductivity of the solid electrolytes was obtained by alternating current impedance measurements. The measurements were conducted at 25°C within a frequency range from 1 MHz to 1 Hz with an amplitude of 100 mV using an impedance analyzer (ModuLab XM ECS, Solartron Analytical). Pellets of samples, approximately 0.7 mm in thickness and 10.0 mm in diameter, were prepared via uniaxial pressing of a powdery sample at a pressure of 360 MPa in a cell. The pellets were held by two stainless-steel rods. These operations were conducted in a dry argon gas atmosphere.

3.3. Results and Discussion

Raman spectra for the precursors with different shaking times are shown in Figure 1. Li_3PS_4 of solid-phase synthesis and Li_2S as the raw material are listed for comparison. Peaks at 372, 422, and 407 cm^{-1} were observed in the sample after shaking for 5 min. These peaks were attributed to the vibration of the sublattice of Li_2S, the PS_4^{3-} anion, and the $P_2S_7^{4-}$ anion, respectively[45]. The peak intensities of Li_2S and the $P_2S_7^{4-}$ anion decreased with the increase of the shaking time and completely disappeared after 30 min. In contrast, the peak intensity of the PS_4^{3-} anion increased with the increase of the shaking time.

Figure 2 (a) shows the TG curve for the precursor prepared after a shaking time of 360 min. The TG curve showed a dramatic weight loss from 50 to 130°C. The dramatic weight loss in our synthesis may be related to ethyl propionate volatilization. Liang *et al.* reported a similar result using the tetrahydrofuran solvent during liquid-phase synthesis and mentioned that the weight loss was derived from solvent volatilization[17]. According to the TG data, we fixed the annealing temperature at 170 °C for 2 h. The XRD pattern of the precursor is shown in Figure 2 (b). The peaks from raw materials were not observed, and the observed Bragg peaks could not be assigned to any known structure. Similar results have been reported[17,36,37].

Figure 3 shows the XRD patterns of the precursor with different shaking times after annealing at 170 °C for 2 h. Strong diffraction peaks of Li_2S were observed at 27.0 and 31.3°, and weak diffraction peaks of β-Li_3PS_4 were also observed at 27.4, 29.1, and 29.8° for a sample prepared by shaking for 5 min. The peak intensity of Li_2S decreased

with the increase of shaking time and disappeared after 60 min, while the peak intensity for β-Li_3PS_4 increased with the increase of shaking time. These results indicate β-Li_3PS_4 formation, which is consistent with the result of Raman spectroscopy. XRD and Raman spectroscopy measurements showed the formation of β-Li_3PS_4; however, Li_2S can be detected within 30 min via Raman measurement and within 60 min via XRD measurement. In the previous report, Li_3PS_4 formed from the surface of Li_2S via the conversion reaction of Li_2S and dissolved species[41]. Raman spectroscopy is sensitive to the information of the surface structure, whereas XRD measurement can obtain information of the bulk structure. Therefore, Raman measurement may not detect the peak derived from Li_2S after Li_3PS_4 formation at the surface, which caused the different disappearance times between the XRD and Raman measurements.

Figure 4 shows the ionic conductivities for the sample prepared with different shaking times after annealing at 170 °C for 2 h. The lithium ionic conductivity logarithmically increased with the increase of the shaking time. It was observed that the particle size of the sample was a few micrometers from 5 to 60 min with shaking time and decreased to sub-micrometer from 60 to 360 min with shaking time by SEM (Figure 5). This particle size tendency cannot explain the tendency of the ionic conductivity change with shaking time. Although the XRD result shown in Figure 3 suggests that Li_2S disappeared after 60 min shaking time, the lithium ionic conductivity increased above 60 min shaking time. The reason for the low ionic conductivity at the short shaking time is the remaining Li_2S; our XRD results did not seem to agree well with the ionic conductivity result. In addition, the ionic conductivity of the liquid-phase synthesis was lower than that of the mechanical milling preparation. To clarify the reason, XRD measurement is not a sufficiently powerful tool because of the trace amount of the raw

material and the low crystallinity of products. We attempted to confirm the reason for the low ionic conductivity using PDF analysis.

Figure 6 shows the results of the PDF analysis for Li_3PS_4 prepared via liquid-phase synthesis with various shaking times and starting materials. After shaking for 360 min, the sample did not include starting materials and was nearly all Li_3PS_4. Li_3PS_4 had peaks at approximately 2.0, 3.3, and 4.1 Å and a broad peak around 7.0 Å corresponding to the P–S bond in the PS_4^{3-} tetrahedral anion, S–S correlation in the PS_4^{3-} tetrahedral anion, S–S correlation between the PS_4^{3-} tetrahedral anions, and P–P correlation between the PS_4^{3-} tetrahedral anions, respectively. Li_2S had characteristic peaks at approximately 2.5, 4.0, and 7.0 Å, as shown by the brown line in Figure 6. The peaks of Li_2S were observed in the samples prepared by shaking from 5 to 10 min. Then, the peak intensity of Li_2S decreased with the increase of the shaking time, whereas the peak intensity of Li_3PS_4 increased. It was reported in a previous study that differential PDF analysis can be used as a method for evaluating the ratio of glassy and crystalline phases[43]. We applied this method for estimating the ratio of the unreacted substance Li_2S and the product substance Li_3PS_4. We describe the details of the analytical method as following. We quantitatively estimated the ratio of the unreacted substance Li_2S and the product substance Li_3PS_4 by the follow equation.

$$G(r) = xG_{\mathrm{Li_2S}}(r) + (1-x)G_{\mathrm{Li_3PS_4}}(r)$$

Where the x, $G(r)$, $G_{\mathrm{Li_2S}}(r)$ and $G_{\mathrm{Li_3PS_4}}(r)$ are the ratio of the Li_2S, the reduced PDF of the sample, the reduced PDF of the Li_2S and the reduced PDF of the Li_3PS_4 prepared by the mechanical milling after annealing, respectively. First, we analyzed the sample prepared by shaking for 360 min after annealing. The blue line in Fig 7 shows the result of curve fitting by the reduced PDF, $G(r)$, of Li_2S and Li_3PS_4. The fitting did not match

the PDF, $G(r)$, of the sample prepared by shanking for 360 min. Next, we performed the curve fitting by only PDF, $G(r)$, of Li_3PS_4 by follow equation.

$$G(r) = yG_{Li_3PS_4}(r)$$

Where the y, $G(r)$ and $G_{Li_3PS_4}(r)$ are the arbitrary value, the reduced PDF of the sample and the reduced PDF of the Li_3PS_4 prepared by the mechanical milling after annealing, respectively. The result of curve fitting was shown red line in Fig 7. The curve fitting matched the PDF, $G(r)$, of the sample prepared by shanking for 360 min. Therefore, we conclude that the sample prepared by shaking for 360 min after annealing don't include the unreacted substance Li_2S. Other samples were performed the curve fitting by the reduced PDF, $G(r)$, of Li_2S and sample prepared by shaking for 360 min. Figure 8 (a) shows the detail of the curve fitting of the sample prepared by shaking for 10 min. The results of the curve fitting were shown in Figure 8 (b). The ratio of Li_2S to Li_3PS_4 estimated using the method is shown in Figure 9 (a). The ratio of Li_2S decreased, while the ratio of Li_3PS_4 increased with the increase of the shaking time. Intriguingly, it was shown using this analysis method that Li_2S, which was not detected in the Raman spectroscopy and XRD measurements, remained at several percentage points in the samples prepared by shaking up to 120 min. The sample prepared by shaking for 360 min did not have the unreacted material Li_2S. The correlation between the volume ratio of Li_2S and the ionic conductivity is shown in Figure 9 (b). The ionic conductivity increased with a decreasing amount of Li_2S with the increase of shaking time. However, Li_3PS_4 prepared via liquid-phase synthesis showed a lower ionic conductivity than that of the mechanical milling method despite not including Li_2S. These results clearly indicate that high-energy XRD coupled to PDF analysis is a powerful tool to detect trace amounts of compounds which cannot be detected by XRD.

High-energy XRD coupled to PDF analysis showed that the starting materials were completely removed in the sample obtained with 360 min shaking time. Therefore, we compared the structure of the Li_3PS_4 prepared by mechanical milling method and liquid phase synthesis after annealing. The XRD patterns of Li_3PS_4 prepared by annealing the precursor synthesized via liquid-phase synthesis and the mechanical milling method are shown in Figure 10. The XRD pattern of Li_3PS_4 prepared by liquid-phase synthesis was assigned to β-Li_3PS_4 (Figure 10 (a)). In contrast, the XRD pattern of Li_3PS_4 prepared by mechanical milling showed broad peaks that were difficult to assign (Figure 10 (b)). Therefore, samples prepared via liquid-phase and solid-phase synthesis were compared using high-energy XRD measurement coupled to PDF analysis, which can analyze both crystalline and amorphous structures to examine the local structure. The results of PDF analysis using the data are shown in Figure 11. Both of the samples prepared via mechanical milling and liquid phase synthesis after annealing showed the characteristic peaks of Li_3PS_4 at approximately 2, 3.3, 4.1, and broad peak around 7.0 Å, which were related to the P-S correlation, S-S correlation in the PS_4^{3-} anions, the S-S correlation between the PS_4^{3-} anions, and P-P correlation between the PS_4^{3-} anions, respectively. The previous study reported that increasing the peak intensity of the S-S correlation and P-P correlation between the PS_4^{3-} anions was in accordance with increasing crystallinity[43]. These peaks of the sample prepared via liquid-phase synthesis were higher than those via solid-phase synthesis. This result implies that the annealing sample prepared via liquid-phase synthesis had higher crystallinity than the sample prepared by the mechanical milling method. This is the reason for the lower ionic conductivity of the solid electrolyte prepared via liquid-phase synthesis than that of the solid electrolyte prepared by solid-phase synthesis because the ionic conductivity of Li_3PS_4 decreased with increasing

crystallinity.

Therefore, we annealed the precursor not including raw materials, which was confirmed by PDF analysis, at low temperature for the suppression of crystallization and optimized the annealing time. Figure 12 shows the lithium ionic conductivity of samples annealed at 80°C, 100°C, and 120°C for different time under Ar atmosphere. In the case of the sample annealed at 80°C, the lithium ionic conductivity increased with increase of the annealing time and reached a maximum value (0.109 mS cm^{-1}) at 12 h. Subsequently, it decreased with increase o the annealing time. In the case of the sample annealed at 100°C, the lithium ionic conductivity showed same tendency as the samples annealed at 80°C. In addition, it showed higher ionic conductivity (0.167 mS cm^{-1}) than that of 80°C. The ionic conductivity of the samples annealed at 120°C decreased with increase of the annealing time, which tendency was different from the others. The lithium ionic conductivity of all samples prepared via liquid phase synthesis was lower than ionic conductivity of the mechanical milling method. We focused on the samples annealed at 100°C and examined the relationship between the structure and the ionic conductivity. The XRD patterns of the samples annealed at 100°C in each annealing time are shown in Figure 13. The Bragg peaks at 27.4, 29.1, and 29.8º attributed to Li_3PS_4 (space group: *Pnma*) were observed from all samples. The Bragg peaks were obtained from all annealing samples and the peaks increased with annealing time and temperature. It is reported that Li_3PS_4 with amorphous structure shows higher lithium ionic conductivity than that of crystal structure[43,44]. This result can explain the reason why the lithium ionic conductivity was decreased by annealing over 12 h but cannot explain the reason why the lithium ionic conductivity increased with annealing time and reached a maximum value at 12 h.

Therefore, high-energy XRD measurement coupled to the PDF analysis was applied to compare the local structure of each samples for the revealing the reason. The result of PDF analysis of samples annealed at 100°C is shown in Figure 14. The samples prepared via liquid phase synthesis and mechanical milling method showed peaks of Li_3PS_4 around 2.0, 3.3, 4.1, and a broad peak around 7.0 Å. In addition, the peak corresponding to S-S correlation between the PS_4^{3-} tetrahedral anions was increased with increase of annealing time. It is reported that the peak intensity of f S-S correlation between PS_4^{3-} units was increased with increase of crystallinity and the crystallinity can be quantitatively evaluated by reproducing experimental PDF with amorphous Li_3PS_4 and crystalline Li_3PS_4 by follow equation[43]. We quantitively evaluated the crystallinity of the samples by using same technique.

$$G(r)_{\text{experimental data}} = (1\text{-}x)\ G(r)_{\text{amorphous}} + x\ G(r)_{\text{crystal}}$$

Where the $G(r)_{\text{experimental data}}$, $G(r)_{\text{amorphous}}$, $G(r)_{\text{crystal}}$ and x are the reduced PDF of the sample prepared by liquid phase synthesis after annealing at 100°C, reduced PDF of the Li_3PS_4 prepared by mechanical milling, reduced PDF of the Li_3PS_4 prepared by mechanical milling after annealing at 270°C and crystallinity, respectively. Figure 15(a) shows the annealing time dependence of the crystallinity. The crystallinity of the samples annealed at 100°C increased with increase of the annealing time. These results indicated that the crystallinity of Li_3PS_4 prepared via liquid phase synthesis increased as annealing time increases. The correlation between the crystallinity and the ionic conductivity of the samples annealed at 100°C is shown in Figure 15(b). The lithium ionic conductivity decreased in the annealing time over 12 h because the crystallinity of Li_3PS_4 increased. This result was consistent with the results of XRD measurement. Although, this result can explain the reason why the lithium ionic conductivity was decreased by annealing over

12 h, cannot explain why the lithium ionic conductivity increased by the annealing time of 12 h.

We compared the reduced PDF of samples prepared via liquid-phase synthesis and the mechanical milling method for revealing the reason of the increase of the ionic conductivity by the annealing time of 12 h. The results of PDF analysis of the sample annealed at 100 °C for 6 and 12 h and Li_3PS_4 prepared by the mechanical milling method are shown in Figure 16 (a). We focused on the shoulder peak observed at around 4.22 Å in the case of the sample annealed at 100 °C. Figure 16 (b) shows an enlarged view around 4.0 Å. The sample prepared by liquid-phase synthesis showed the peak of S–S correlation between PS_4^{3-} units at 3.97 Å and a shoulder peak at around 4.22 Å. The shoulder peak was not obtained from the PDF of Li_3PS_4 prepared by the mechanical milling method. As shown in Figure 14, the shoulder peak decreased with the increase of the annealing time. In the case of liquid-phase synthesis, Li_3PS_4 was formed by removing the solvent from the complex of Li_3PS_4 during the annealing process. In the result of TG–differential thermal analysis (DTA) measurement as shown in Figure 17 (a), the TG curve showed a significant weight loss between 80 and 120 °C and the DTA curve showed the two endothermic peaks at 85 and 121 °C. This result indicates that some intermediate states existed during the annealing process. The Raman spectra of the precursor and samples after annealing at 100 °C are shown in Figure 17 (b). The Raman spectrum of the precursor was recorded, and the peak around 2900 cm^{-1} was attributed to ethyl propionate[37]. In addition, Raman spectra of the samples after annealing at 100 °C were recorded; the peak was attributed to ethyl propionate, and the peak decreased with the increase of annealing time. This result indicates that the intermediate remained in the sample after annealing at 100 °C and the amount of the intermediate decreased with the

increase of annealing time. Considering these results, we considered that the shoulder peak was attributed to the intermediate states formed during the annealing process and that the intermediate remained in the samples in the short annealing time and decreased as the annealing time increased. Therefore, the lithium ionic conductivity was increased by decreasing intermediate with annealing time between 6 and 12 h. These results showed that the decrease of the intermediate and the increase of the crystallinity occurred simultaneously as annealing time increased, indicating that ionic conductivity shows a volcano behavior.

3.4. Conclusion

In this study, the factors determining lithium ionic conductivity in Li3PS4 prepared via liquid-phase synthesis were studied. High-energy XRD coupled to PDF analysis can detect trace amounts of the Li_2S starting material, which were difficult to detect using Raman spectroscopy and XRD measurements (Figure 18 (a)). It takes a longer sample shaking time than 360 min to completely remove the starting material. In addition, it was shown that the Li_3PS_4 prepared via liquid-phase synthesis after a long shaking time and annealed at 170 °C had higher crystallinity than that prepared via solid-phase synthesis.

Therefore, we optimized the annealing process in the liquid-phase synthesis of Li_3PS_4 for the suppression of crystallization. The sample annealed at 100 °C showed the highest ionic conductivity (0.167 mS cm^{-1}) at 12 h for the annealing time, whose ionic conductivity was higher than the ionic conductivity of the sample annealed at 170°C. However, the sample prepared by annealing at 100°C shows lower ionic conductivity than

that prepared by the mechanical milling method. The high-energy XRD measurement coupled to PDF analysis indicates that the residual amount of the intermediate in the sample decreased with the increase of the annealing time, while the crystallinity of Li_3PS_4 increased. This trade-off relationship between the crystallinity and the residual amount of the solvent in the sample determines the lithium ionic conductivity as shown in Figure 18 (b).

Reference

1. Dunn, B.; Kamath, H.; Tarascon, J.-M. Electrical Energy Storage for the Grid: A Battery of Choices. *Science* **2011**, *334*, 928–935.
2. Zubi, G.; Dufo-López, R.; Carvalho, M.; Pasaoglu, G. The Lithium-Ion Battery: State of the Art and Future Perspectives. *Renew. Sustain. Energy Rev.* **2018**, *89*, 292–308.
3. Wu, H.; Cui, Y. Designing Nanostructured Si Anodes for High Energy Lithium Ion Batteries. *Nano Today* **2012**, *7*, 414–429.
4. Islam, M. S.; Fisher, C. A. J. Lithium and Sodium Battery Cathode Materials: Computational Insights into Voltage, Diffusion and Nanostructural Properties. *Chem. Soc. Rev.* **2014**, *43*, 185–204.
5. Seh, Z. W.; Sun, Y.; Zhang, Q.; Cui, Y. Designing High-Energy Lithium–Sulfur Batteries. *Chem. Soc. Rev.* **2016**, *45*, 5605–5634.
6. Goodenough, J. B.; Kim, Y. Challenges for Rechargeable Li Batteries. *Chem. Mater.* **2010**, *22*, 587–603.
7. Goodenough, J. B.; Park, K. S. The Li-Ion Rechargeable Battery: A Perspective. *J. Am. Chem. Soc.* **2013**, *135*, 1167–1176.
8. Whittingham, M. S. Lithium Batteries and Cathode Materials. *Chem. Rev.* **2004**, *104*, 4271–4302.
9. Simon, P.; Gogotsi, Y. Materials for Electrochemical Capacitors. *Nat. Mater*. **2008**, *7*, 845–854.
10. Winter, M.; Brodd, R. J. What Are Batteries, Fuel Cells, and Supercapacitors? *Chem. Rev.* **2004**, *104*, 4245–4270.
11. Goodenough, J. B. Rechargeable Batteries: Challenges Old and New. *J. Solid State Electrochem.* **2012**, *16*, 2019–2029.

12. Tatsumisago, M.; Nagao, M.; Hayashi, A. Recent Development of Sulfide Solid Electrolytes and Interfacial Modification for All-Solid-State Rechargeable Lithium Batteries. *J. Asian Ceram. Soc.* **2013**, *1*, 17–25.
13. Hayashi, A.; Sakuda, A.; Tatsumisago, M. Development of Sulfide Solid Electrolytes and Interface Formation Processes for Bulk-Type All-Solid-State Li and Na Batteries. *Front. Energy Res.* **2016**, *4*, 25.
14. Inaguma, Y.; Liquan, C.; Itoh, M.; Nakamura, T.; Uchida, T.; Ikuta, H.; Wakihara, M. High Ionic Conductivity in Lithium Lanthanum Titanate. *Solid State Commun.* **1993**, *86*, 689–693.
15. Murugan, R.; Thangadurai, V.; Weppner, W. Fast Lithium Ion Conduction in Garnet-Type $Li_7La_3Zr_2O_{12}$. *Angew. Chem., Int. Ed.* **2007**, *46*, 7778–7781.
16. Kamaya, N.; Homma, K.; Yamakawa, Y.; Hirayama, M.; Kanno, R.; Yonemura, M.; Kamiyama, T.; Kato, Y.; Hama, S.; Kawamoto, K.; Mitsui, A. A Lithium Superionic Conductor. *Nat. Mater.* **2011**, *10*, 682–686.
17. Liu, Z.; Fu, W.; Payzant, E. A.; Yu, X.; Wu, Z.; Dudney, N. J.; Kiggans, J.; Hong, K.; Rondinone, A. J.; Liang, C. Anomalous High Ionic Conductivity of Nanoporous β-Li_3PS_4. *J. Am. Chem. Soc.* **2013**, *135*, 975–978.
18. Rangasamy, E.; Liu, Z.; Gobet, M.; Pilar, K.; Sahu, G.; Zhou, W.; Wu, H.; Greenbaum, S.; Liang, C. An Iodide-Based $Li_7P_2S_8I$ Superionic Conductor. *J. Am. Chem. Soc*. **2015**, *137*, 1384–1387.
19. Nagao, M.; Kitaura, H.; Hayashi, A.; Tatsumisago, M. High Rate Performance, Wide Temperature Operation and Long Cyclability of All-Solid-State Rechargeable Lithium Batteries Using Mo-S Chevrel-Phase Compound. *J. Electrochem. Soc.* **2013**, *160*, A819–A823.

20. Miura, A.; Rosero-Navarro, N. C.; Sakuda, A.; Tadanaga, K.; Phuc, N. H. H.; Matsuda, A.; Machida, N.; Hayashi, A.; Tatsumisago, M. Liquid-Phase Syntheses of Sulfide Electrolytes for All-Solid-State Lithium Battery. *Nat. Rev. Chem.* **2019**, *3*, 189–198.
21. Kato, Y.; Hori, S.; Saito, T.; Suzuki, K.; Hirayama, M.; Mitsui, A.; Yonemura, M.; Iba, H.; Kanno, R. High-Power All-Solid-State Batteries Using Sulfide Superionic Conductors. *Nat. Energy* **2016**, *1*, 16030.
22. Hayashi, A.; Hama, S.; Morimoto, H.; Tatsumisago, M.; Minami, T. Preparation of Li_2S-P_2S_5 Amorphous Solid Electrolytes by Mechanical Milling. *J. Am. Ceram. Soc.* **2004**, *84*, 477–479.
23. Minami, K.; Hayashi, A.; Tatsumisago, M. Preparation and Characterization of Superionic Conducting $Li_7P_3S_{11}$ Crystal from Glassy Liquids. *J. Ceram. Soc. Japan* **2010**, *118*, 305–308.
24. Deiseroth, H.-J.; Kong, S.-T.; Eckert, H.; Vannahme, J.; Reiner, C.; Zaiß, T.; Schlosser, M. Li_6PS_5X: A Class of Crystalline Li-Rich Solids With an Unusually High Li^+ Mobility. *Angew. Chem., Int. Ed.* **2008**, *120*, 767–770.
25. Boulineau, S.; Courty, M.; Tarascon, J.-M.; Viallet, V. Mechanochemical Synthesis of Li-Argyrodite Li_6PS_5X (X=Cl, Br, I) as Sulfur-Based Solid Electrolytes for All Solid State Batteries Application. *Solid State Ionics* **2012**, *221*, 1–5.
26. Sakuda, A.; Hayashi, A.; Tatsumisago, M. Sulfide Solid Electrolyte with Favorable Mechanical Property for All-Solid-State Lithium Battery. *Sci. Rep.* **2013**, *3*, 2261.
27. Nam, Y. J.; Cho, S.-J.; Oh, D. Y.; Lim, J.-M.; Kim, S. Y.; Song, J. H.; Lee, Y.-G.; Lee, S.-Y.; Jung, Y. S. Bendable and Thin Sulfide Solid Electrolyte Film: A New Electrolyte Opportunity for Free-Standing and Stackable High-Energy All-Solid-

State Lithium-Ion Batteries. *Nano Lett.* **2015**, *15*, 3317–3323.

28. El-Shinawi, H.; Paterson, G. W.; MacLaren, D. A.; Cussen, E. J.; Corr, S. A. Low-Temperature Densification of Al-Doped $Li_7La_3Zr_2O_{12}$: A Reliable and Controllable Synthesis of Fast-Ion Conducting Garnets. *J. Mater. Chem. A* **2017**, *5*, 319–329.
29. Ohta, S.; Seki, J.; Yagi, Y.; Kihira, Y.; Tani, T.; Asaoka, T. Co-Sinterable Lithium Garnet-Type Oxide Electrolyte with Cathode for All-Solid-State Lithium Ion Battery. *J. Power Sources* **2014**, *265*, 40–44.
30. Muramatsu, H.; Hayashi, A.; Ohtomo, T.; Hama, S.; Tatsumisago, M. Structural Change of Li_2S–P_2S_5 Sulfide Solid Electrolytes in the Atmosphere. *Solid State Ionics* **2011**, *182*, 116–119.
31. Auvergniot, J.; Cassel, A.; Ledeuil, J.-B.; Viallet, V.; Seznec, V.; Dedryvère, R. Interface Stability of Argyrodite Li_6PS_5Cl toward $LiCoO_2$, $LiNi_{1/3}Co_{1/3}Mn_{1/3}O_2$, and $LiMn_2O_4$ in Bulk All-Solid-State Batteries. *Chem. Mater.* **2017**, *29*, 3883–3890.
32. Tachez, M.; Malugani, J.; Mercier, R.; Robert, G. Ionic Conductivity of and Phase Transition in Lithium Thiophosphate Li_3PS_4. *Solid State Ionics* **1984**, *14*, 181–185.
33. Murayama, M.; Kanno, R. Synthesis of New Lithium Ionic Conductor Thio-LISICON—Lithium Silicon Sulfides System. *J. Solid State Chem.* **2002**, *168*, 140–148.
34. Teragawa, S.; Aso, K.; Tadanaga, K.; Hayashi, A.; Tatsumisago, M. Liquid-Phase Synthesis of a Li_3PS_4 Solid Electrolyte Using N-Methylformamide for All-Solid-State Lithium Batteries. *J. Mater. Chem. A* **2014**, *2*, 5095.
35. Matuda, A.; Muto, H.; H.H. Phuc, N. Preparation of $L_{i3}PS_4$ Solid Electrolyte by Liquid-Phase Shaking Using Organic Solvents with Carbonyl Group as Complex Forming Medium. *J. Japan Soc. Powder Powder Metall.* **2016**, *63*, 976–980.

36. Phuc, N. H. H.; Morikawa, K.; Totani, M.; Muto, H.; Matsuda, A. Chemical Synthesis of Li_3PS_4 Precursor Suspension by Liquid-Phase Shaking. *Solid State Ionics* **2016**, *285*, 2–5.

37. Phuc, N. H. H.; Morikawa, K.; Mitsuhiro, T.; Muto, H.; Matsuda, A. Synthesis of Plate-like Li_3PS_4 Solid Electrolyte via Liquid-Phase Shaking for All-Solid-State Lithium Batteries. *Ionics*. **2017**, *23*, 2061–2067.

38. Lim, H.-D.; Yue, X.; Xing, X.; Petrova, V.; Gonzalez, M.; Liu, H.; Liu, P. Designing Solution Chemistries for the Low-Temperature Synthesis of Sulfide-Based Solid Electrolytes. *J. Mater. Chem. A* **2018**, *6*, 7370–7374.

39. Choi, S.; Lee, S.; Park, J.; Nichols, W. T.; Shin, D. Facile Synthesis of Li_2S-P_2S_5 Glass-Ceramics Electrolyte with Micron Range Particles for All-Solid-State Batteries via a Low-Temperature Solution Technique (LTST). *Appl. Surf. Sci.* **2018**, *444*, 10–14.

40. Wang, H.; Hood, Z. D.; Xia, Y.; Liang, C. Fabrication of Ultrathin Solid Electrolyte Membranes of β-Li_3PS_4 Nanoflakes by Evaporation-Induced Self-Assembly for All-Solid-State Batteries. *J. Mater. Chem. A* **2016**, *4*, 8091–8096.

41. Wang, Y.; Lu, D.; Bowden, M.; El Khoury, P. Z.; Han, K. S.; Deng, Z. D.; Xiao, J.; Zhang, J.-G.; Liu, J. Mechanism of Formation of $Li_7P_3S_{11}$ Solid Electrolytes through Liquid Phase Synthesis. *Chem. Mater.* **2018**, *30*, 990–997.

42. Suto, K.; Bonnick, P.; Nagai, E.; Niitani, K.; Arthur, T. S.; Muldoon, J. Microwave-Aided Synthesis of Lithium Thiophosphate Solid Electrolyte. *J. Mater. Chem. A* **2018**, *6*, 21261–21265.

43. Shiotani, S.; Ohara, K.; Tsukasaki, H.; Mori, S.; Kanno, R. Pair Distribution Function Analysis of Sulfide Glassy Electrolytes for All-Solid-State Batteries: Understanding

the Improvement of Ionic Conductivity under Annealing Condition. *Sci. Rep.* **2017**, *7*, 6972.

44. Tsukasaki, H.; Mori, S.; Shiotani, S.; Yamamura, H. Ionic Conductivity and Crystallization Process in the Li_2S–P_2S_5 Glass Electrolyte. *Solid State Ionics* **2018**, *317*, 122–126.
45. Ghidiu, M.; Ruhl, J.; Culver, S. P.; Zeier, W. G. Solution-Based Synthesis of Lithium Thiophosphate Superionic Conductors for Solid-State Batteries: A Chemistry Perspective. *J. Mater. Chem. A* **2019**, *7*, 17735–17753.

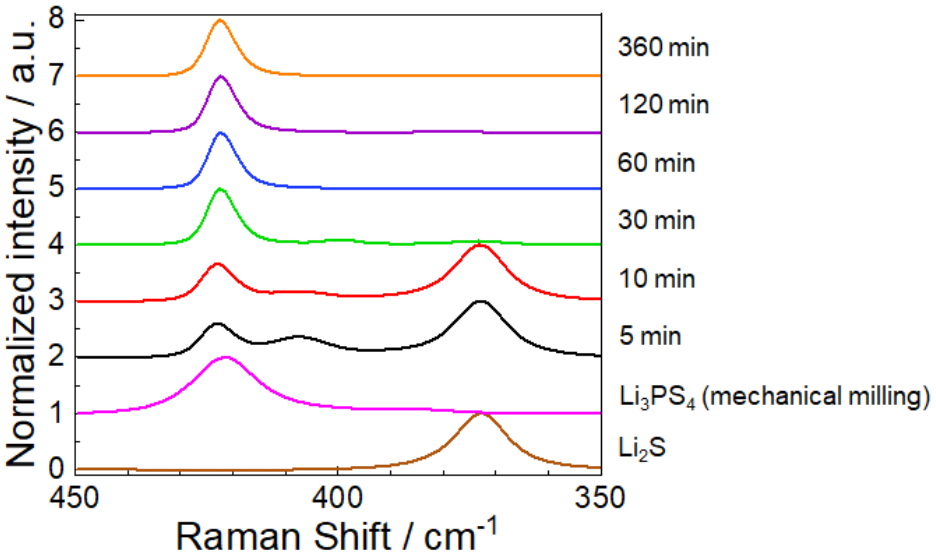

Figure 1. Raman spectra of raw materials and precursors at different shaking times.

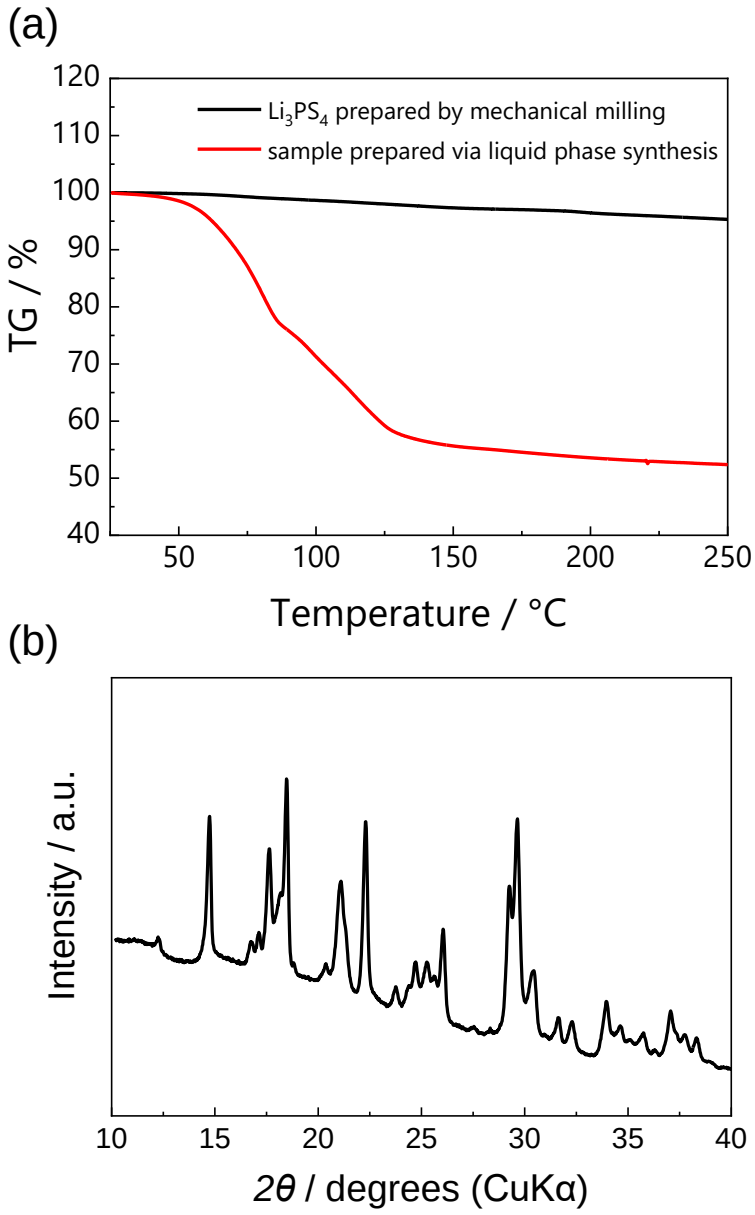

Figure 2. (a) TG curves of the Li_3PS_4 prepared by the mechanical milling method and precursor prepared by shaking for 360 min at 10ºC min^{-1} under an Ar atmosphere. (b) XRD pattern of the precursor prepared by shaking for 360 min.

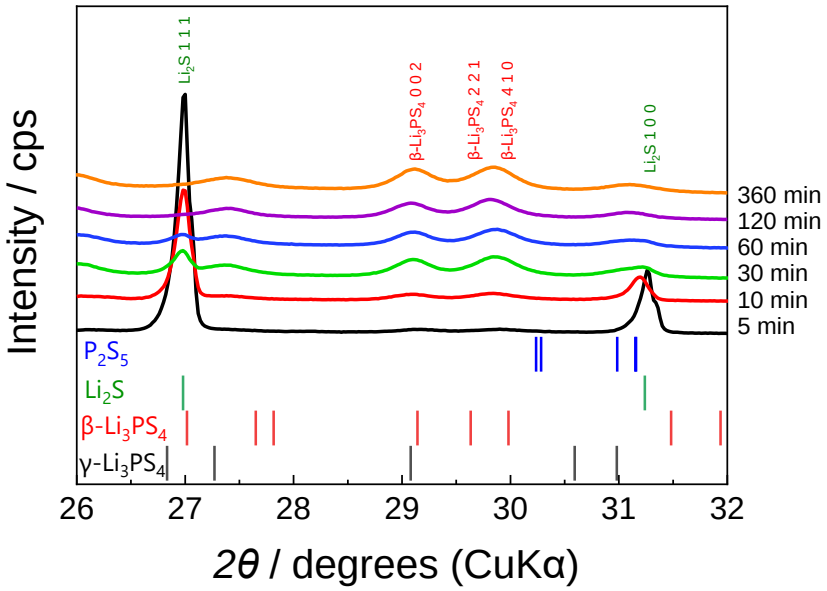

Figure. 3 XRD patterns of samples prepared at different shaking times after annealing at 170°C for 2 h.

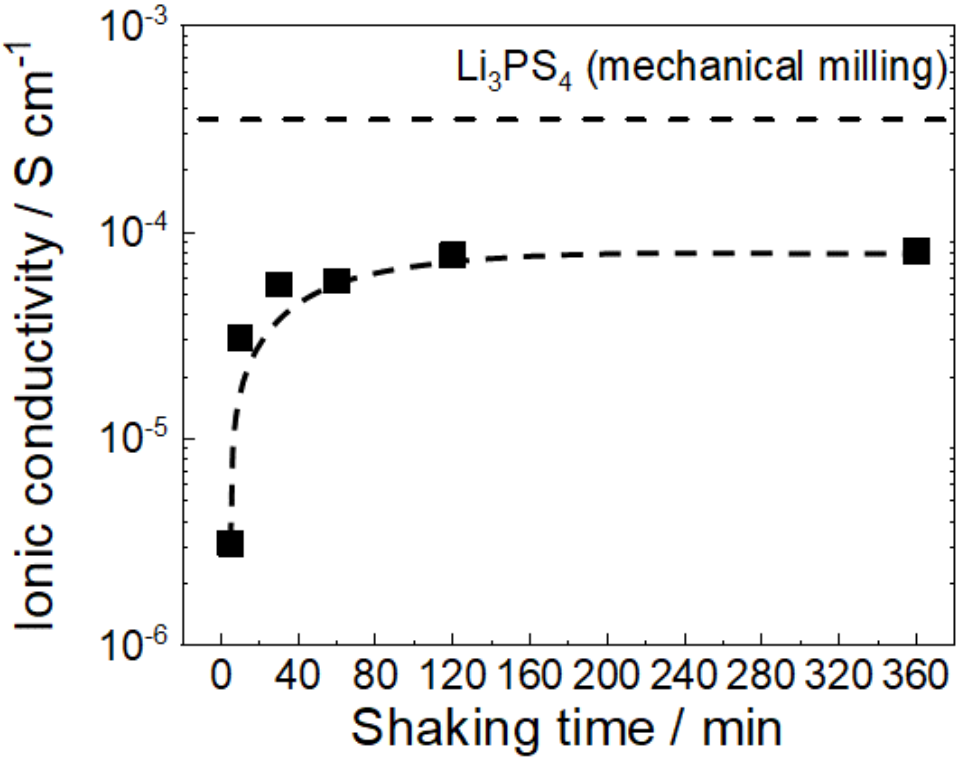

Figure 4. Correlation between the shaking time and the sample ionic conductivity after annealing at 170°C for 2 h at 25°C.

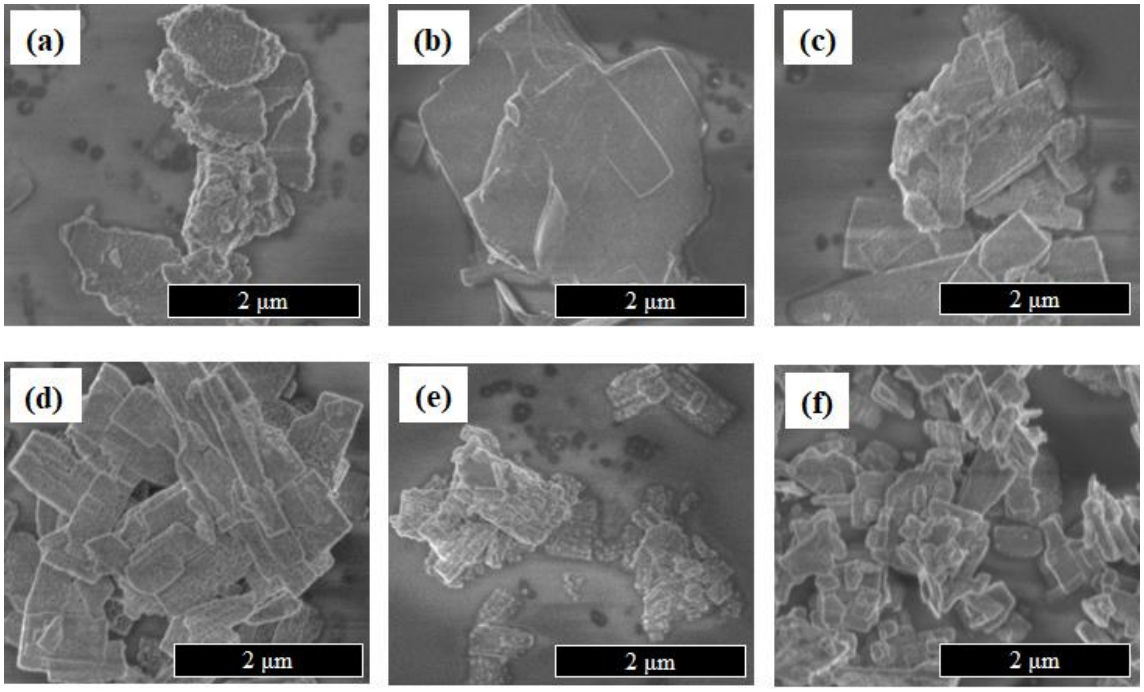

Figure 5. SEM image of the Li_3PS_4 prepared by shaking for (a) 5 min, (b) 10 min, (c) 30 min, (d) 60 min, (e) 120 min and (f) 360 min after annealing at 170 °C for 2 h.

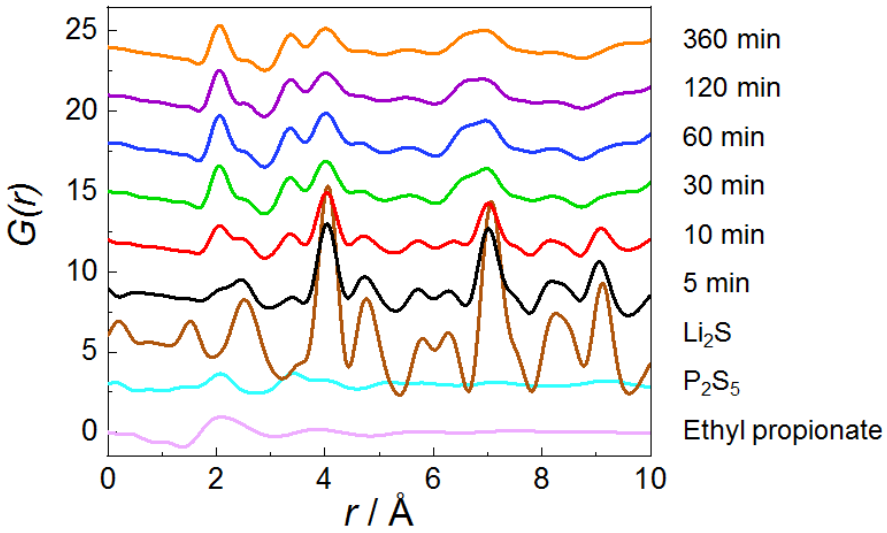

Figure 6. Reduced pair distribution function, $G(r)$, of the Li_3PS_4 prepared by heating precursors with different shaking times at 170°C for 2 h.

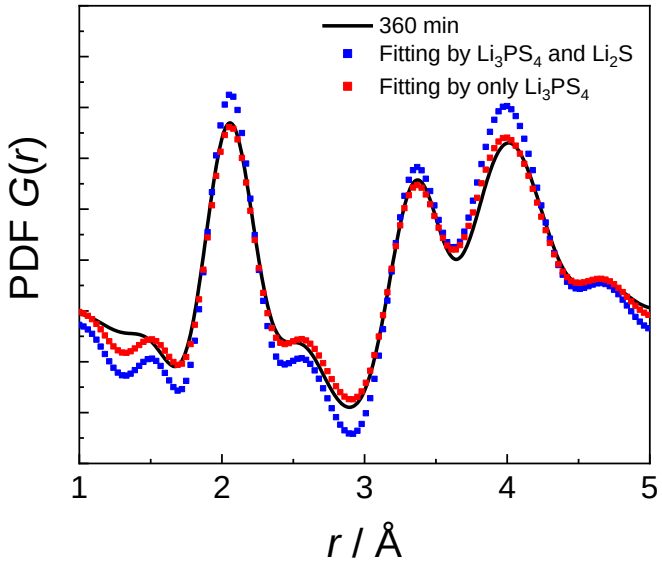

Figure 7. Curve fittings of reduce PDF of the samples prepared by shaking for 360 min. The blue plot is the result of fitting by Li_2S and Li_3PS_4 prepared by mechanical milling method after annealing. The red plot is the fitting by only Li_3PS_4 prepared by mechanical milling method after annealing.

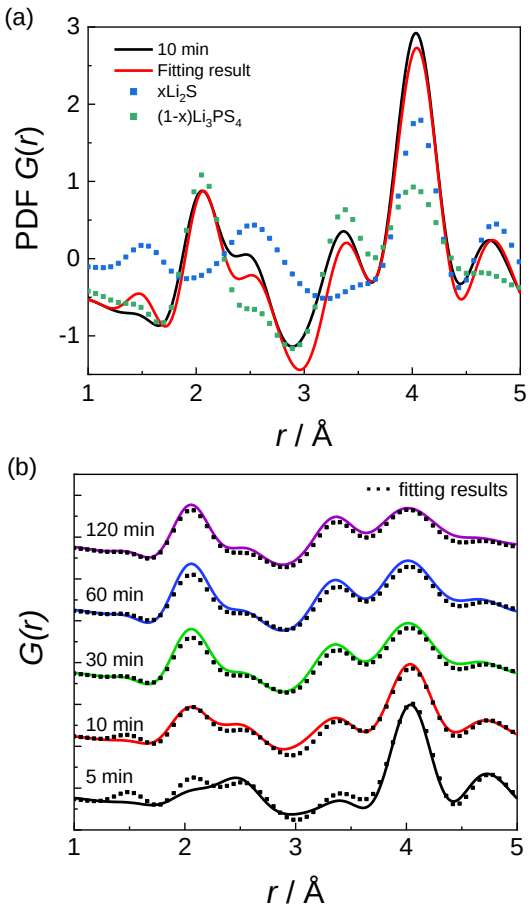

Figure 8. (a) Detail of curve fittings of reduce PDFs of the samples prepared by shaking for 10 min by the Li_2S and Li_3PS_4 prepared by shaking for 360 min after annealing. (b) Curve fittings of reduce PDFs of the samples prepared by liquid phase synthesis by the Li_2S and Li_3PS_4 prepared by shaking for 360 min after annealing.

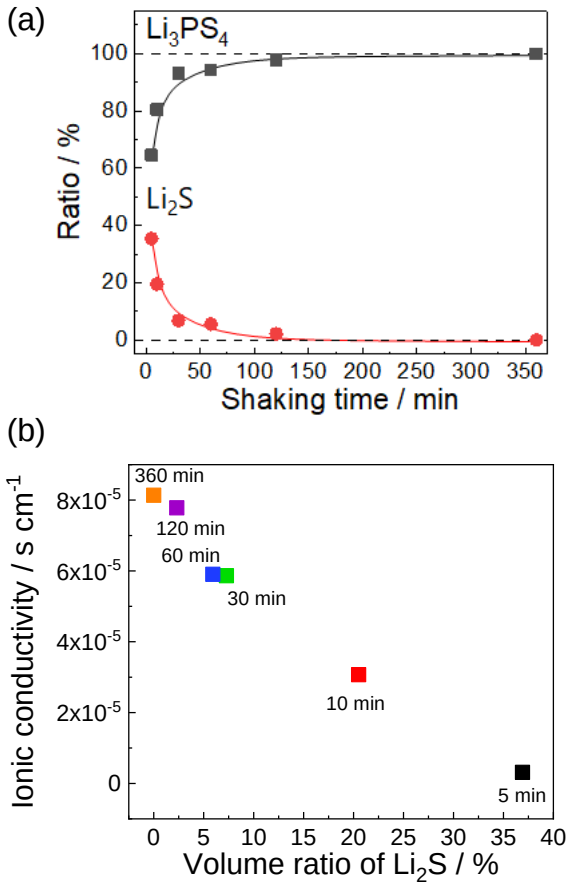

Figure 9. (a) Correlation of the ratio of Li_3PS_4 to Li_2S obtained from $G(r)$ in samples after annealing at 170°C for 2 h to the shaking time from 5 to 360 min. (b) Correlation between volume ratio of Li_2S and ionic conductivity at 25°C of Li_3PS_4 prepared using annealing precursors with different shaking times at 170°C for 2 h.

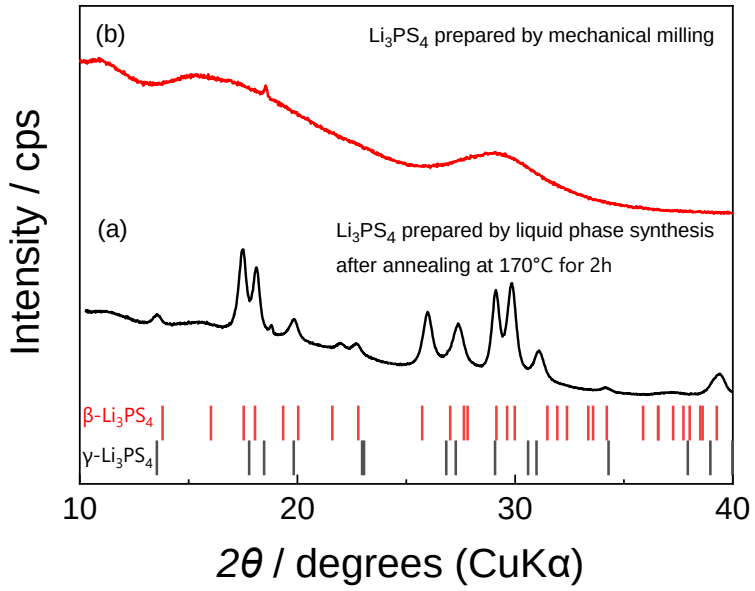

Figure 10. XRD patterns of Li_3PS_4 prepared via (a) liquid phase synthesis after annealing at 170°C for 2 h (black line) or (b) solid phase synthesis (red line).

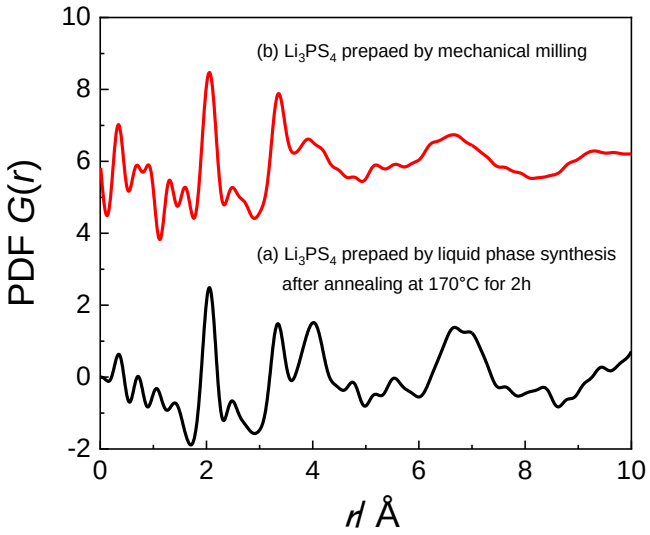

Figure 11. Reduced PDFs of the Li_3PS_4 prepared via (a) liquid phase synthesis after annealing at 170°C for 2 h (black line) or (b) solid phase synthesis (red line).

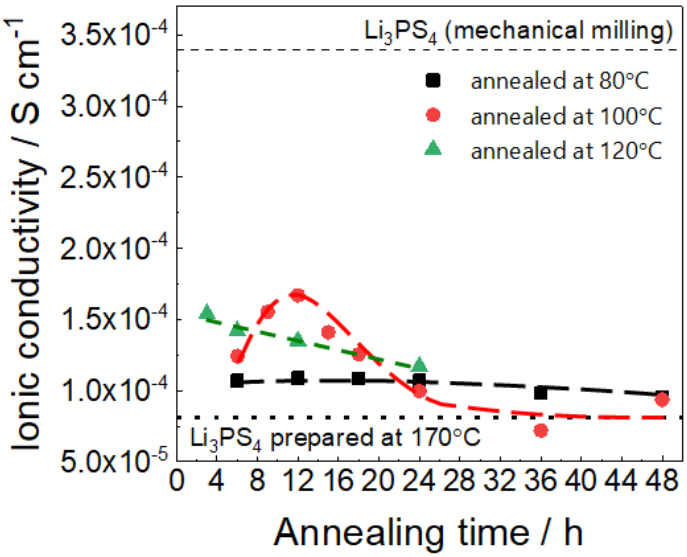

Figure 12. The lithium ionic conductivity of samples prepared by liquid phase synthesis after annealing at 80°C (black plots), 100°C (red plots) and 120°C (green plots) for each time.

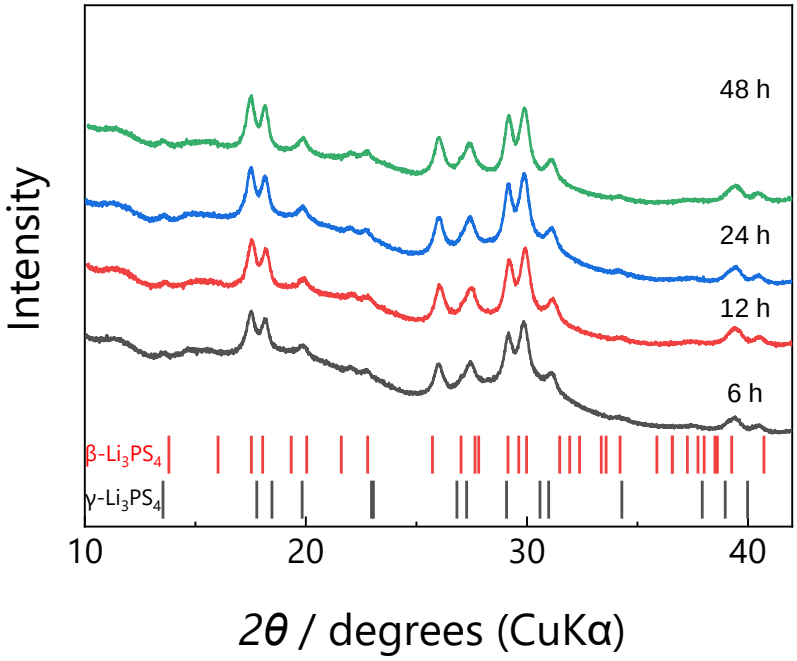

Figure 13. XRD patterns of samples annealed at 100°C for 6 h (black line), 12 h (red line), 24 h (blue line), 48 h (green line). Black bar is the reference material of γ-Li_3PS_4 and red bar is the reference material of β-Li_3PS_4.

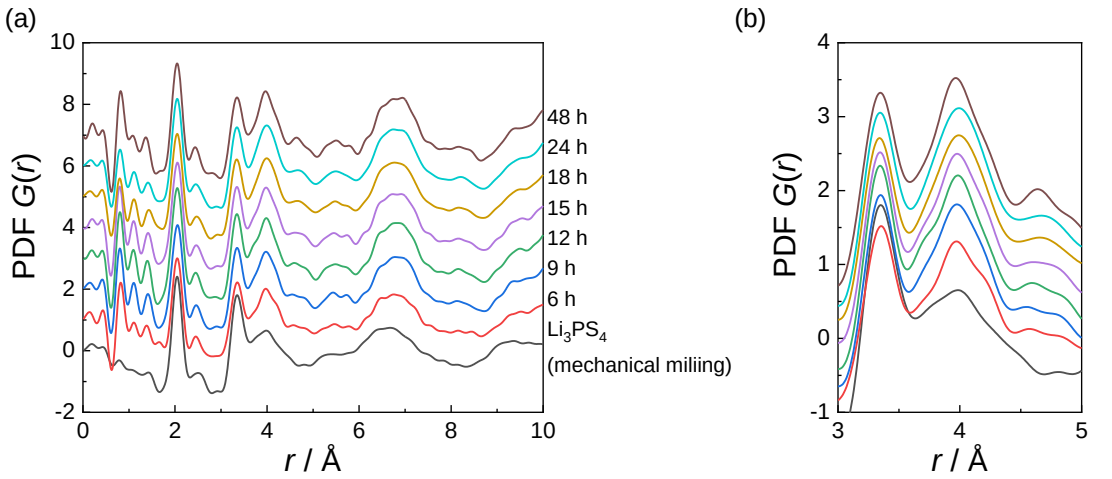

Figure 14. (a) The reduced PDF of the Li_3PS_4 prepared by mechanical milling method and the precursor and the samples annealed at 100°C for each time. (b) enlarge view of the reduced PDF from 3 to 5 Å.

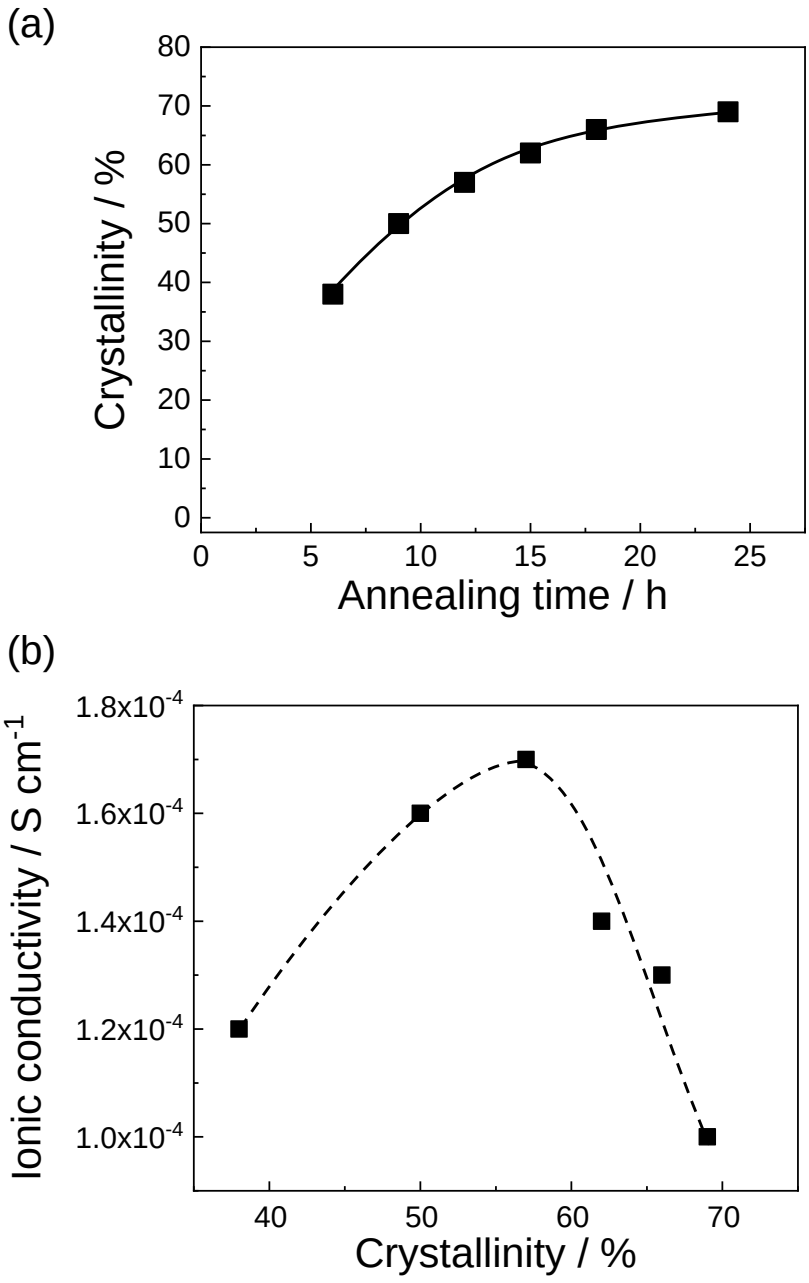

Figure 15. (a) The correlation between the annealing time and the crystallinity of the samples annealed at 100°C. (b) The correlation between the crystallinity and the lithium ionic conductivity of the samples annealed at 100°C.

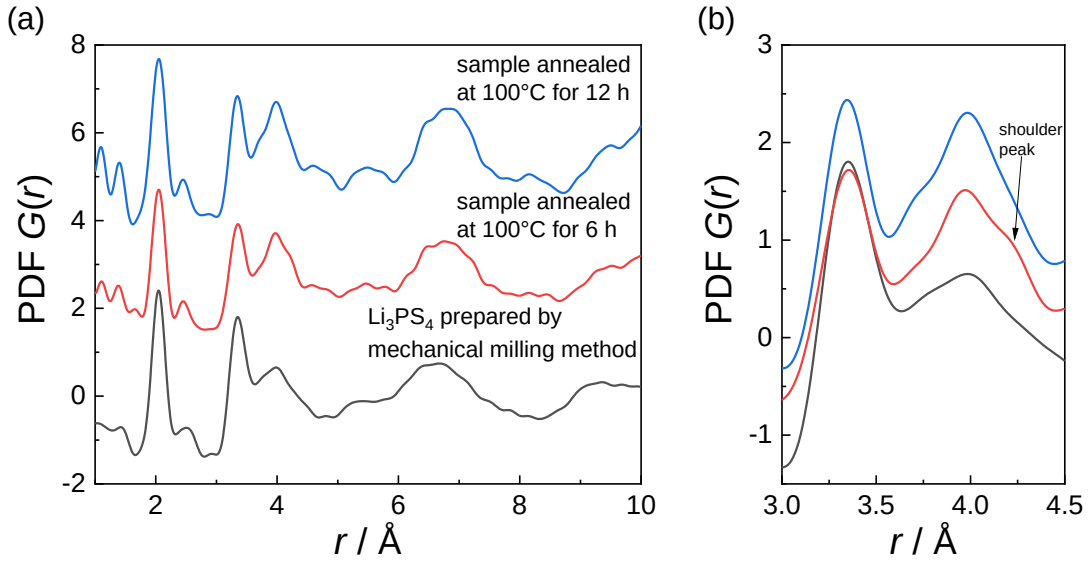

Figure 16. (a) Reduced PDF $G(r)$ of samples annealed 100°C for 6 h (red line) and 12 h (blue line) and Li_3PS_4 prepared by mechanical milling method (black line). (b) enlarge view of the reduced PDF from 3.0 to 5.0 Å.

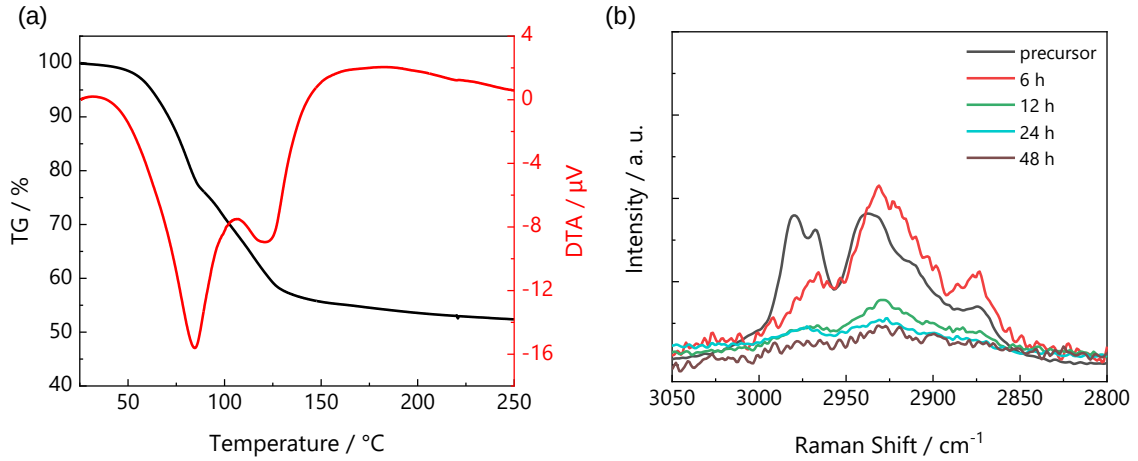

Figure 17. (a) TG-DTA curve of the precursor prepared by shaking for 360 min at 10ºC min^{-1} under an Ar atmosphere. (b) Raman spectra of the samples annealing at 100ºC with different annealing times.

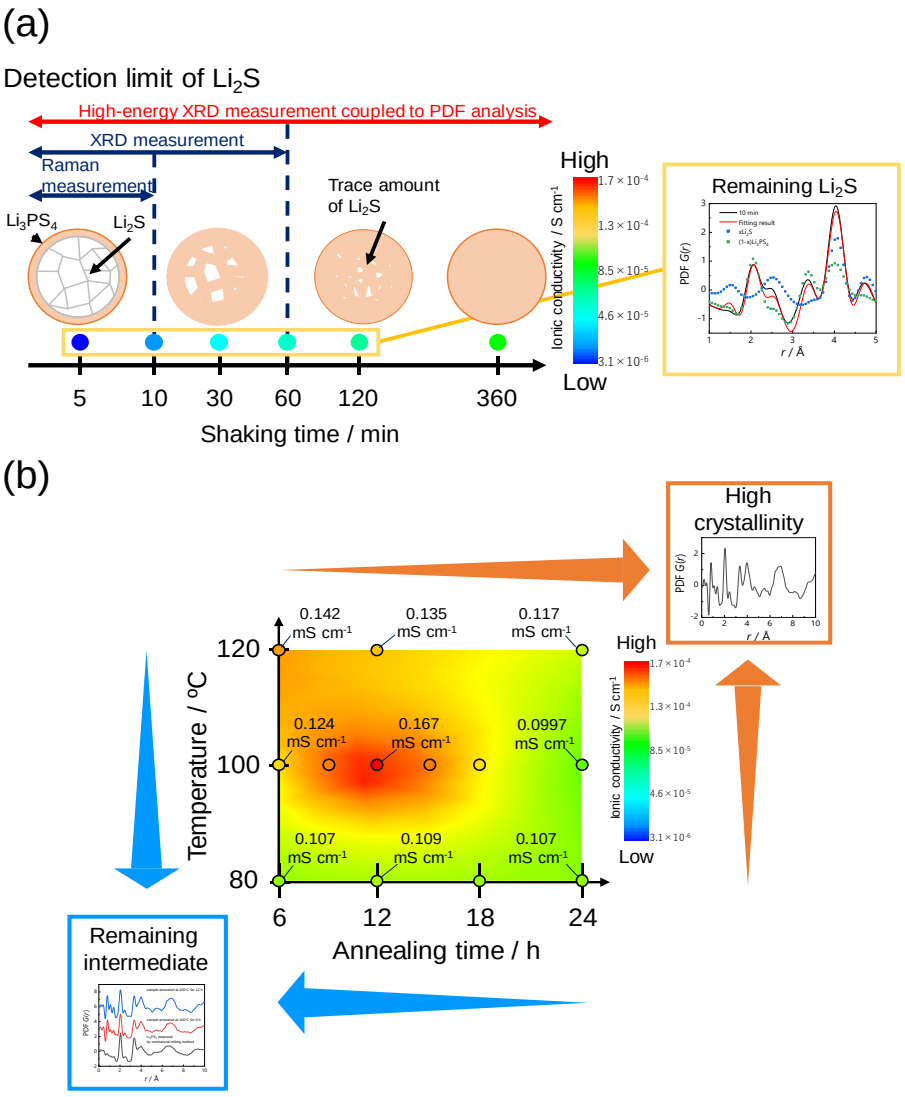

Figure 18. (a) Scheme of detection limits of Li_2S in the case of Raman and XRD measurements and high-energy XRD coupled to PDF analysis. (b) Scheme of the effect of annealing conditions on ionic conductivity of the Li_3PS_4 prepared by the liquid phase synthesis.

Chapter 4. Improvement of lithium ionic conductivity of Li_3PS_4 through suppression of crystallization using low-boiling-point solvent in liquid-phase synthesis

4.1. Introduction

Lithium ion batteries (LIBs) must improve in terms of energy density and safety in response to growing storage demands. All-solid-state batteries, which have solid-state components, are expected to be the most promising next-generation batteries in terms of the potential to be highly safe[1–5]. The key material in this battery system is a solid electrolyte. Among the various solid electrolytes, sulfide solid electrolytes have attracted much attention because of their high ionic conductivity[6–10] and low elastic module[11,12].

Several sulfide solid electrolytes have been developed, such as Li_2S-P_2S_5 sulfide glasses and glass-ceramics[6,13], argyrodite Li_6PS_5X (X = Cl, Br, I)[9,14], and LISICON-like crystalline compounds including $Li_{10}GeP_2S_{12}$[10,15,16]. However, conventional synthesis methods, such as mechanical milling, cannot meet industrial demands because large-scale synthesis is difficult and they are time-consuming[6,9,10,13,14]. Therefore, liquid-phase synthesis using organic solvents has been reported as an alternative[17–26]. Liquid-phase synthesis supplies a large amount of a sample in a shorter time compared to the conventional methods. However, the ionic conductivity of a solid electrolyte prepared

using the liquid-phase synthesis method is lower than that of one prepared using the conventional method, which is a critical problem[17,18,22–25]. Thus, most studies have focused on improving the ionic conductivity and determining the cause, and it was found that the relatively low ionic conductivity of solid electrolytes prepared through liquid-phase synthesis is the result of residual unreacted raw materials and the crystallinity[23,27,28].

In a previous paper, we reported the quantitative evaluation of these factors by using high-energy X-ray diffraction (XRD) coupled with pair distribution function (PDF) analysis[29]. It was revealed that the residual amount of the intermediate formed during the annealing process and the crystallinity of Li_3PS_4 affected the lithium ionic conductivity [29]. These factors depend on the annealing conditions, which are affected by solvent properties such as boiling point. Therefore, the solvent is also an important factor that affects the ionic conductivity of an electrolyte. It has been reported that several types of solvents have been used in the synthesis of sulfide solid electrolytes and this affected the ionic conductivity[17,18,22–25]. However, the influence of solvent properties on the ionic conductivity has not been clarified. For the selection of solvents for liquid-phase synthesis, it is necessary to determine the effects of their properties on the ionic conductivity.

In this study, we focused on the boiling point and used THF as the solvent for the liquid-phase synthesis of Li3PS4 because it has a lower boiling point (66°C) than ethyl propionate (99°C). In addition, we verified the effect of the boiling point on ionic conductivity and crystallinity by comparing the results obtained using THF with previously reported results from ethyl propionate.

4.2. Experimental Section

4.2.1. Preparation of Li_3PS_4 through liquid-phase synthesis

Li_2S (Sigma-Aldrich Co., LLC) and P_2S_5 (Sigma-Aldrich Co., LLC) in a 3:1 molar ratio and a zirconia ball with a 4.0 mm diameter were placed in a tube with THF (Wako Chemical). The raw materials were reacted by shaking for 12 h at 30°C. The suspension was centrifuged at 10000 rpm for 5 min and then dried for 30 min under vacuum at room temperature. Annealing was carried out at 80°C, 100°C, or 120°C for 3–12 h. Additionally, Li_3PS_4 was prepared by the mechanical milling of Li_2S and P_2S_5 (mol ratio 3:1) with zirconia balls at 370 rpm for 30 h for a reference material. All processes were carried out in an argon-filled glove box.

4.2.2. Thermogravimetric analysis (TGA) and XRD measurement

The TGA measurements for the samples were conducted with a Thermo plus EVO02 (Rigaku); the TGA chamber was purged with N_2 gas after the alumina pan loaded with the sample powder was transferred to a glove box. The weight loss of the sample was estimated between 25°C and 350°C with the temperature increasing at 10°C min^{-1} and 2°C min^{-1} under a N_2 atmosphere.

XRD measurements of the annealed samples prepared through liquid-phase synthesis using THF were carried out with an RINT-Ultima III (Rigaku) with CuKα radiation. All samples were prepared in a special holder in the glove box to prevent air exposure.

4.2.3. High-energy XRD coupled with PDF analysis

The prepared samples were sealed in a 2ϕ quartz capillary tube to prevent air exposure and analyzed using high-energy XRD. The measurement was conducted using the BL08W beamline at SPring-8 (Japan). The samples were irradiated with 115 keV (0.108 Å) X-ray, and the scattered X-ray were detected using a flat-panel detector. The structure factor, $S(Q)$, was obtained through the standardization of the collected scattering data from the number of atoms and the scattering intensity from one atom. In addition, the reduced PDF, $G(r)$, was calculated using the Fourier transform of $S(Q)$.

4.2.4. Ionic conductivity measurement

All of the samples prepared using THF were pressed into dense pellets, each with a thickness and diameter of approximately 0.7 and 10 mm, respectively, by two stainless steel rods with a pressure of 360 MPa in an argon-filled glove box. The ionic conductivity was measured using alternating current impedance at 25°C in the frequency range of 1.0 MHz to 0.1 Hz with an amplitude of 100 mV using ModuLab XM ECS (Solartron Analytical). Nyquist plots showed a semi-arc at high frequencies and a straight line at lower frequencies. The total conductivity was determined by using the intercept between the semi-arc and straight line as the total resistance through the obtained Nyquist plots.

4.3. Results and Discussion

The TGA curves of the samples synthesized via liquid-phase synthesis using THF and ethyl propionate are shown in Figure 1. TGA result with different heating rates

were shown in Figure 2. The samples showed weight loss due to solvent volatilization at 50°C. The sample prepared using ethyl propionate showed drastic weight loss from approximately 50°C to 120°C, whereas the sample prepared using THF showed drastic weight loss from approximately 50°C to 100°C. In case of TGA results measured at 2°C min^{-1}, the tendency of weight loss was similar to that of 10 °C min^{-1}, while the tendency for THF to show larger weight loss than ethyl propionate at lower temperatures was more pronounced in case of TGA results measured at 2°C min^{-1}. These results revealed that solvent could be removed from the material prepared using THF at a lower temperature.

In order to examine the effect of annealing on ionic conductivity, we annealed materials prepared using THF at 80°C, 100°C, and 120°C for various times. The lithium ionic conductivities of these samples are shown in Figure 3. The Nyquist plots of all samples measured to determine the ionic conductivity were shown in Figure 4. The lithium ionic conductivity of the sample annealed at 80°C gave a volcano plot with annealing time, and the highest value was 1.94×10^{-4} S cm^{-1} at 6 h. In the cases of the samples annealed at 100°C and 120°C, the lithium ionic conductivity decreased with increasing annealing time. In the case of the sample prepared using ethyl propionate and annealed at 80°C, the ionic conductivity increased gradually and reached a maximum (1.09×10^{-4} S cm^{-1}) at 12 h, as shown by the black plot in Figure 2. After this, the ionic conductivity decreased with increasing annealing time. The maximum ionic conductivity of the sample prepared using THF and annealed at 80°C was higher than that of the sample prepared using ethyl propionate. However, the ionic conductivity was lower than that of Li_3PS_4 prepared using the mechanical milling method. In order to determine the reason for this ionic conductivity difference, we analyzed the structure of the samples prepared using THF and annealed at 80°C.

The XRD patterns of the samples prepared in THF and annealed at 80°C for different times are shown in Figure 5 (a). Those of the samples prepared in THF and annealed at 100°C and 120°C are shown in Figure 6. For the samples annealed at 100°C and 120°C, Bragg peaks for β-Li_3PS_4 (space group *Pnma*) were observed in all cases. The samples annealed at 80°C for less than 6 h showed only a broad peak. In contrast, the sample annealed for more than 6 h showed Bragg peaks, which were attributed to β-Li_3PS_4, and the intensity increased with increasing annealing time. This result indicates that the samples annealed for less than 6 h had amorphous structures and that crystallization progressed with increasing annealing time. We compared the XRD patterns of the samples prepared using THF and ethyl propionate and annealed at 80°C with the highest ionic conductivities and Li_3PS_4 prepared using the mechanical milling method (Figure 5 (b)) to find differences in their ionic conductivities. The samples prepared using ethyl propionate and THF showed Bragg peaks for Li_3PS_4. The peak intensity for the sample prepared using THF and annealed at 80°C for 6 h was lower than that for the sample prepared using ethyl propionate. This result suggests that the ionic conductivity of the sample prepared in THF was higher than that of the sample prepared in ethyl propionate because crystallization was suppressed by THF, which has a lower boiling point than ethyl propionate. However, the ionic conductivity of the sample prepared in THF was lower than that of Li_3PS_4 prepared using the mechanical milling method, although the structure of the sample prepared in THF was almost amorphous. Because quantitative evaluation of the crystallinity of Li_3PS_4 from the XRD results was difficult, the relationship with ionic conductivity could not be understood clearly.

Hence, we examined the samples annealed at 80°C using high-energy XRD measurement coupled with PDF analysis, which can quantitatively evaluate both

crystalline and amorphous structures.

The reduced PDFs, $G(r)$, of the sample prepared in THF and annealed at 80°C for different times and Li_3PS_4 prepared using the mechanical milling method are shown in Figure 7 (a). These samples gave peaks at 2.0, 3.3, 4.1, and 7.0 Å, which were attributed to the P–S correlation in the PS_4^{3-} anion unit, the S–S correlation in the PS_4^{3-} anion unit, the S–S correlation between PS_4^{3-} anion units, and the P–P correlation between PS_4^{3-} anion units, respectively[27]. The peak intensity for the S–S correlation between PS_4^{3-} anion units (4.1 Å) increased with increasing annealing time. It has been reported that the peak intensity for this correlation increases with increasing crystallinity[54]. Therefore, the crystallinity of the sample prepared in THF and annealed at 80°C was increased by increasing the annealing time. As shown in Figure 7 (b), a shoulder peak near 4 Å appeared for the samples prepared using THF and annealed at 80°C, but not for Li_3PS_4 prepared using the mechanical milling method. These shoulder peaks are considered to represent an intermediate and are discussed in more detail below.

It has been reported that the crystallinity can be quantitatively evaluated by reproducing experimental PDF with amorphous and crystalline Li_3PS_4 using the following equation[27]:

$$G(r)_{\text{experimental data}} = (1 - \text{x})\, G(r)_{\text{amorphous}} + \text{x}\, G(r)_{\text{crystal}}$$

where $G(r)_{\text{experimental data}}$, $G(r)_{\text{amorphous}}$, $G(r)_{\text{crystal}}$, and x are the reduced PDFs of the samples prepared using THF and ethyl propionate and annealed at 80°C, reduced PDF of Li_3PS_4 prepared through mechanical milling, reduced PDF of Li_3PS_4 prepared through mechanical milling and annealed at 270°C, and crystallinity, respectively. We quantitatively evaluated the crystallinities of the samples prepared using THF and ethyl propionate and annealed at 80°C for different times by using the same method to

determine the effect of crystallinity on ionic conductivity. The crystallinities of these samples are shown in Figure 8 (a). The PDFs calculated from amorphous and crystalline Li_3PS_4 with experimental data are shown in Figure 9. The crystallinities of the samples prepared using THF and ethyl propionate both increased with increasing annealing time. It was found that crystallization progressed with annealing time regardless of the solvent. The correlations between the crystallinities and the ionic conductivities of the samples prepared using THF and ethyl propionate and annealed at 80°C are shown in Figure 8 (b). It has been reported that the ionic conductivity of Li_3PS_4 with a crystal structure is lower than that of amorphous Li_3PS_4[27,28]. In the case of the samples prepared in THF and annealed at 80°C for more than 6 h, the ionic conductivity decreased with increasing crystallinity. However, the ionic conductivity increased when the sample was annealed for less than 6 h despite the increasing crystallinity. In addition, the ionic conductivity of the sample prepared with ethyl propionate did not change despite the increase in crystallinity. It was revealed that the ionic conductivity decreased because the crystallinity was increased by annealing for a long time. However, the effect of crystallinity alone cannot explain why the ionic conductivity increased despite the increasing crystallinity with short annealing times. Therefore, we considered that there are other factors in addition to crystallinity.

As shown in Figure 7 (b), the samples prepared using THF gave a shoulder peak at approximately 4.24 Å, and this peak decreased in intensity with increasing annealing time. This tendency was observed in a previous study on ethyl propionate[29]. In a previous paper, it was proposed that a complex comprising Li_3PS_4 and ethyl propionate with different coordination numbers is formed as an intermediate owing to volatilization of solvent during the annealing process, and that this intermediate was retained after

annealing for a long time[29]. It is thought that this intermediate is present in the sample prepared using THF and annealed at 80°C, as reported in the past. Therefore, Raman measurements of the sample prepared in THF and annealed at 80°C were performed to confirm the identity of the solvent residue, as shown in Figure 10. Before it was annealed, the sample showed a peak at around 2900 cm^{-1} attributed to THF. The intensity of this peak decreased dramatically after annealing at 80 °C for 3 h and gradually afterwards. Moreover, the peak intensity decreased significantly after annealing at 80°C for 24 h. This result suggests that THF remained in the samples as part of the intermediate, but the amount was small. Based on the results of the Raman measurement, we concluded, as in the previous report, that the shoulder peak observed from PDF analysis (Figure 7 (b)) may be attributed to the intermediate formed during the annealing process. Therefore, it was considered that the ionic conductivity increased despite the increase in crystallinity because the amount of the residual intermediate decreased. Since ethyl propionate has a boiling point of 99°C, it is difficult to remove from the sample at 80°C. Therefore, the sample prepared using ethyl propionate and annealed at 80 °C contained a high amount of the intermediate. In contrast, the amount of the intermediate in the samples prepared using THF was lower because THF has a lower boiling point and is removed more easily. Therefore, it is suggested that using THF, which has a lower boiling point, improved ionic conductivity because THF could be removed while suppressing crystallization. We compared our results with those of previous papers that synthesized Li_3PS_4 using solvents different from those used in this study such as N-methyldormaide[18] and acetonitrile[24]. Figure 11 shows the correlation between boiling point and ionic conductivity of Li_3PS_4 including the results of this study and previous reports[18,24]. The ionic conductivity shows

a tendency to increase with decreasing boiling point. This tendency also supported our conclusion that using the solvents with low boiling points improves ionic conductivity.

The ionic conductivity of the sample prepared in THF was lower than that of Li_3PS_4 prepared using the mechanical milling method, although the crystallinity was similar. These results suggest that the relatively low ionic conductivity of the sample prepared in THF is attributed to the intermediate that is formed during the annealing process, which is difficult to remove.

4.4. Conclusion

In this study, we used THF as the solvent in the liquid-phase synthesis of Li_3PS_4 because of its low boiling point (66°C). We succeeded in synthesizing Li_3PS_4 with an amorphous structure and improved its ionic conductivity, which was higher (1.85×10^{-4} S cm^{-1}) than that of Li_3PS_4 prepared with ethyl propionate (1.09×10^{-4} S cm^{-1}). However, the ionic conductivity of Li_3PS_4 prepared using THF was lower than that of Li_3PS_4 prepared using the mechanical milling method. Hence, we attempted to determine the reasons for this using high-energy XRD coupled with PDF analysis. PDF analysis revealed that the crystallization of Li_3PS_4 can be suppressed by using THF, which has a lower boiling point than ethyl propionate. Because of this suppression, Li_3PS_4 prepared using THF showed improved ionic conductivity compared to that of Li_3PS_4 prepared using ethyl propionate. However, the solvent could not be removed completely while maintaining an amorphous structure, and thus, the ionic conductivity was lower than that obtained from the solid-phase synthesis method. We believe that this study can provide a guideline for selecting the solvent in liquid-phase synthesis.

Reference

1. Dunn, B.; Kamath, H.; Tarascon, J.-M. Electrical Energy Storage for the Grid: A Battery of Choices. *Science* **2011**, *334*, 928–935.
2. Zubi, G.; Dufo-López, R.; Carvalho, M.; Pasaoglu, G. The Lithium-Ion Battery: State of the Art and Future Perspectives. *Renew. Sustain. Energy Rev*. **2018**, *89*, 292–308.
3. Wu, H.; Cui, Y. Designing Nanostructured Si Anodes for High Energy Lithium Ion Batteries. *Nano Today* **2012**, *7*, 414–429.
4. Islam, M. S.; Fisher, C. A. J. Lithium and Sodium Battery Cathode Materials: Computational Insights into Voltage, Diffusion and Nanostructural Properties. *Chem. Soc. Rev.* **2014**, *43,* 185–204.
5. Seh, Z. W.; Sun, Y.; Zhang, Q.; Cui, Y. Designing High-Energy Lithium–Sulfur Batteries. *Chem. Soc. Rev.* **2016**, *45*, 5605–5634.
6. Hayashi, A.; Hama, S.; Morimoto, H.; Tatsumisago, M.; Minami, T. Preparation of Li_2S-P_2S_5 Amorphous Solid Electrolytes by Mechanical Milling. *J. Am. Ceram. Soc.* **2004**, *84*, 477–479.
7. Minami, K.; Hayashi, A.; Tatsumisago, M. Preparation and Characterization of Superionic Conducting $Li_7P_3S_{11}$ Crystal from Glassy Liquids. *J. Ceram. Soc. Japan* **2010**, *118*, 305–308.
8. Deiseroth, H.-J.; Kong, S.-T.; Eckert, H.; Vannahme, J.; Reiner, C.; Zaiß, T.; Schlosser, M. Li_6PS_5X: A Class of Crystalline Li-Rich Solids With an Unusually High Li^+ Mobility. *Angew. Chem., Int. Ed.* **2008**, *120*, 767–770.
9. Boulineau, S.; Courty, M.; Tarascon, J.-M.; Viallet, V. Mechanochemical Synthesis of Li-Argyrodite Li_6PS_5X (X=Cl, Br, I) as Sulfur-Based Solid Electrolytes for All Solid State Batteries Application. *Solid State Ionics* **2012**, *221*, 1–5.

10. Kamaya, N.; Homma, K.; Yamakawa, Y.; Hirayama, M.; Kanno, R.; Yonemura, M.; Kamiyama, T.; Kato, Y.; Hama, S.; Kawamoto, K.; Mitsui, A. A Lithium Superionic Conductor. *Nat. Mater.* **2011**, *10*, 682–686.
11. Sakuda, A.; Hayashi, A.; Tatsumisago, M. Sulfide Solid Electrolyte with Favorable Mechanical Property for All-Solid-State Lithium Battery. *Sci. Rep.* **2013**, *3*, 2261.
12. Nam, Y. J.; Cho, S.-J.; Oh, D. Y.; Lim, J.-M.; Kim, S. Y.; Song, J. H.; Lee, Y.-G.; Lee, S.-Y.; Jung, Y. S. Bendable and Thin Sulfide Solid Electrolyte Film: A New Electrolyte Opportunity for Free-Standing and Stackable High-Energy All-Solid-State Lithium-Ion Batteries. *Nano Lett.* **2015**, *15*, 3317–3323.
13. Muramatsu, H.; Hayashi, A.; Ohtomo, T.; Hama, S.; Tatsumisago, M. Structural Change of Li_2S–P_2S_5 Sulfide Solid Electrolytes in the Atmosphere. *Solid State Ionics* **2011**, *182*, 116–119.
14. Auvergniot, J.; Cassel, A.; Ledeuil, J.-B.; Viallet, V.; Seznec, V.; Dedryvère, R. Interface Stability of Argyrodite Li_6PS_5Cl toward $LiCoO_2$, $LiNi_{1/3}Co_{1/3}Mn_{1/3}O_2$, and $LiMn_2O_4$ in Bulk All-Solid-State Batteries. *Chem. Mater.* **2017**, *29*, 3883–3890.
15. Tachez, M.; Malugani, J.; Mercier, R.; Robert, G. Ionic Conductivity of and Phase Transition in Lithium Thiophosphate Li_3PS_4. *Solid State Ionics* **1984**, *14*, 181–185.
16. Murayama, M.; Kanno, R. Synthesis of New Lithium Ionic Conductor Thio-LISICON—Lithium Silicon Sulfides System. *J. Solid State Chem.* **2002**, *168*, 140–148.
17. Liu, Z.; Fu, W.; Payzant, E. A.; Yu, X.; Wu, Z.; Dudney, N. J.; Kiggans, J.; Hong, K.; Rondinone, A. J.; Liang, C. Anomalous High Ionic Conductivity of Nanoporous β-Li_3PS_4. *J. Am. Chem. Soc.* **2013**, *135*, 975–978.
18. Teragawa, S.; Aso, K.; Tadanaga, K.; Hayashi, A.; Tatsumisago, M. Liquid-Phase

Synthesis of a Li_3PS_4 Solid Electrolyte Using N-Methylformamide for All-Solid-State Lithium Batteries. *J. Mater. Chem. A* **2014**, *2*, 5095-5099.

19. Matuda, A.; Muto, H.; H.H. Phuc, N. Preparation of Li_3PS_4 Solid Electrolyte by Liquid-Phase Shaking Using Organic Solvents with Carbonyl Group as Complex Forming Medium. *J. Japan Soc. Powder Powder Metall.* **2016**, *63*, 976–980.
20. Phuc, N. H. H.; Morikawa, K.; Totani, M.; Muto, H.; Matsuda, A. Chemical Synthesis of Li_3PS_4 Precursor Suspension by Liquid-Phase Shaking. *Solid State Ionics* **2016**, *285*, 2–5.
21. Phuc, N. H. H.; Morikawa, K.; Mitsuhiro, T.; Muto, H.; Matsuda, A. Synthesis of Plate-like Li_3PS_4 Solid Electrolyte via Liquid-Phase Shaking for All-Solid-State Lithium Batteries. *Ionics* **2017**, *23*, 2061–2067.
22. Lim, H.-D.; Yue, X.; Xing, X.; Petrova, V.; Gonzalez, M.; Liu, H.; Liu, P. Designing Solution Chemistries for the Low-Temperature Synthesis of Sulfide-Based Solid Electrolytes. *J. Mater. Chem. A* **2018**, *6*, 7370–7374.
23. Choi, S.; Lee, S.; Park, J.; Nichols, W. T.; Shin, D. Facile Synthesis of Li_2S-P_2S_5 Glass-Ceramics Electrolyte with Micron Range Particles for All-Solid-State Batteries via a Low-Temperature Solution Technique. *Appl. Surf. Sci.* **2018**, *444*, 10–14.
24. Wang, H.; Hood, Z. D.; Xia, Y.; Liang, C. Fabrication of Ultrathin Solid Electrolyte Membranes of β-Li_3PS_4 Nanoflakes by Evaporation-Induced Self-Assembly for All-Solid-State Batteries. *J. Mater. Chem. A* **2016**, *4*, 8091–8096.
25. Wang, Y.; Lu, D.; Bowden, M.; El Khoury, P. Z.; Han, K. S.; Deng, Z. D.; Xiao, J.; Zhang, J.-G.; Liu, J. Mechanism of Formation of $Li_7P_3S_{11}$ Solid Electrolytes through Liquid Phase Synthesis. *Chem. Mater.* **2018**, *30*, 990–997.
26. Suto, K.; Bonnick, P.; Nagai, E.; Niitani, K.; Arthur, T. S.; Muldoon, J. Microwave-

Aided Synthesis of Lithium Thiophosphate Solid Electrolyte. *J. Mater. Chem. A* **2018**, *6*, 21261–21265.

27. Shiotani, S.; Ohara, K.; Tsukasaki, H.; Mori, S.; Kanno, R. Pair Distribution Function Analysis of Sulfide Glassy Electrolytes for All-Solid-State Batteries: Understanding the Improvement of Ionic Conductivity under Annealing Condition. *Sci. Rep.* **2017**, *7*, 6972.
28. Tsukasaki, H.; Mori, S.; Shiotani, S.; Yamamura, H. Ionic Conductivity and Crystallization Process in the Li_2S–P_2S_5 Glass Electrolyte. Solid State Ionics **2018**, *317*, 122–126.
29. Yamamoto, K.; Takahashi, M.; Ohara, K.; Phuc, N. H. H.; Yang, S.; Watanabe, T.; Uchiyama, T.; Sakuda, A.; Hayashi, A.; Tatsumisago, M.; Muto, H.; Matsuda, A.; Uchimoto, Y. Synthesis of Sulfide Solid Electrolytes through the Liquid Phase: Optimization of the Preparation Conditions. *ACS Omega* **2020**, *5*, 26287-26294.

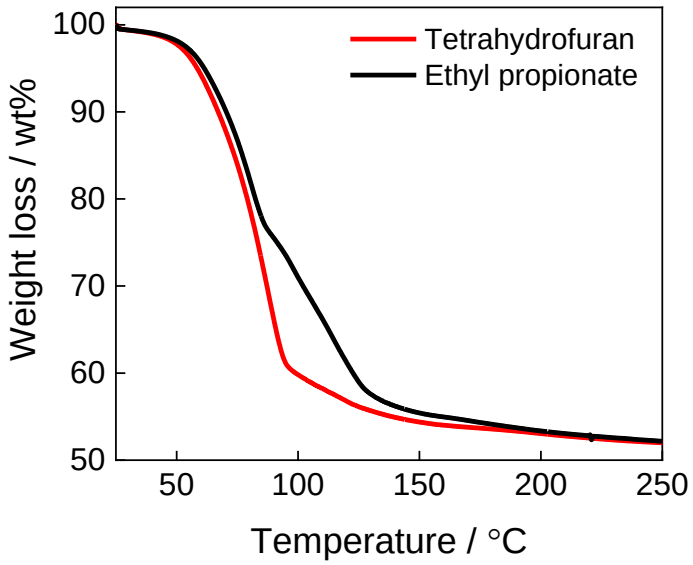

Figure 1. TGA results for samples synthesized using THF and ethyl propionate from 25 °C to 350 °C with heating at 10°C min^{-1} under a N_2 atmosphere.

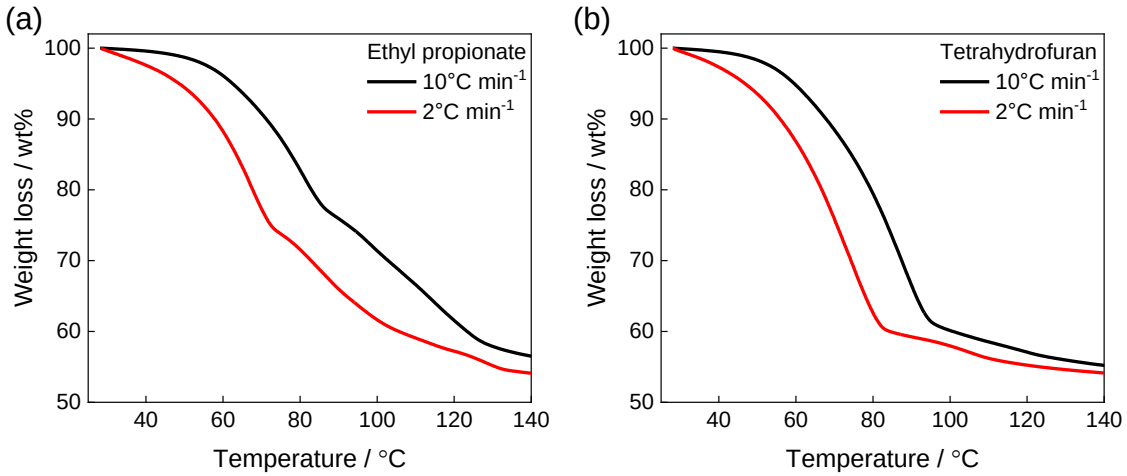

Figure 2. TGA results for samples synthesized using (a) ethyl propionate and (b) THF from 25°C to 250°C with heating at 10 °C min^{-1} and 2°C min^{-1} under a N_2 atmosphere.

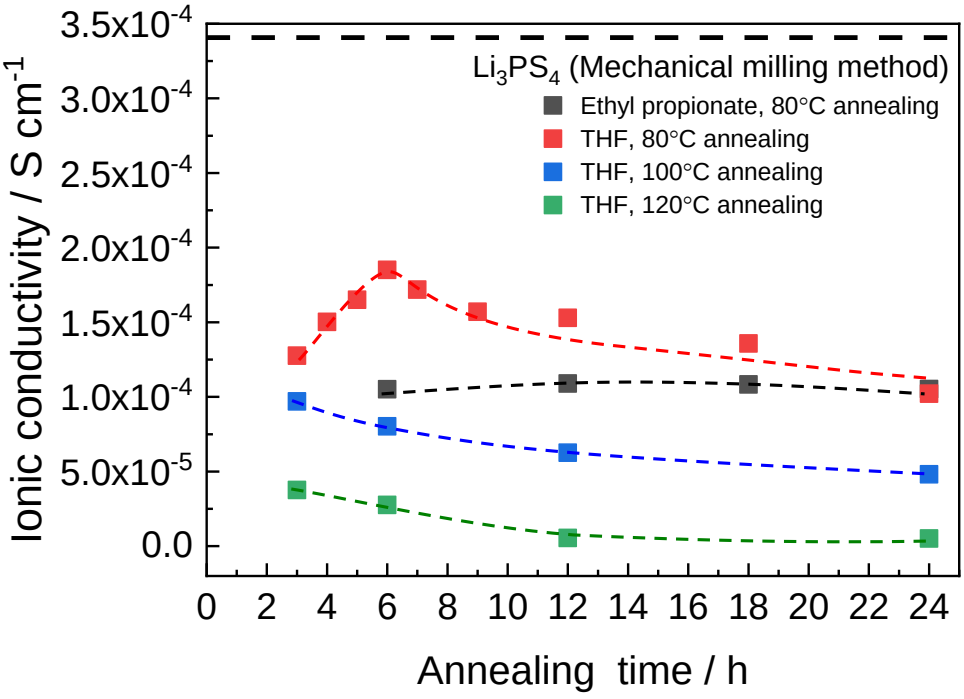

Figure 3. Comparison of ionic conductivities of samples prepared using THF and annealed with different annealing temperatures and times. The black plot represents the samples prepared using ethyl propionate and annealed at 80°C. The red, blue, and green plots represent the samples prepared using THF and annealed at 80°C, 100°C, and 120°C, respectively.

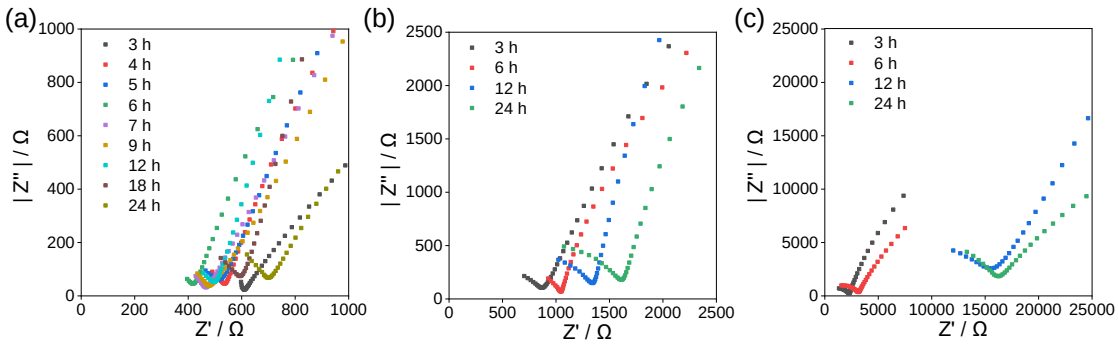

Figure 4. Nyquist plots of the samples the samples prepared using THF and annealed at (a) 80°C, (b)100°C, and (c)120°C, respectively.

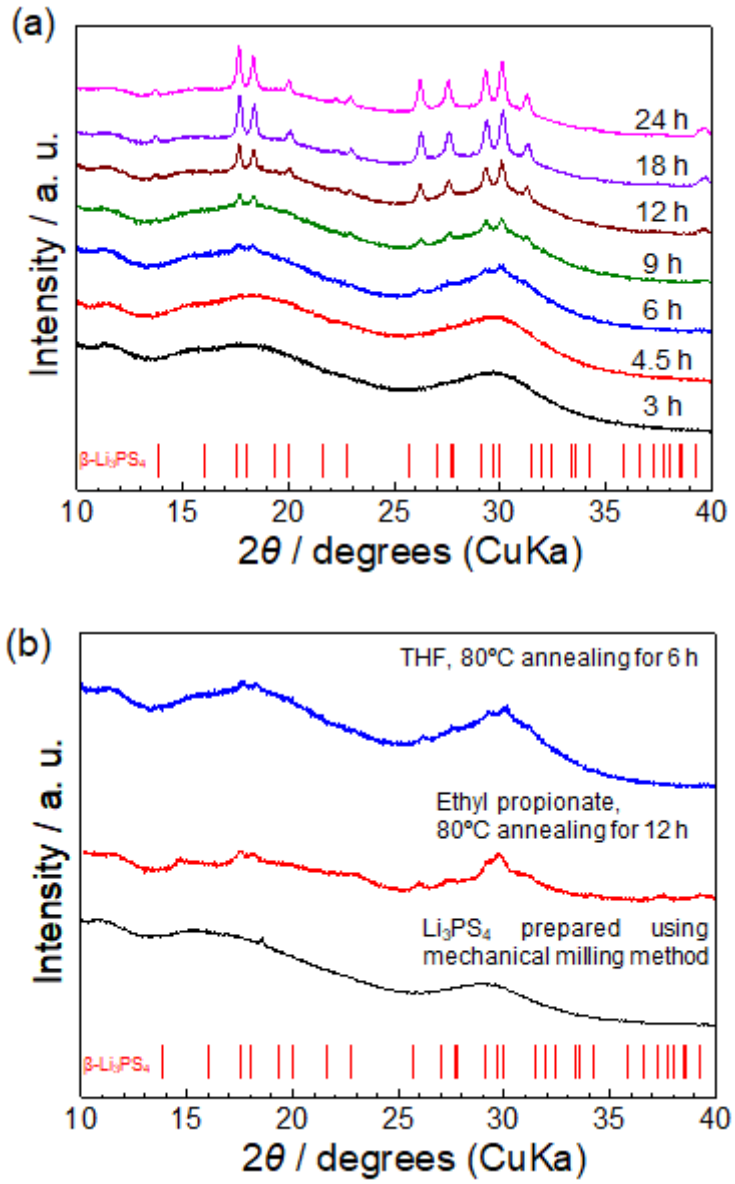

Figure 5. (a) XRD patterns of the samples prepared using THF and annealed at 80°C for different times. (b) Comparison of XRD patterns of the sample prepared through mechanical milling, the sample prepared using THF and annealed at 80°C for 6 h, and the sample prepared using ethyl propionate and annealed at 80°C for 12 h.

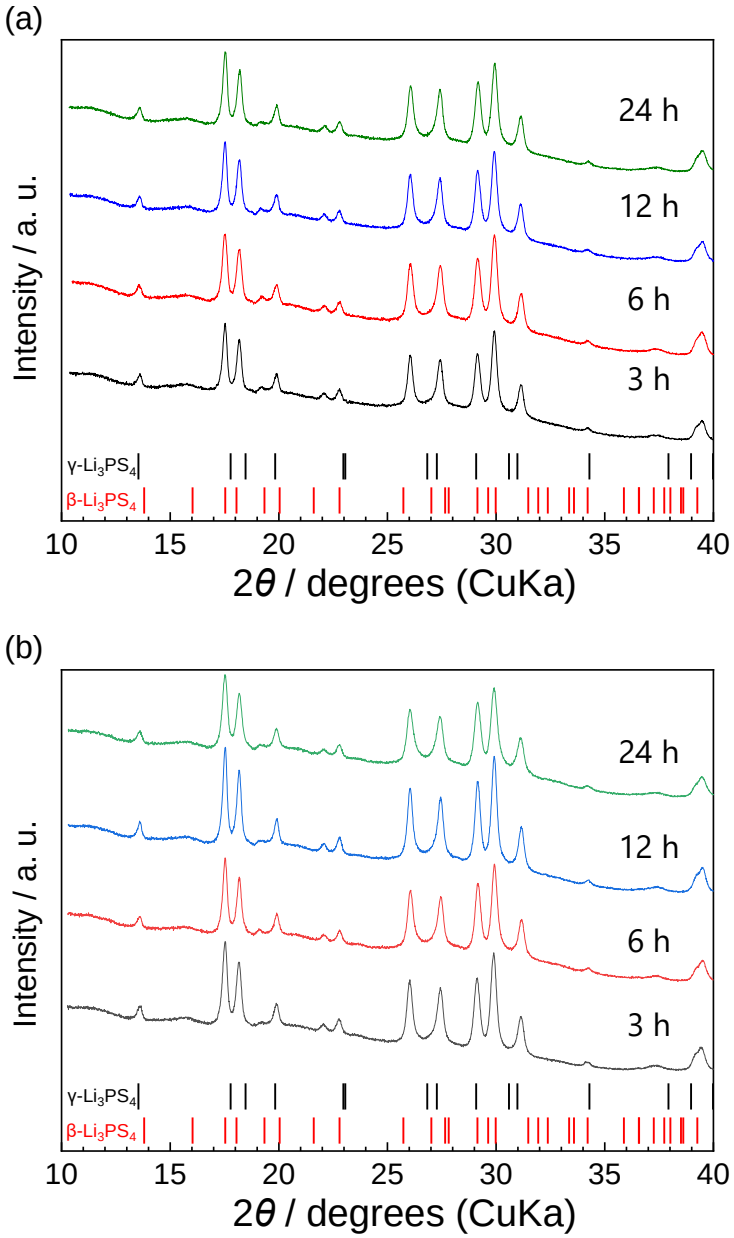

Figure 6. XRD patterns of samples annealed at (a) 100°C and (b) 120°C for different times.

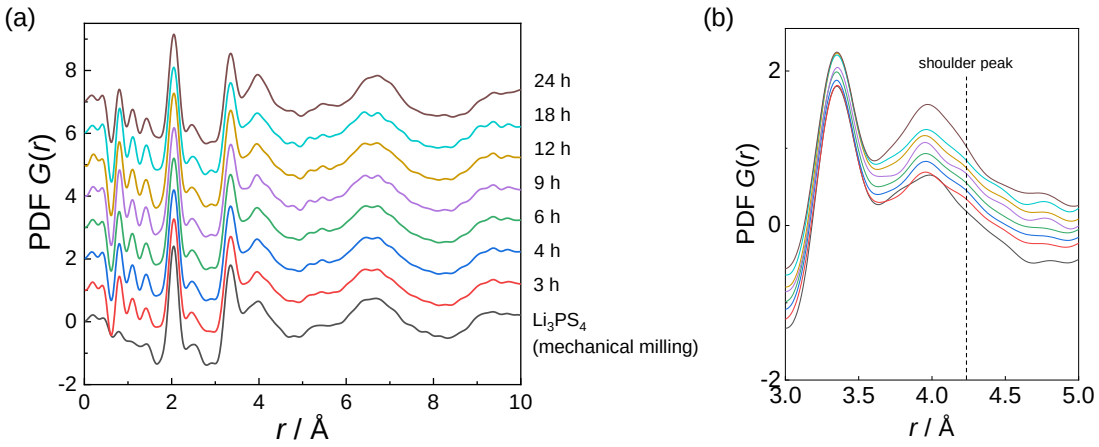

Figure 7. PDF analysis results for the samples prepared using THF and annealed at 80°C for different times. (b) Enlarged view of the 3–5 Å region.

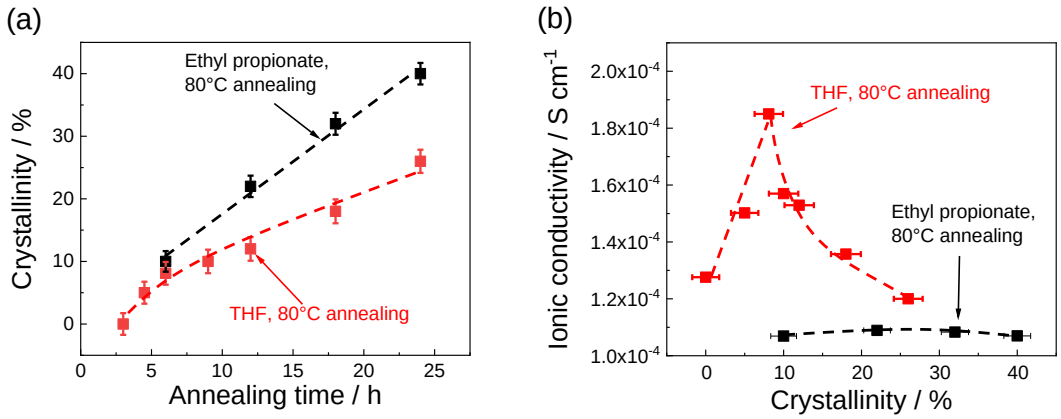

Figure 8. (a) Annealing time dependences at 80°C of the crystallinities of the samples prepared using THF (red line) and ethyl propionate (black line). (b) Correlations between the crystallinity and lithium ionic conductivity of the samples prepared using THF (red plot) and ethyl propionate (black plot) and annealed at 80°C

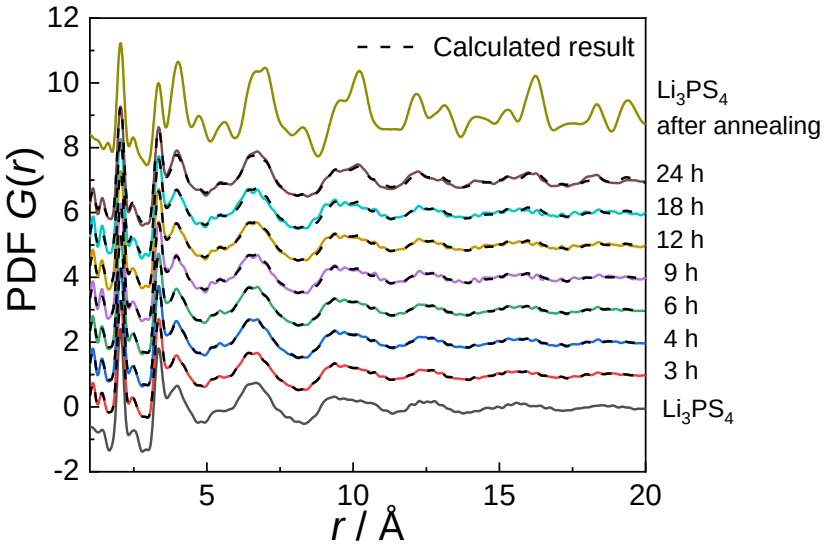

Figure 9. Results of PDF fitting of samples prepared using THF and annealed at 80°C for different times.

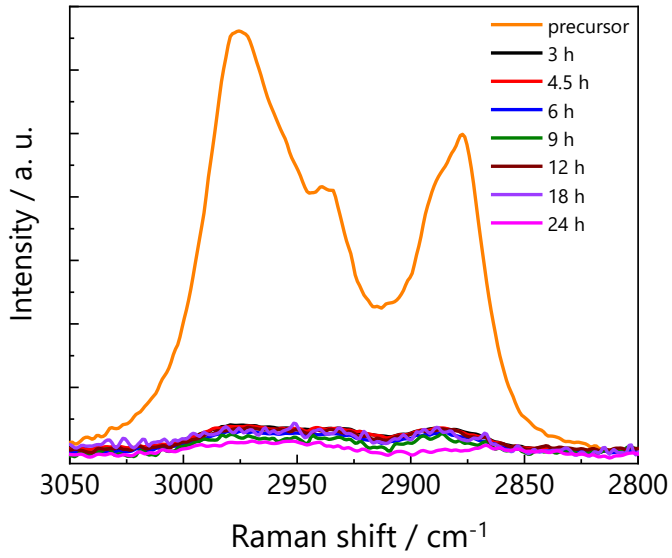

Figure 10. Raman spectra of samples prepared using THF and annealed at 80°C for different annealing times.

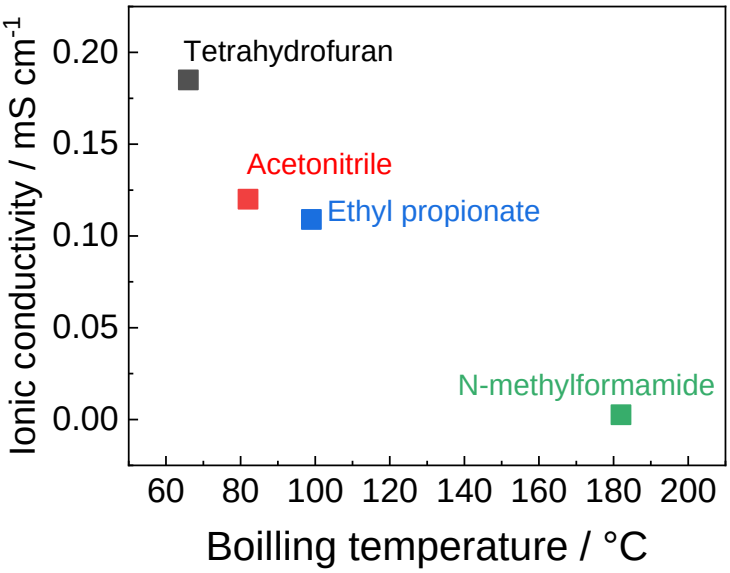

Figure 11. Correlation between boiling temperature of solvents and ionic conductivity of Li_3PS_4 prepared by using each solvent. The ionic conductivity obtained by using acetonitrile and N-methyldormaide are referred from previous studies[18,24].

Chapter 5. Elucidation of Relationship between Local Structure and Lithium Ion Conductivity of LiI-doped Li_3PS_4 for Li Dendrite Suppression by Using Pair Distribution Function Analysis

5.1. Introduction

Increasing the cruising ranges of electric vehicles and developing high-energy-density batteries for this purpose are highly desired.[1–5] Among current secondary batteries, lithium ion secondary batteries have the highest energy density, and it is considered that the use of a lithium metal anode can further improve the energy density. Lithium metal is a promising anode material for high-energy-density batteries because of the high theoretical capacity (3860 mAh g^{-1}) and low electrochemical potential (−3.04 V vs. standard hydrogen electrode).[6] However, the risk of thermal runaway due to internal short-circuiting caused by lithium dendrite formation and degradation of cycle characteristics are problems that must be solved toward using lithium metal as an anode.[7–9] Therefore, the suppression of lithium dendrite formation is important for the practical use of lithium metal anodes.

Inorganic solid electrolytes are believed to act as barriers to dendrite growth owing to their high shear moduli.[10,11] However, even with inorganic solid electrolytes, dendrite

formation has not been suppressed to the extent of practical use.[12–15] The factors that contribute to dendrite formation are believed to be 1) non-uniform mechanical con-tact between lithium metal and the solid electrolyte, 2) the physical properties of the interface between lithium metal and the solid electrolyte, and 3) non-uniform current density due to low ionic conductivity.[16,17] Various efforts to suppress lithium dendrite growth have been made, including the use of lithium alloys, modification of the interface between lithium metal and the solid electrolyte, and intro-duction of a lithium halide.[18–24] The addition of a halogen compound such as LiI to the solid electrolyte is one of the most feasible methods.[23,24] This suppresses lithium dendrite growth for long periods of time.[23,24] It has been hypothesized that lithium dendrite growth is influenced by both the formation of thermodynamically stable LiI on the lithium metal/electrolyte interface, which inhibits the reductive decomposition of the interface, and physical properties such as the ionic conductivity of the solid electrolyte.[23,24] Recently, we have reported the effect of suppressing the growth of lithium dendrite by adding lithium iodide to stabilize the interface.[25] However, it is currently unclear whether the improvement of interface stability or ionic conductivity due to LiI addition contributes to the suppression of lithium dendrites. To design materials for further dendrite suppression, it is necessary to clarify the structure of the material and the effect of each factor on dendrite growth. To accomplish these goals, the local structure of the iodide ions in the solid electrolyte, which affects film formation at the interface, must be determined.

In this study, LiI-doped Li_3PS_4 solid electrolytes were synthesized using the mechanical milling method and annealed at different temperatures. The structures before and after annealing were determined by comparing the results of high-energy X-ray diffraction (XRD) coupled with pair distribution function (PDF) analysis with simulation

results. The effect of the lithium/solid electrolyte interface on the lithium dendrite suppression capability was determined by observing the structure and morphology through X-ray absorption spectroscopy (XAS) and X-ray computed tomography (CT) measurements. In addition, the effect of the ionic conductivity on the dendrite suppression capability was clarified by determining the relationship between them. The results revealed that lithium dendrite suppression is due to not only the suppression of electrolyte reduction by the addition of LiI, but also the improvement of the uniformity of the current density distribution through the improvement of the ionic conductivity.

5.2. Experimental Section

5.2.1. Synthesis and annealing of the (100-x) Li_3PS_4 – x LiI solid electrolyte

Li_2S (Sigma-Aldrich, > 99.9%), P_2S_5 (Sigma-Aldrich, 99%), and LiI (Sigma-Aldrich, > 99.99%) were mixed in an agate mortar at appropriate molar ratios to produce (100−x)Li_3PS_4-xLiI such that x = 0, 10, 20, 30, 40, 50, or 60. The mixed powder was placed in a zirconia pod along with 90 g of 4ϕ zirconia balls and subjected to high-energy ball milling at 600 rpm for 10 h. The (100−x)Li_3PS_4-xLiI samples were annealed at 140–270 °C for 2 h. All procedures were carried out in an argon-filled glove box to prevent reaction with air.

5.2.2. Ionic conductivity measurement

Dense pellets ~0.7 mm thick and 10 mm in diameter were prepared by pressing the samples from both sides at 360 MPa using two stainless steel rods in an argon-filled

glove box. Alternating current impedance measurements were carried out at 25–100 °C in the 1.0 MHz to 0.1 Hz frequency range with an amplitude of 100 mV using ModuLab XM ECS (Solartron Analytical). The obtained Nyquist plots were used to determine the total conductivity.

5.2.3. Critical current density measurement for short-circuiting caused by lithium dendrite formation.

Pellets of the solid electrolyte were prepared by pressing the solid electrolyte at 360 MPa. The prepared pellets were held in place on both sides with 8ϕ Li metal and 10ϕ stainless steel foil. Additionally, the pellets were placed in a laminate cell and sealed under vacuum. The laminate cell underwent cold isostatic pressurization at 80 MPa to ensure good contact between lithium metal and the solid electrolyte. The lithium metal/solid electrolyte/lithium metal cells were subjected to galvanostatic cycling tests with the current density increasing by 0.04 mA cm^{-2} after charging and discharging for 1 h at 100 °C to evaluate the critical current density.

5.2.4. Characterization

XRD measurements of (100−x)Li_3PS_4-xLiI before and after annealing were performed using RINT-Ultima III (Rigaku) with CuKα radiation. Raman spectra between 50 and 1800 cm^{-1} were obtained using a DXR3 Smart Raman spectrometer (Thermo Fisher Scientific) with a 532 nm diode-pumped solid-state laser at room temperature. All samples were sealed in a non-exposure cell or glass tube in an argon-filled glove box to prevent reaction with air.

High-energy XRD was carried out at beamline BL04B2 at SPring-8 (Japan). Samples sealed in 2ϕ quartz capillary tubes were irradiated with 61.2 keV synchrotron radiation energy and the scattered X-rays were detected using seven point-type detectors. The structure factor $S(Q)$ was obtained by normalizing the scattering data to the number of atoms and the scattering intensity from one atom. Moreover, the reduced PDF, $G(r)$, was calculated through the Fourier transform of $S(Q)$.

X-ray CT measurements were conducted at beamline BL20XU at SPring-8 (Japan). Laminate cells containing the samples were irradiated with 30 keV synchrotron radiation, and transmission images were acquired at various angles. Laboratory-based X-ray CT measurements were performed using Xradia 520 Versa (Carl Zeiss Co., Ltd., USA).

XAS spectra of the samples before and after galvanostatic cycling tests in the S *K*-edge and P *K*-edge energy regions were measured using the partial fluorescence yield method at beamline BL27SU at SPring-8 (Japan). The samples before and after the galvanostatic cycling tests were sealed in a glove box filled with argon to prevent exposure to air after the stainless-steel foil was removed from both sides of the samples.

5.3. Results and Discussion

Figures 1(a) and (b) show the XRD patterns and lithium ionic conductivity of $(100-x)Li_3PS_4$-xLiI (x = 0, 10, 20, 30, 40, 50, or 60), respectively. The XRD pattern of the sample without LiI doping (x = 0) showed the broad peaks around 30°, similar to the XRD pattern of Li_3PS_4 in previous report.[24,26] The broad peaks around 30° were observed in LiI-doped samples, and the peak shifted to lower angle as the amount of LiI added increased. In addition, LiI-doped samples with x > 40 gave Bragg peaks attributable to

crystalline LiI (JCPDS No. 71-37466). This result suggests that the lattice constant was increased by the introduction of iodine, which has a larger ionic radius than sulfur. [23,27] The precipitation of crystalline LiI in the samples with x > 40 was considered to be due to the addition of an amount exceeding the solid solution limit. The ionic conductivity of (100−x)Li_3PS_4-xLiI increased with increasing LiI content up to x = 50. This trend is consistent with the results of previous study.[24] In previous studies, the reason of increasing ionic conductivity by introduction of iodine was considered to be the expansion of diffusion paths due to the increase in lattice constant.[23,27] Therefore, it can be inferred that this trend occurred because the introduction of LiI increased the ionic conductivity owing to the increase in lattice constant; however, as the amount of LiI introduced increased further, the ionic conductivity decreased because of the low ionic conductivity of LiI.

In order to investigate the effect of annealing temperature, XRD and Raman measurements were performed on 70Li_3PS_4-30LiI samples prepared without annealing and with annealing at various temperatures. The XRD patterns are shown in Figure 1(c). The XRD patterns of the samples annealed at 140 and 160 °C showed no Bragg peaks. In contrast, the samples annealed at 180 and 200 °C gave Bragg peaks attributable to a thio-LISICON II analog.[26,28] The sample annealed at 220 °C gave Bragg peaks attributable to the thio-LISICON II analog and Li_4PS_4I.[29] For the samples annealed at above 240 °C, the weak Bragg peaks of the thio-LISICON II analog did not appear, while the intensity of the Bragg peaks of Li_4PS_4I increased and a new Bragg peak attributable to β-Li_3PS_4 was observed.[30] These results suggest that the thio-LISICON II phase transformed into Li_4PS_4I and Li_3PS_4 as the annealing temperature increased. The Raman spectra of 70Li_3PS_4-30LiI samples prepared using the mechanical milling method and annealed at

various temperatures are shown in Figure 2. The spectrum of Li_3PS_4 is displayed for comparison. A peak at ~420 cm^{-1}, attributed to the vibration of the PS_4^{3-} anion[31], was observed for all samples. The peak position shifted to lower wavenumbers as the annealing temperature increased up to 200 °C and then returned to the original peak position as the annealing temperature increased further. Based on the XRD results, it is proposed that the formation of the thio-LISICON II phase caused this shift to lower wavenumbers. The thio-LISICON II phase, $Li_{3.25}P_{0.95}S_4$, is known to have a high ratio of sulfur to phosphorus.[32] The formation of the thio-LISICON II phase is thought to cause compositional variations and result in the formation of a P_2S_7 unit. Therefore, the formation of the P_2S_7 unit (410 cm^{-1}) with the formation of the thio-LISICON II phase may be the reason for the shift in the Raman spectra.

The ionic conductivities at 25 °C of $70Li_3PS_4$-30LiI prepared using the mechanical milling method and annealed at various temperatures for 2 h are shown in Figure 1(d). Arrhenius plots for these samples are shown in Figure 3 and the activation energies and frequency factors are listed in Table 1. The ionic conductivity increased with increasing annealing temperature until 200 °C, reaching 2.8 times the value of that unannealed, and then tended to decrease. The activation energy exhibited the opposite trend. The XRD and Raman measurements revealed that the thio-LISICON II phase was formed at annealing temperatures up to 200 °C, while Li_4PS_4I and Li_3PS_4 were formed at temperatures above 220 °C. The crystalline phases of thio-LISICON II are known to have high ionic conductivity,[32,33] while those of Li_3PS_4 and Li_4PS_4I have been reported to have low ionic conductivity.[29,34] This suggested that the change in the crystalline phase was one reason for the change in ionic conductivity with annealing temperature.

The presence of iodide ions in the solid electrolyte has a great influence on the formation of a lithium-iodide-containing film at the interface through the reaction between lithium metal and the solid electrolyte containing LiI.[23,24] However, it is difficult to determine the detailed structure of the solid electrolyte based on the XRD and Raman results alone. Therefore, high-energy XRD coupled with PDF analysis was performed for detailed structural characterization of the unannealed sample. Figure 4(a) shows the $G(r)$ of Li_3PS_4 and unannealed $70Li_3PS_4$-30LiI. Li_3PS_4 gave peaks at 2.0, 3.3, and 4.1 Å attributed to the P-S bond, S-S correlation in the PS_4^{3-} anion, and S-S correlation between the PS_4^{3-} anions, respectively.[35] Unannealed $70Li_3PS_4$-30LiI gave a peak at a similar position to that of Li_3PS_4. This result suggested that the correlations within the PS_4^{3-} anions were unaffected by the addition of LiI. To determine the structure in greater detail, we simulated the $G(r)$ of model structures and compared them with that of $70Li_3PS_4$-30LiI. The simulation was carried out using an inserted model, in which iodine was inserted between the PS_4^{3-} anions (Figure 4(b)), and an exchanged model, in which iodine was replaced by sulfur in the PS_4^{3-} anions (Figure 4(c)). These model structures were constructed using the structural model obtained from the calculations as a reference.[27] The red and blue lines in Figure 4(a) show the calculated PDFs from the inserted and exchanged models, respectively. Details of the peak assignments for each model structure are shown in Figure 5. The $G(r)$ of unannealed $70Li_3PS_4$-30LiI and the inserted model showed peaks at similar positions. The $G(r)$ of the exchanged model showed a characteristics peak at around 2.5 Å derived from the P-I bond, while the $G(r)$ of unannealed $70Li_3PS_4$-30LiI showed no peak derived from the P-I bond. From this result, it was found that iodine was inserted between the PS_4 anions. It has been reported that an iodine ion is difficult to replace with sulfur ion because an iodide ion has a significantly

larger ionic radius than a sulfur ion.[36,37] Our result is consistent with the reports, in other words, it suggests that an insertion-type structure was formed. From these results, we succeeded in determining the structure of the amorphous Li_3PS_4-LiI solid electrolyte. Similarly, the structure of annealed $70Li_3PS_4$-30LiI, which gave no clear Bragg XRD peaks, was examined using PDF analysis. The analysis results are shown in Figure 5. The results revealed that unannealed and annealed $70Li_3PS_4$-30LiI showed similar PDFs. This indicates that iodine does not replace sulfur in the PS_4^{3-} anion even after annealing. The dendrite suppression effect was investigated using unannealed and annealed $70Li_3PS_4$-30LiI, which both have iodine inserted between PS_4^{3-} anions.

The dendrite suppression capabilities of Li_3PS_4 and $70Li_3PS_4$-30 LiI before and after annealing were evaluated through galvanostatic cycling tests using lithium metal/solid electrolyte/lithium metal cells with stepwise increases in current density at 100 °C. Figure 6 shows the results of the galvanostatic cycling tests. For all samples, the cells showed a voltage drop after cycling. These voltage drops were attributed to internal short circuits due to the formation of lithium dendrites in the solid electrolyte. The current density at which the voltage drop occurred was defined as the critical current density of lithium dendrite formation. The dendrite suppression capability is generally evaluated based on the critical current density.[23,38,39] Figure 7(a) shows the critical current densities of the LiI-doped samples tended to increase with annealing temperature up to 200 °C and then decrease. To clarify the influence of ionic conductivity on the dendrite suppression capability, the relationship between the ionic conductivity and the critical current density was investigated and is shown in Figure 7(b). The critical current densities of the LiI-doped samples tended to increase with increasing ionic conductivity. However, Li_3PS_4 did not follow this trend.

In order to determine why Li_3PS_4 deviated from this trend, the morphology changes of Li_3PS_4 and $70Li_3PS_4$-30LiI after the galvanostatic cycling tests under the same conditions (Figure 8(a)) were examined using X-ray CT measurements (Figure 9, Figure 10, and Figure 8(b),(c)) and the reactivity of Li_3PS_4 and $70Li_3PS_4$-30LiI with the lithium metal was investigated by P *K*-edge (Figure 8(d)) and S *K*-edge XANES (Figure 8(e)). Millimeter-scale observations using a laboratory CT apparatus did not clearly observe the morphology between lithium metal and solid electrolyte (Figure 9). Therefore, Higher resolution CT measurements were performed. Li_3PS_4 and $70Li_3PS_4$-30LiI prepared via mechanical milling before the galvanostatic cycling tests showed uniform lithium metal/solid electrolyte interfaces (Figure 10). In the case of Li_3PS_4, the uniform lithium metal/solid electrolyte interface was broken and cracks formed after the galvanostatic cycling test (Figure 8(b)). In contrast, for $70Li_3PS_4$-30LiI, good interface contact between the solid electrolyte and lithium metal was maintained and no cracks were observed in the solid electrolyte (Figure 8(c)). We conducted P *K*-edge and S *K*-edge XAS measurements to detect decomposed products during galvanostatic cycling. The results of these measurements are shown in Figure 11. To see the changes in the spectra after the galvanostatic cycling tests, the respective P *K*-edge and S *K*-edge X-ray absorption near edge structure (XANES) spectra of Li_3PS_4 and $70Li_3PS_4$-30LiI before and after the galvanostatic cycling tests were subtracted to obtain the difference XANES spectra, which are shown in Figures 8(e) and (f).In the case of Li_3PS_4, the peak intensity decreased and a peak for Li_3P was also observed after the galvanostatic cycling test. Moreover, S *K*-edge XAS measurements showed that the peak intensity for Li_3PS_4 decreased and the spectrum of Li_2S was observed after the galvanostatic cycling test. Our previous studies

have also reported that the reduction layer at the lithium/Li_3PS_4 interface causes the formation of cracks in Li_3PS_4 and the crack promoted short cuircuit.[25]

On the other hand, the P *K*-edge and S *K*-edge XANES spectra of 70Li_3PS_4-30LiI showed almost no changes after the galvanostatic cycling test. The lack of changes indicated that the addition of LiI inhibited the decomposition of the solid electrolyte. A similar result to our previous study which reported that the addition of LiI suppresses the reduction reaction with lithium metal and the formation of cracks at the lithium/solid electrolyte interface was also obtained in this study.[25] These results revealed that Li_3PS_4 deviated from the correlation between ionic conductivity and critical current density found in the LiI-doped samples shown in Fig. 7(b) because of different resistances to reduction by lithium metal. This result clearly shows that the stabilization of the solid electrolyte / Li metal interface by the addition of LiI is not the main factor of the dendrite suppression effect, but a part of the suppression effect.

In order to clarify the effect of the ionic conductivity of the solid electrolyte on the lithium dendrite suppression capability, X-ray CT measurements were performed on 70Li_3PS_4-30LiI without annealing and that with annealing at 200 °C, which has the highest ionic conductivity, after the galvanostatic cycling tests until an internal short circuit occurred. The results of the galvanostatic cycling tests and X-ray CT measurements are shown in Figure 12. For both samples, cracks were observed after the galvanostatic cycling tests. The cracks in 70Li_3PS_4-30LiI annealed at 200 °C, with high ionic conductivity, were smaller than those in unannealed 70Li_3PS_4-30LiI. This is believed to be due to the dependence of the lithium ion flux on the ionic conductivity. When the ionic conductivity is high, the lithium ion flux is uniform, resulting in suppression of dendrite formation. As shown by these results, we have successfully

evaluated the contributions of the reductive stability of the interface and the ionic conductivity of the solid electrolyte to the dendrite suppression capability, and these are important in elucidating the dendrite growth suppression mechanism.

Figure 12 showed a scheme diagram of the dendrite suppression mechanism of the Li_3PS_4 and LiI doped Li_3PS_4. In the case of Li_3PS_4, the volume expansion caused by the decomposition of Li_3PS_4 into Li_2S and Li_3P reacting with Li metal forms cracks at the lithium metal/solid electrolyte interface, breaking the good interfacial contact. The poor interfacial contact causes rapid dendrite growth due to the partial concentration of current. In contrast, in the LiI doped Li_3PS_4, the reductive decomposition of the solid electrolyte was suppressed by the LiI doping, and the good interfacial contact was maintained. Therefore, dendrite growth is suppressed due to more uniform Li precipitation compared to Li_3PS_4. In addition, it was suggested that dendrite suppression was enhanced not only by the suppression of electrolyte reduction by LiI addition, but also by the improved uniformity of current density distribution due to the enhanced ionic conductivity. This information will be very useful in establishing design guidelines for materials to suppress dendrite growth.

5.4. Conclusion

In this study, the factors that determine the properties and lithium dendrite suppression capability of LiI-doped Li_3PS_4 with and without annealing treatment were studied. The ionic conductivity increased with increasing annealing temperature and, at 200 °C, reached 2.8 times the value of that unannealed, and then tended to decrease. The change in ionic conductivity was found to be due to the formation of a high-ionic-

conductivity thio-LISICON II phase and low-ionic-conductivity Li_3PS_4 and Li_4PS_4I phases. In addition, PDF analysis revealed that the LiI-doped Li_3PS_4 solid electrolyte has an inserted structure with iodine inserted between PS_4^{3-} anions, which is maintained even after annealing.

Although the critical current density and ionic conductivity of LiI-doped Li_3PS_4 showed a linear relationship, the Li_3PS_4 did not show the same correlation. The XAS and X-ray CT measurements proves that in the case of Li_3PS_4, the cracks attributed to lithium dendrite were observed at the lithium metal/solid electrolyte interface owing to volume expansion caused by decomposition into Li_2S and Li_3P. In contrast, in the case of LiI-doped Li_3PS_4, the cracks and decomposed product Li_2S and Li_3P, were not observed at the lithium metal/solid electrolyte interface even after experienced the critical current density of the Li_3PS_4. Although the cracks were observed in the LiI-doped Li_3PS_4 at relatively high current density, the magnitude of the crack was suppressed with increase of the ionic conductivity of the LiI-doped Li_3PS_4. These results indicate that lithium dendrite suppression is due to not only the suppression of electrolyte reduction by the addition of LiI, but also the improvement of the uniformity of the current density distribution through the improvement of the ionic conductivity. This information will be very useful for establishing design guidelines for materials for dendrite growth suppression.

Reference

1. Dunn, B.; Kamath, H.; Tarascon, J.-M. Electrical Energy Storage for the Grid: A Battery of Choices. *Science* **2011**, *334* (6058), 928–935.
2. Zubi, G.; Dufo-López, R.; Carvalho, M.; Pasaoglu, G. The Lithium-Ion Battery: State of the Art and Future Perspectives. *Renew. Sustain. Energy Rev.* **2018**, *89*, 292–308.
3. Wu, H.; Cui, Y. Designing Nanostructured Si Anodes for High Energy Lithium Ion Batteries. *Nano Today* **2012**, *7* (5), 414–429.
4. Islam, M. S.; Fisher, C. A. J. Lithium and Sodium Battery Cathode Materials: Computational Insights into Voltage, Diffusion and Nanostructural Properties. *Chem. Soc. Rev.* **2014**, *43* (1), 185–204.
5. Seh, Z. W.; Sun, Y.; Zhang, Q.; Cui, Y. Designing High-Energy Lithium–Sulfur Batteries. *Chem. Soc. Rev.* **2016**, *45* (20), 5605–5634.
6. Hatzell, K. B.; Chen, X. C.; Cobb, C. L.; Dasgupta, N. P.; Dixit, M. B.; Marbella, L. E.; McDowell, M. T.; Mukherjee, P. P.; Verma, A.; Viswanathan, V.; Westover, A. S.; Zeier, W. G. Challenges in Lithium Metal Anodes for Solid-State Batteries. *ACS Energy Lett.* **2020**, *5* (3), 922–934.
7. Kim, H.; Jeong, G.; Kim, Y. U.; Kim, J. H.; Park, C. M.; Sohn, H. J. Metallic Anodes for next Generation Secondary Batteries. *Chem. Soc. Rev.* **2013**, *42* (23), 9011–9034.
8. Xu, W.; Wang, J.; Ding, F.; Chen, X.; Nasybulin, E.; Zhang, Y.; Zhang, J. G. Lithium Metal Anodes for Rechargeable Batteries. *Energy Environ. Sci.* **2014**, *7* (2), 513–537.
9. Krauskopf, T.; Richter, F. H.; Zeier, W. G.; Janek, J. Physicochemical Concepts of the Lithium Metal Anode in Solid-State Batteries. *Chem. Rev.* **2020**, *120* (15), 7745–7794.
10. Fan, L.; Wei, S.; Li, S.; Li, Q.; Lu, Y. Recent Progress of the Solid-State Electrolytes

for High-Energy Metal-Based Batteries. *Adv. Energy Mater.* **2018**, *8* (11), 1702657.

11. Zhang, Z.; Shao, Y.; Lotsch, B.; Hu, Y. S.; Li, H.; Janek, J.; Nazar, L. F.; Nan, C. W.; Maier, J.; Armand, M.; Chen, L. New Horizons for Inorganic Solid State Ion Conductors. *Energy Environ. Sci.* **2018**, *11* (8), 1945–1976.
12. Swamy, T.; Park, R.; Sheldon, B. W.; Rettenwander, D.; Porz, L.; Berendts, S.; Uecker, R.; Carter, W. C.; Chiang, Y.-M. Lithium Metal Penetration Induced by Electrodeposition through Solid Electrolytes: Example in Single-Crystal $Li_6La_3ZrTaO_{12}$ Garnet. *J. Electrochem. Soc.* **2018**, *165* (16), A3648–A3655.
13. Ren, Y.; Shen, Y.; Lin, Y.; Nan, C. W. Direct Observation of Lithium Dendrites inside Garnet-Type Lithium-Ion Solid Electrolyte. *Electrochem. commun.* **2015**, *57*, 27–30.
14. Fan, X.; Ji, X.; Han, F.; Yue, J.; Chen, J.; Chen, L.; Deng, T.; Jiang, J.; Wang, C. Fluorinated Solid Electrolyte Interphase Enables Highly Reversible Solid-State Li Metal Battery. *Sci. Adv.* **2018**, *4* (12), eaau9245.
15. Nagao, M.; Hayashi, A.; Tatsumisago, M.; Kanetsuku, T.; Tsuda, T.; Kuwabata, S. In Situ SEM Study of a Lithium Deposition and Dissolution Mechanism in a Bulk-Type Solid-State Cell with a Li_2S-P_2S_5 Solid Electrolyte. *Phys. Chem. Chem. Phys.* **2013**, *15* (42), 18600–18606.
16. Xiao, Y.; Wang, Y.; Bo, S. H.; Kim, J. C.; Miara, L. J.; Ceder, G. Understanding Interface Stability in Solid-State Batteries. *Nat. Rev. Mater.* **2020**, *5* (2), 105–126.
17. Liu, H.; Cheng, X.-B.; Huang, J.-Q.; Yuan, H.; Lu, Y.; Yan, C.; Zhu, G.-L.; Xu, R.; Zhao, C.-Z.; Hou, L.-P.; He, C.; Kaskel, S.; Zhang, Q. Controlling Dendrite Growth in Solid-State Electrolytes. *ACS Energy Lett.* **2020**, *5* (3), 833–843.
18. Cao, D.; Sun, X.; Li, Q.; Natan, A.; Xiang, P.; Zhu, H. Lithium Dendrite in All-Solid-

State Batteries: Growth Mechanisms, Suppression Strategies, and Characterizations. *Matter* **2020**, *3* (1), 57–94.

19. Rehnlund, D.; Lindgren, F.; Böhme, S.; Nordh, T.; Zou, Y.; Pettersson, J.; Bexell, U.; Boman, M.; Edström, K.; Nyholm, L. Lithium Trapping in Alloy Forming Electrodes and Current Collectors for Lithium Based Batteries. *Energy Environ. Sci.* **2017**, *10* (6), 1350–1357.
20. Xu, H.; Li, Y.; Zhou, A.; Wu, N.; Xin, S.; Li, Z.; Goodenough, J. B. Li3N-Modified Garnet Electrolyte for All-Solid-State Lithium Metal Batteries Operated at 40 °C. *Nano Lett.* **2018**, *18* (11), 7414–7418.
21. Han, X.; Gong, Y.; Fu, K.; He, X.; Hitz, G. T.; Dai, J.; Pearse, A.; Liu, B.; Wang, H.; Rubloff, G.; Mo, Y.; Thangadurai, V.; Wachsman, E. D.; Hu, L. Negating Interfacial Impedance in Garnet-Based Solid-State Li Metal Batteries. *Nat. Mater.* **2017**, *16* (5), 572–579.
22. Tsai, C. L.; Roddatis, V.; Chandran, C. V.; Ma, Q.; Uhlenbruck, S.; Bram, M.; Heitjans, P.; Guillon, O. $Li_7La_3Zr_2O_{12}$ Interface Modification for Li Dendrite Prevention. *ACS Appl. Mater. Interfaces* **2016**, *8* (16), 10617–10626.
23. Han, F.; Yue, J.; Zhu, X.; Wang, C. Suppressing Li Dendrite Formation in Li_2S-P_2S_5 Solid Electrolyte by LiI Incorporation. *Adv. Energy Mater.* **2018**, *8* (18), 2–7.
24. Suyama, M.; Kato, A.; Sakuda, A.; Hayashi, A.; Tatsumisago, M. Lithium Dissolution/Deposition Behavior with Li_3PS_4-LiI Electrolyte for All-Solid-State Batteries Operating at High Temperatures. *Electrochim. Acta* **2018**, *286*, 158–162.
25. Otoyama, M.; Suyama, M.; Hotehama, C.; Kowada, H.; Takeda, Y.; Ito, K.; Sakuda, A.; Tatsumisago, M.; Hayashi, A. Visualization and Control of Chemically Induced Crack Formation in All-Solid-State Lithium-Metal Batteries with Sulfide Electrolyte.

ACS Appl. Mater. Interfaces **2021**, DOI: 10.1021/acsami.0c18314.

26. Ujiie, S.; Hayashi, A.; Tatsumisago, M. Preparation and Ionic Conductivity of (100-x)($0.8Li_2S{\cdot}0.2P_2S_5$)·xLiI Glass-Ceramic Electrolytes. *J. Solid State Electrochem.* **2013**, *17* (3), 675–680.
27. Kang, J.; Han, B. First-Principles Characterization of the Unknown Crystal Structure and Ionic Conductivity of $Li_7P_2S_8I$ as a Solid Electrolyte for High-Voltage Li Ion Batteries. *J. Phys. Chem. Lett.* **2016**, *7* (14), 2671–2675.
28. Choi, S.-J.; Choi, S.-H.; Dinh Bui, A.; Lee, Y.-J.; Lee, S.-M.; Shin, H.-C.; Ha, Y.-C. LiI-Doped Sulfide Solid Electrolyte: Enabling a High-Capacity Slurry-Cast Electrode by Low-Temperature Post-Sintering for Practical All-Solid-State Lithium Batteries. *ACS Appl. Mater. Interfaces* **2018**, *10* (37), 31404–31412.
29. J. Sedlmaier, S.; Indris, S.; Dietrich, C.; Yavuz, M.; Dräger, C.; von Seggern, F.; Sommer, H.; Janek, J. Li_4PS_4I: A Li^+ Superionic Conductor Synthesized by a Solvent-Based Soft Chemistry Approach. *Chem. Mater.* **2017**, *29* (4), 1830–1835.
30. Homma, K.; Yonemura, M.; Kobayashi, T.; Nagao, M.; Hirayama, M.; Kanno, R. Crystal Structure and Phase Transitions of the Lithium Ionic Conductor Li_3PS_4. *Solid State Ionics* **2011**, *182* (1), 53–58.
31. Dietrich, C.; Weber, D. A.; Sedlmaier, S. J.; Indris, S.; Culver, S. P.; Walter, D.; Janek, J.; Zeier, W. G. Lithium Ion Conductivity in Li_2S-P_2S5 Glasses-Building Units and Local Structure Evolution during the Crystallization of Superionic Conductors Li_3PS_4, $Li_7P_3S_{11}$ and $Li_4P_2S_7$. *J. Mater. Chem. A* **2017**, *5* (34), 18111–18119.
32. Hayashi, A.; Hama, S.; Minami, T.; Tatsumisago, M. Formation of Superionic Crystals from Mechanically Milled Li_2S-P_2S_5 Glasses. *Electrochem. commun.* **2003**,

5 (2), 111–114.

33. Kanno, R.; Murayama, M. Lithium Ionic Conductor Thio-LISICON: The Li_2S-GeS_2-P_2S_5 System. *J. Electrochem. Soc.* **2001**, *148* (7), A742.
34. Tsukasaki, H.; Mori, S.; Morimoto, H.; Hayashi, A.; Tatsumisago, M. Direct Observation of a Non-Crystalline State of Li_2S-P_2S_5 Solid Electrolytes. *Sci. Rep.* **2017**, *7* (1), 1–7.
35. Shiotani, S.; Ohara, K.; Tsukasaki, H.; Mori, S.; Kanno, R. Pair Distribution Function Analysis of Sulfide Glassy Electrolytes for All-Solid-State Batteries: Understanding the Improvement of Ionic Conductivity under Annealing Condition. *Sci. Rep.* **2017**, *7* (1), 6972.
36. Gautam, A.; Sadowski, M.; Prinz, N.; Eickhoff, H.; Minafra, N.; Ghidiu, M.; P. Culver, S.; Albe, K.; F. Fässler, T.; Zobel, M.; G. Zeier, W. Rapid Crystallization and Kinetic Freezing of Site-Disorder in the Lithium Superionic Argyrodite Li_6PS_5Br. *Chem. Mater.* **2019**, *31* (24), 10178–10185.
37. Kraft, M. A.; Culver, S. P.; Calderon, M.; Bo, F.; Krauskopf, T.; Senyshyn, A.; Dietrich, C.; Zevalkink, A.; Janek, J.; Zeier, W. G. Influence of Lattice Polarizability on the Ionic Conductivity in the Lithium Superionic Argyrodites Li_6PS_5X (X = Cl , Br , I). *J. Am. Chem. Soc.* **2017**, *139* (31), 1–15.
38. Cheng, L.; Chen, W.; Kunz, M.; Persson, K.; Tamura, N.; Chen, G.; Doeff, M. Effect of Surface Microstructure on Electrochemical Performance of Garnet Solid Electrolytes. *ACS Appl. Mater. Interfaces* **2015**, *7* (3), 2073–2081.
39. Tsai, C.-L.; Roddatis, V.; Vinod Chandran, C.; Ma, Q.; Uhlenbruck, S.; Bram, M.; Heitjans, P.; Guillon, O. $Li_7La_3Zr_2O_{12}$ Interface Modification for Li Dendrite Prevention. *ACS Appl. Mater. Interfaces* **2016**, *8* (16), 10617–10626.

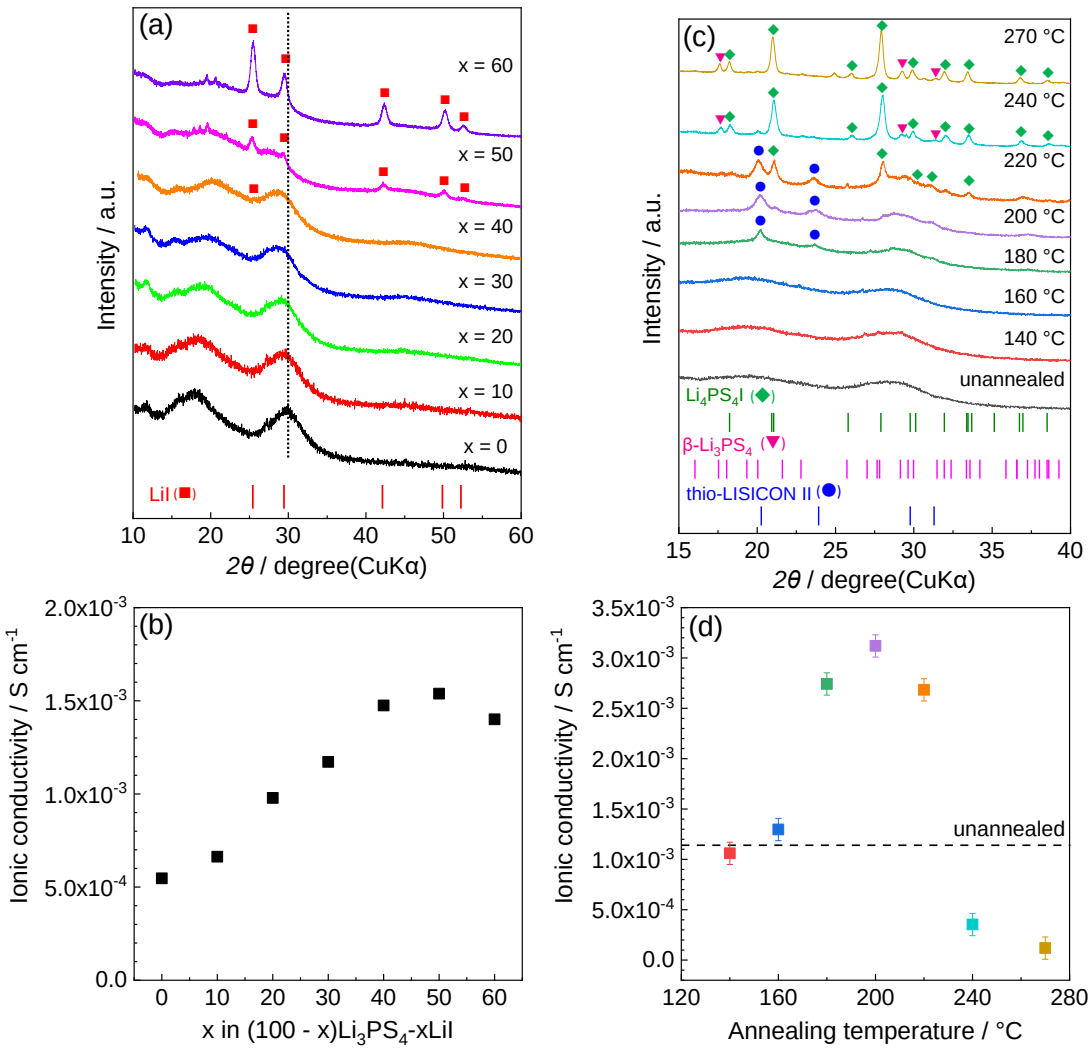

Figure 1. (a) XRD patterns and (b) lithium ionic conductivities at 25 °C of (100−x)Li_3PS_4-xLiI prepared using the mechanical milling method with different amounts of LiI. (c) XRD patterns and (d) lithium ionic conductivities at 25 °C of 70Li_3PS_4-30LiI prepared using the mechanical milling method and annealed at various temperatures for 2 h.

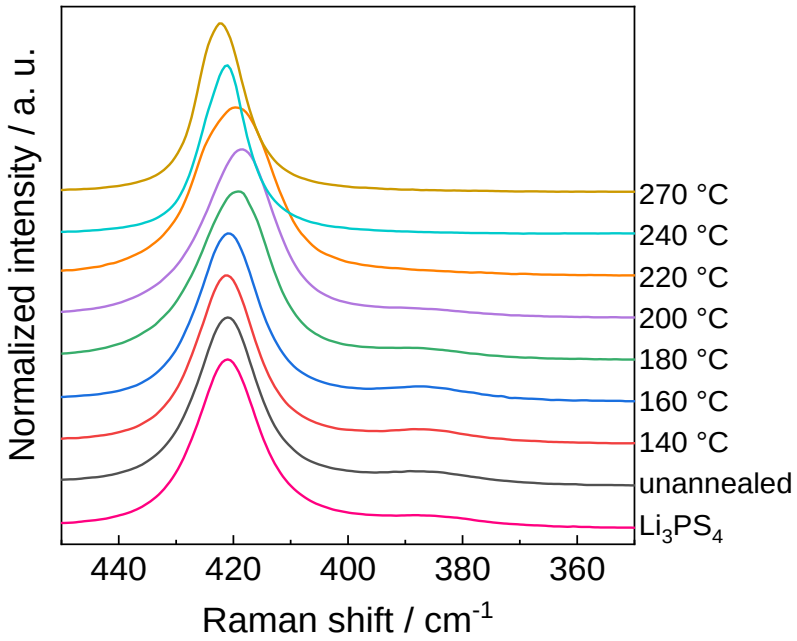

Figure 2. Raman spectra of Li_3PS_4 and $70Li_3PS_4$-30LiI prepared using the mechanical milling method before annealing and after annealing at various temperatures.

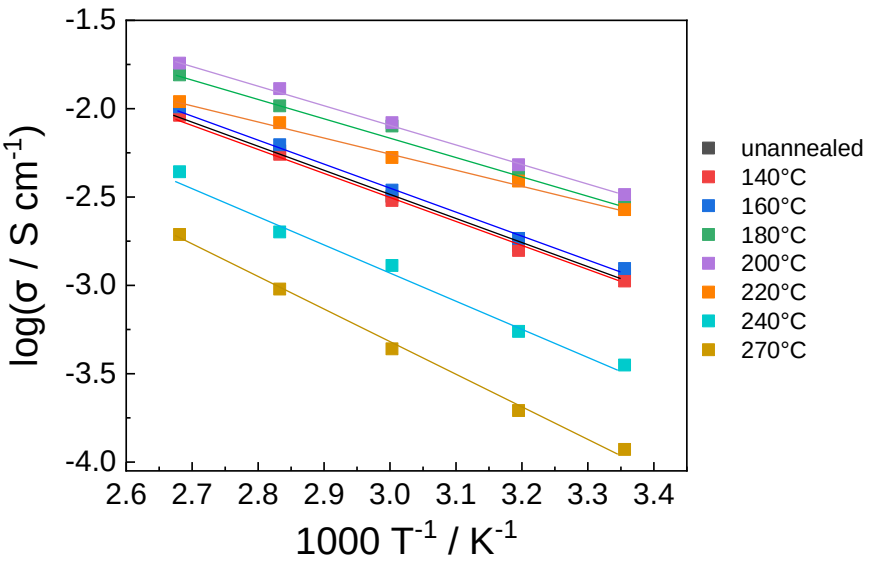

Figure 3. Arrhenius plots of $70Li_3PS_4$-30LiI prepared using the mechanical milling method and annealed at various temperatures for 2 h.

Table 1. Activation energies and frequency factors obtained from the Arrhenius plots of $70Li_3PS_4$-30LiI prepared using the mechanical milling method and annealed at various temperatures for 2 h.

	Activation energy / eV	Frequency factor
unannealed	0.274	46.3
annealed at 140 ºC	0.281	52.3
annealed at 160 ºC	0.272	47.7
annealed at 180 ºC	0.199	13.6
annealed at 200 ºC	0.181	3.67
annealed at 220 ºC	0.196	5.63
annealed at 240 ºC	0.317	76.1
annealed at 270 ºC	0.362	139.5

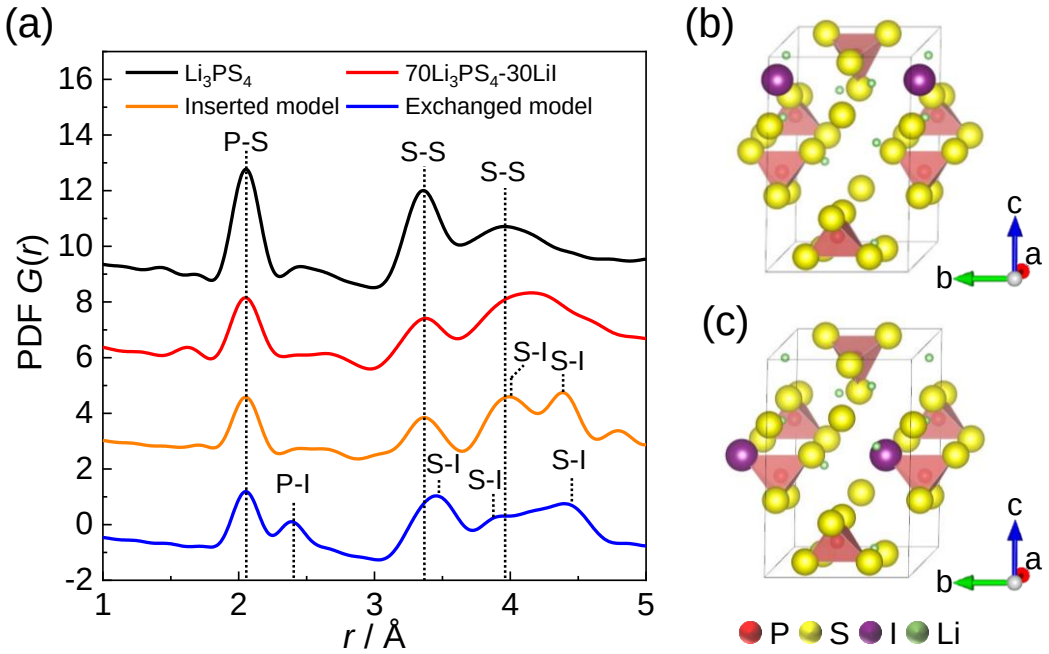

Figure 4. (a) Reduced PDF, $G(r)$, of Li_3PS_4 (pink line) and $70Li_3PS_4$-30LiI prepared using the mechanical milling method. The red line is the simulated PDF obtained using the inserted model shown in (b); the blue line is the simulated PDF obtained using the exchanged model shown in (c).

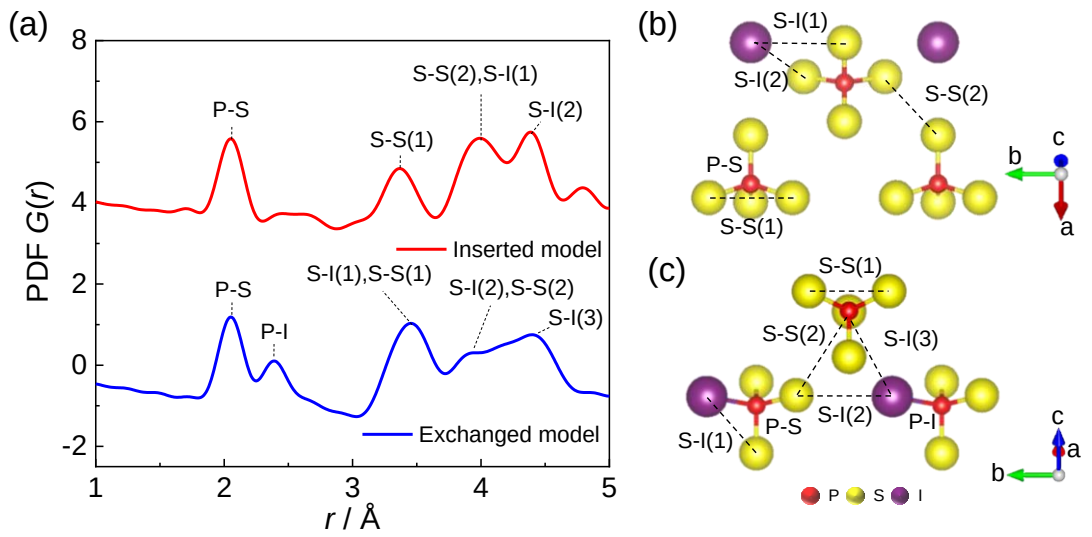

Figure 5. (a) Reduced PDF, *G*(*r*), simulated using inserted and exchanged models. (b) Crystal structure of the exchanged model. (c) Atomic arrangement around iodine in the exchanged model.

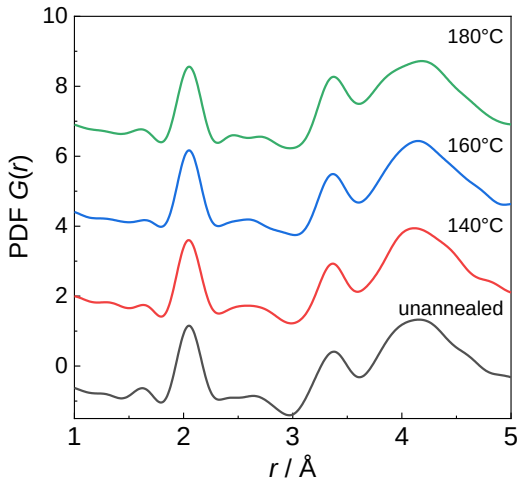

Figure 5. Reduced PDF, $G(r)$, of $70Li_3PS_4$-30LiI prepared using the mechanical milling method before annealing and after annealing at various temperatures for 2 h.

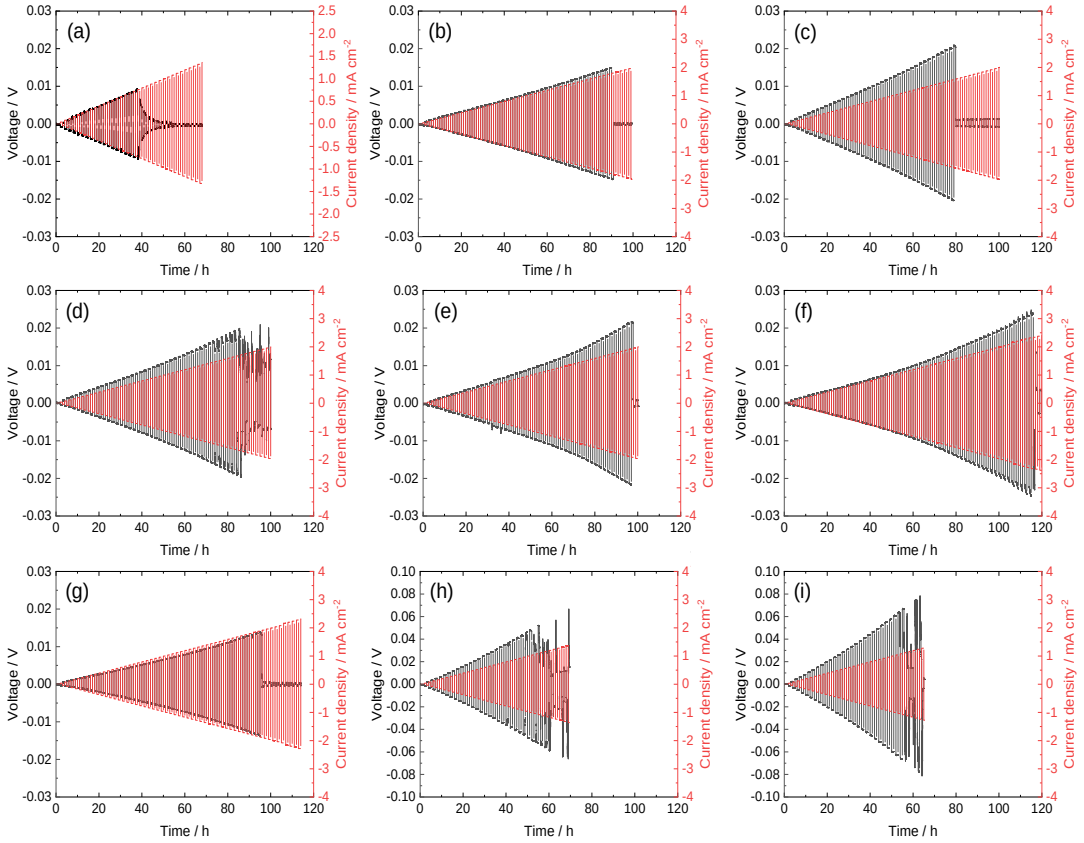

Figure 6. Galvanostatic cycling test results for (a) Li_3PS_4 and $70Li_3PS_4$-30LiI prepared using the mechanical milling method (b) unannealed and after annealing at (c) 140, (d) 160, (e) 180, (f) 200, (g) 220, (h) 240, and (i) 270 °C using the lithium metal/solid electrolyte/lithium metal cells with current density increasing by 0.04 mA cm^{-2} after charging and discharging for 1 h at 100 °C.

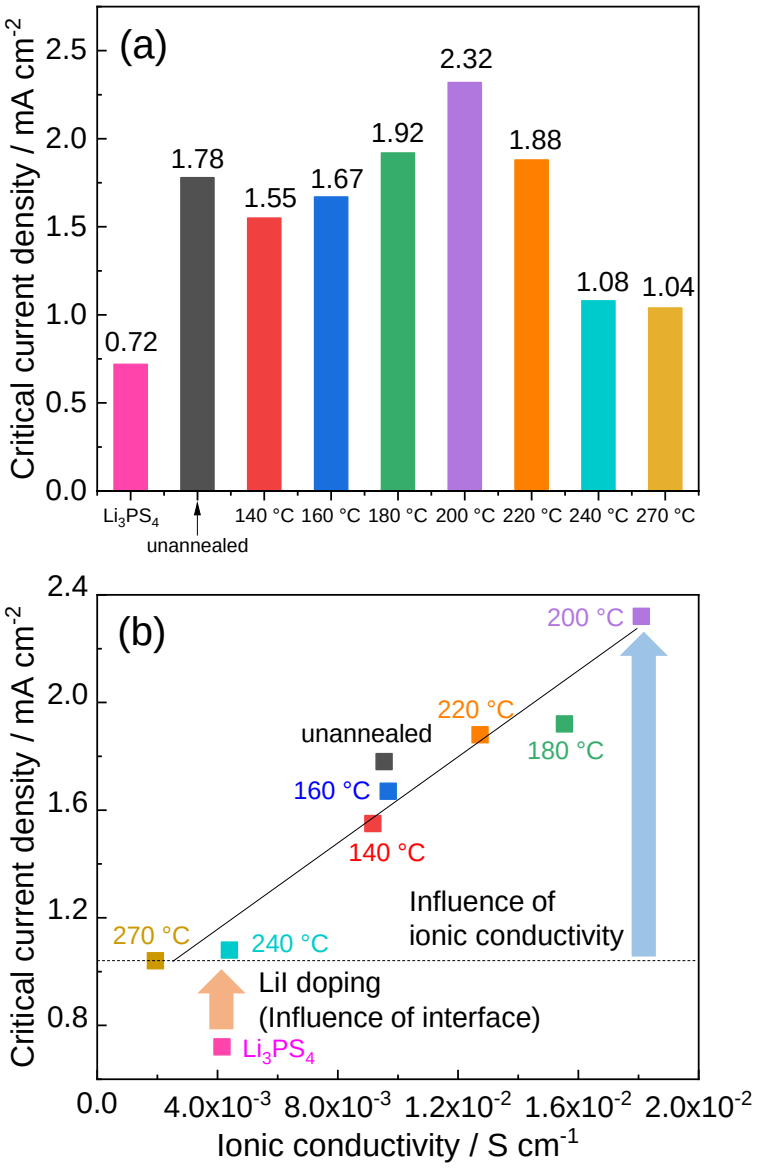

Figure 7. (a) Critical current densities at 100 °C of Li_3PS_4 and $70Li_3PS_4$-30LiI prepared using the mechanical milling method unannealed and after annealing at various temperatures for 2 h. (b) Correlations between the lithium ionic conductivity and critical current density at 100 °C of Li_3PS_4 and $70Li_3PS_4$-30LiI prepared using the mechanical milling method unannealed and after annealing at various temperatures for 2 h.

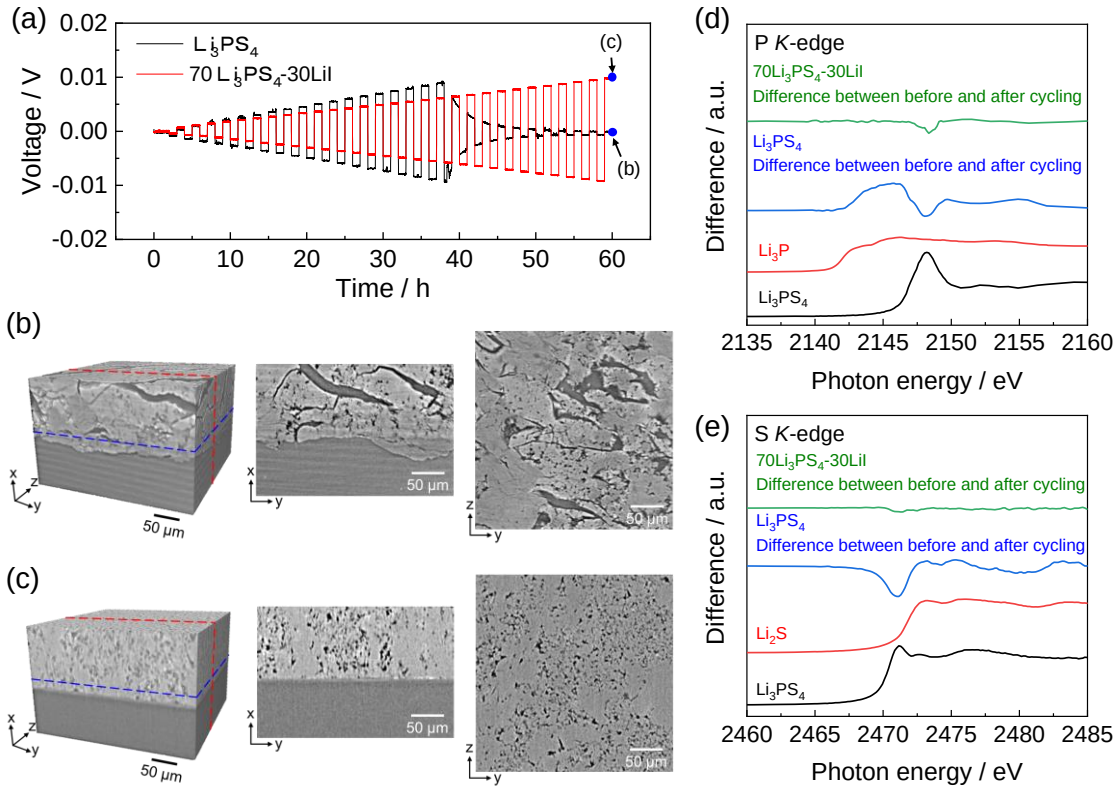

Figure 8. (a) Galvanostatic cycling test results for Li_3PS_4 and $70Li_3PS_4$-30LiI using Li/solid electrolyte/Li cells under the same conditions. The black line represents Li_3PS_4; the red line represents unannealed $70Li_3PS_4$-30LiI. Transmission images of (b) Li_3PS_4 and (c) $70Li_3PS_4$-30LiI after the galvanostatic cycling tests. (d) P *K*-edge and (e) S *K*-edge XANES difference spectra of Li_3PS_4 and $70Li_3PS_4$-30LiI after the galvanostatic cycling tests.

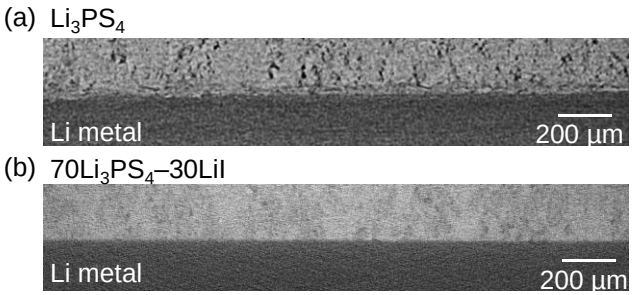

Figure 9. Cross-sectional images of 3D volume data of (a) Li_3PS_4 and (b) $70Li_3PS_4$-30LiI from lab-CT measurements after galvanostatic tests.

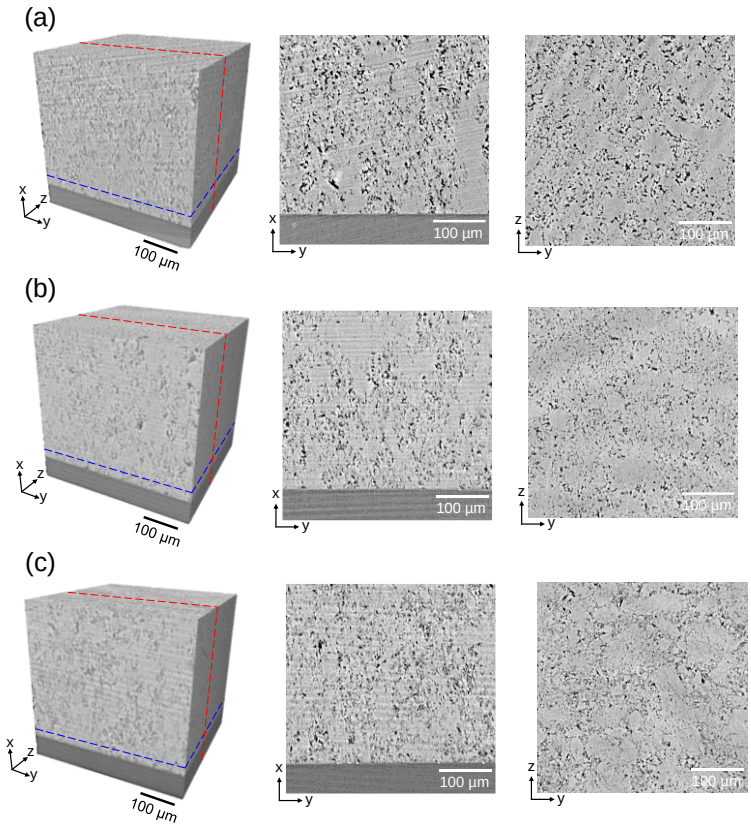

Figure 10. Transmission images of (a) Li_3PS_4, (b) unannealed $70Li_3PS_4$-30LiI, and (c) $70Li_3PS_4$-30LiI annealed at 200 °C before the galvanostatic cycling tests.

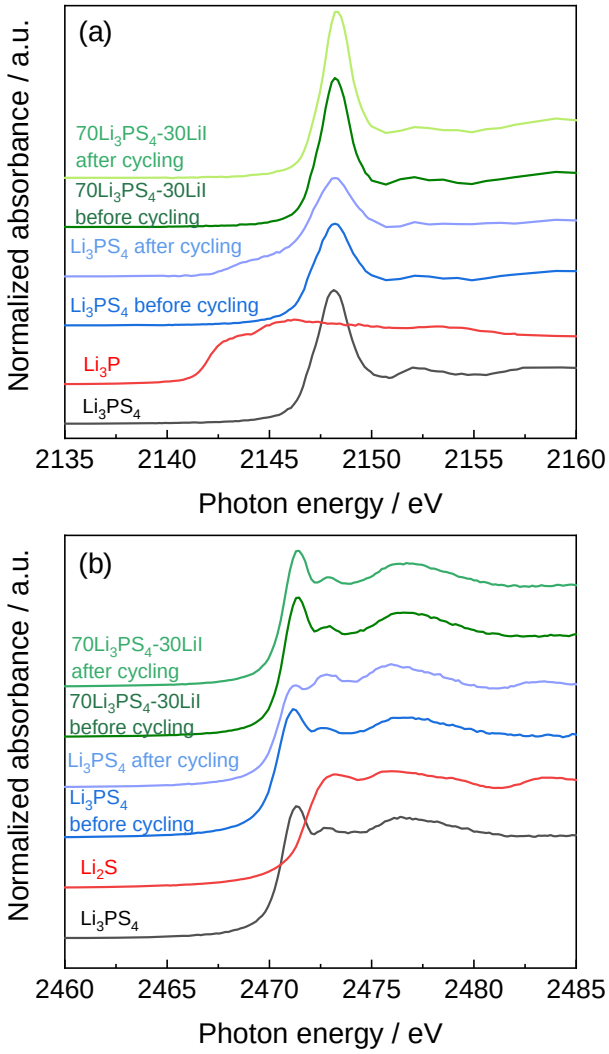

Figure 11. (a) P *K*-edge and (b) S *K*-edge XANES spectra of Li_3PS_4 and $70Li_3PS_4$-30LiI before and after the galvanostatic cycling tests using the lithium metal/solid electrolyte/lithium metal cells.

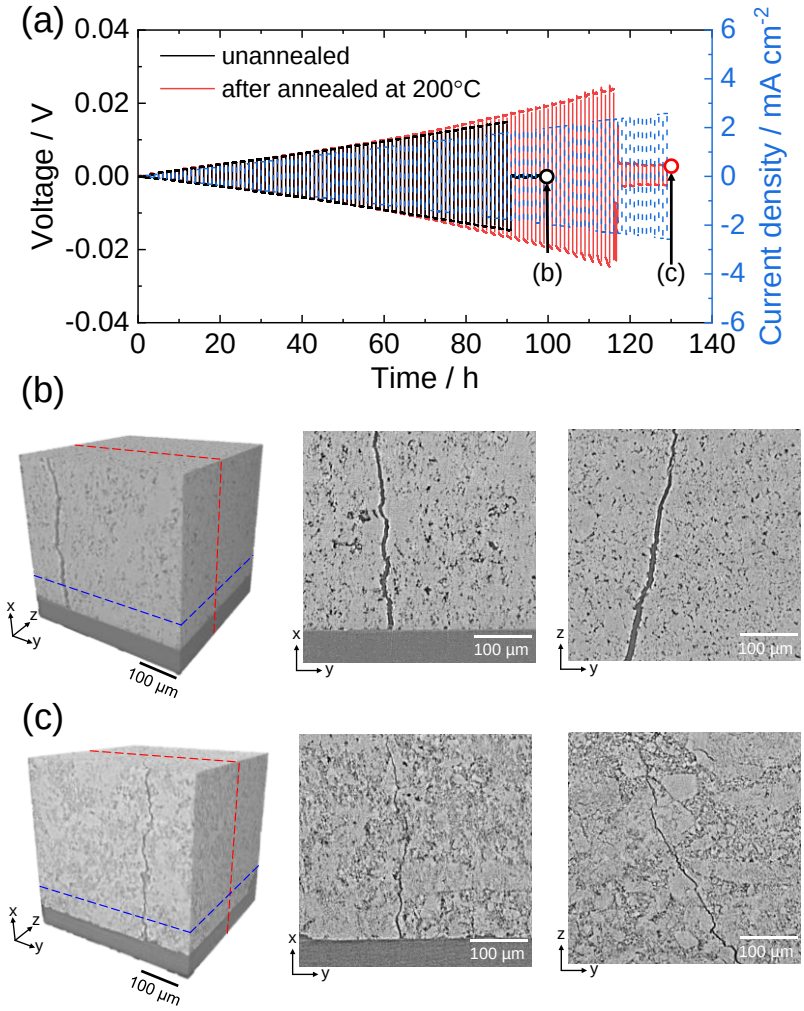

Figure 12. (a) Results of the galvanostatic cycling tests for $70Li_3PS_4$-30LiI and $70Li_3PS_4$-30LiI annealed at 200 °C using the lithium metal/solid electrolyte/lithium metal cells with current density increasing by 0.04 mA cm^{-2} after charging and discharging for 1 h at 100 °C. Transmission images of (b) $70Li_3PS_4$-30LiI and (c) $70Li_3PS_4$-30LiI annealed at 200 °C after the galvanostatic cycling tests.

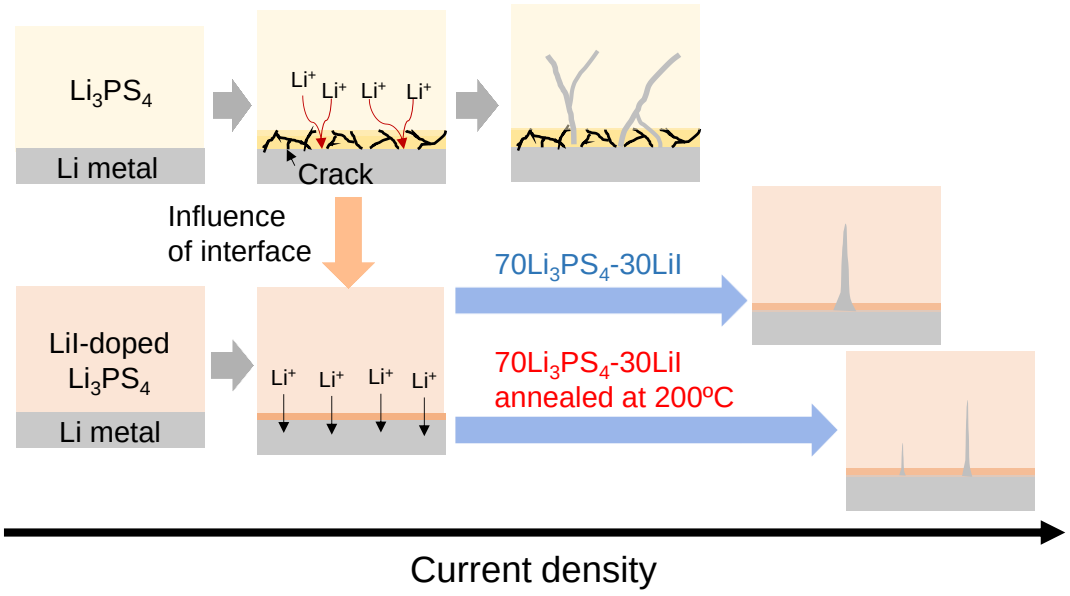

Figure 12. Schematic diagram of dendrite growth in Li_3PS_4 and Li_3PS_4-LiI.

Chapter 6. General conclusions

Fuel cells and LIBs are suitable for powering vehicles and as distributed energy-storage devices. However, the performance of these electrochemical devices is not sufficient. Therefore, it is necessary to improve their performance for use in smart grids. Disordered materials, such as nanoparticles and amorphous materials, are important for improving the performance of electrochemical devices, and the exploration of these materials is underway. To further improve their properties, it is necessary to understand the influence of disordered structures in disordered materials. In the present work, the structure of the disordered materials was evaluated by using pair distribution function analysis to elucidate the dominant factors in electrochemical materials.

In Chapter 1, the overview of electrochemical devices was described. The importance of understand the influence of disordered structures to the properties was described. Method to analyze the disordered materials were reviewed.

In Chapter 2, a surface structure analysis method using a pair distribution function analysis was developed. The correlation between the Pt-Pt interatomic distance and the area specific activity of Pt/C catalysts with different particle sizes was investigated. As a result, the developed method was possible to evaluate the changes in the surface structure that could not be evaluated by XAFS measurements. The method in this study could lead to a further understanding of the factors controlling the specific activity of the oxygen reduction reaction and the degradation mechanism of a Pt/C catalyst.

In Chapter 3, the dominant factors controlling the lithium ionic conductivity of Li_3PS_4 synthesized by the liquid phase synthesis method were elucidated by using pair distribution function analysis. It was found that the factors influence to the lithium ionic conductivity of Li_3PS_4 were the crystallinity and the residual amount of the intermediate. The residual amount of the intermediate in the sample decreased with the increase of the annealing time, while the crystallinity of Li_3PS_4 increased. This trade-off relationship between the crystallinity and the residual amount of the solvent in the sample determines the lithium ionic conductivity.

In Chapter 4, the effect of the boiling point of the solvent to the ionic conductivity of Li_3PS_4 synthesized in liquid phase was elucidated by using pair distribution function analysis. The use of low boiling point solvents enables the removal of intermediates from the sample while suppressing the crystallization of Li_3PS_4. Therefore, it was found that the ionic conductivity was improved by using low boiling point solvents.

In Chapter 5, the elucidation of structure of LiI-doped Li_3PS_4 by pair distribution function analysis and the suppression mechanism of lithium dendrite formation by adding LiI into Li_3PS_4. As a result of pair distribution function analysis, it was found that iodine occupied between PS_4^{3-} tetrahedra anion, and the bulk structure of the LiI-doped Li_3PS_4, which affects the electrochemical stability, was clarified. In addition, it was found that the addition of lithium iodide improved the interfacial stability and the ionic conductivity of the solid electrolyte, and suppressed the formation of lithium dendrites.

In Chapter 6, the results of the thesis were summarized.

Acknowledgements

The study on this thesis has been carried out at Graduate School of Human and Environmental Studies, Kyoto University.

First of all, I would like to wish to express my special gratitude to Prof. Yoshiharu Uchimoto for his precise indications and valuable advices. He has walked me through all the stages of the writing of this thesis. Without his consistent and illuminating instruction, this thesis could not have reached its present form.

Special thanks are expressed to Dr. Koji Ohara for their advices on the whole study and his guidance.

I am also grateful to Dr. Kentaro Yamamoto, Dr. Tomoki Uchiyama, Dr. Toshiki Watanabe and Prof. Toshiyuki Matsunag, for his useful comments and discussions.

I would like to thank to all the members of Prof. Uchimoto's laboratory for their helps, discussions and encouragement throughout this study.

Finally, I would like to appreciate my parents for their understanding and support.

Masakuni Takahashi

Copyright

Huy Phuc, Toshiki Watanabe, Tomoki Uchiyama, Atsushi Sakuda, Akitoshi Hayashi, Masahiro Tatsumisago, Hiroyuki Muto, Atsunori Matsuda, Yoshiharu Uchimoto

("Solid State Ionics" March 2021, Volume 361, 115568)

doi : 10.1016/j.ssi.2021.115568

The final pbulication is avaliable at Elsevier pubtications via https://doi.org/10.1016/j.ssi.2021.115568